Microwave Filters Based on New Design Concepts in Several Technologies with Emphasis on the Printed Ridge Gap Waveguide Technology

Milad Sharifi Sorkherizi

A Thesis
in the Department
of
Electrical and Computer Engineering

Presented in Partial Fulfillment of the Requirements
for the Degree of
Doctor of Philosophy (Electrical and Computer Engineering) at
Concordia University
Montreal, Quebec, Canada

August 2016

CONCORDIA UNIVERSITY

SCHOOL OF GRADUATE STUDIES

This is to certify that the thesis prepared

By: Milad Sharifi Sorkherizi

Entitled: Microwave Filters Based on New Design Concepts in Several Technologies with Emphasis on the Printed Ridge Gap Waveguide Technology

and submitted in partial fulfillment of the requirements for the degree of

Doctor of Philosophy (Electrical & Computer Engineering)

Complies with the regulations of the University and meets the accepted standards with respect to originality and quality.

Signed by the final examining committee:

Dr. G. Gouw	Chair
Dr. R. Mansour	External Examiner
Dr. A. Youssef	External to Program
Dr. R. Paknys	Examiner
Dr. A. Sebak	Examiner
Dr. A. Kishk	Thesis Supervisor

Approved by: Dr. W. –P. Zhu, Graduate Program Director

August 1, 2016   Dr. A. Asif, Dean, Faculty of Engineering & Computer Science

Abstract

Microwave Filters Based on New Design Concepts in Several Technologies with Emphasis on the Printed Ridge Gap Waveguide Technology

Milad Sharifi Sorkherizi, Ph.D.

Concordia University, 2016

Microwave filters have been an interesting research topic for more than half a century. Since any communication system is required to use some microwave filters, considerable effort is being made to optimize the performance and size of these filters. As operating frequency is on the rise, filter design becomes more challenging with the demand for low insertion losses and low cost. As low cost might require the use of printed circuit technology, high performance demands waveguide technology that drives the cost to unacceptable levels. There is a need for a new technology that achieves both requirements of low cost and high performance.

The new technology of ridge gap waveguide that was proposed in 2011 shows promising characteristics as a new guiding structure, especially for high-frequency bands. Therefore, it is necessary to design and propose classic or even new filtering devices on this technology. Here, we propose the use of this technology to design practical and efficient microwave filters.

The work of this thesis can be divided into three major parts: (1) Developing efficient codes and methods to optimize the computationally expensive structure of ridge gap waveguide or any other large-scale microwave filter device. (2) Characterizing cavity structures on ridge gap waveguide and using them in the design of simple microwave filters. (3) The third part will discuss more advanced and practical filters, especially using printed ridge gap waveguide technology. The ultimate goal of this thesis is to design and propose state of the art designs in the field of microwave filters that can satisfy the requirements of today's advanced communication systems and to be cost efficient and compete with other rival technologies. We achieved these objectives using efficient optimization, efficient design techniques, and fabrication of the models using advanced technology.

Keywords: Microwave filters; diplexers; gap waveguide; electromagnetic band gap; optimization.

Dedication

TO THE MEMORY OF MY FATHER

Acknowledgements

I sincerely wish to thank my supervisor, Prof. Ahmed Kishk for all his guidance and support. It was a real pleasure for me to have such an exceptional scholar and it was my honor to be his PhD student.

Furthermore, I would like to thank the committee members, Prof. Mansour, Prof. Paknys, Prof. Sebak and Prof. Youssef for their review of my thesis and their numerous constructive comments and feedback.

Table of Contents

List of Tables

List of Figures

x

List of Acronyms

RGW   Ridge Gap Waveguide

PRGW   Printed Ridge Gap Waveguide

MS   Microstrip

SIW   Substrate Integrated Waveguide

LTCC   Low-Temperature Co-fired Ceramic

EBG   Electromagnetic Band Gap

CM   Coupling Matrix

TEM   Transverse Electromagnetic Wave

PMC   Perfect Magnetic Conductor

AMC   Artificial Magnetic Conductor

CST MWS   Computer Simulation Technology Microwave Studio

HFSS   High Frequency Structure Simulator

EM   Electromagnetic

Tx   Transmitter

Rx   Receiver

BW   Bandwidth

FBW   Fractional Bandwidth

TZ   Transmission Zero

ME   Magneto-Electric

2D   2 Dimensional

3D   3 Dimensional

Chapter 1.

Introduction

1.1. Challenges in Microwave Devices Fabrication

With the growing demand for utilizing high data transfer rates, high-frequency bands are finding more and more applications. Particularly in the millimeter-wave frequency band that is recognized to extend from 30 to 300 GHz with a corresponding wavelength of 1-10 mm, high data transfer rate is easily achievable. Hence, considerable efforts are being made to design microwave components for those frequency bands, which should be cost effective without jeopardizing the functionality. The most common technologies for microwave devices are hollow waveguides (rectangular and cylindrical waveguide), strip and microstrip lines and SIW waveguide, which all of them have inevitable problems in high-frequency bands. For hollow waveguides, as they need to be fabricated in separate parts and then connected, intact electrical contact between separate parts should be insured, which is difficult and expensive in high-frequency bands. Therefore, even though hollow waveguide devices have excellent performance in millimeter and submillimeter bands, they are not cost effective. Also, weight and size of circuits in waveguide technology make them an undesirable solution. For the strip and microstrip line and SIW waveguide, as the wave is propagating inside the dielectric, high-frequency applications suffer from the high dielectric loss. In addition to the dielectric loss, considerable radiation loss exists in microstrip line.

Many designs have been proposed as a guiding structure to overcome the problems above. As a pioneer, NRD (Non-radiative Dielectric) waveguide was invented in the 1980s [1], which is a dielectric rod sandwiched between two parallel plates. In this way, there will be a TEM transmission line, which does not need any electrical contact, and leakage is limited by using the dielectric rod and maintaining the gap between the

plates smaller than a quarter of a wavelength. However, this technology still suffers from dielectric loss.

As it can be seen, there is still no appropriate and acceptable guiding technology for millimeter and terahertz frequency bands. Even though rectangular and cylindrical waveguides have the best performance regarding the loss, inability to realize perfect electrical contact between the separate parts of a device by conventional methods makes them an unattractive solution for high-frequency bands. Special techniques have been proposed to realize acceptable electrical contact such as diffusion bonding [2] which again adds to the cost. Other technologies like SIW and microstrip line are all based on propagation inside the dielectric, which is not efficient in the millimeter band. Moreover, microstrip circuits require adequate packaging to minimize the radiation loss. Therefore, the need for a new guiding technology that can fill the gap between the performance of hollow waveguides and cost effectiveness of printed boards is present in today's industrial environment.

1.2. Gap Waveguide Technology

Recently, a new metamaterial-based guiding structure in the gap between two parallel metallic plates has been introduced [3], [4]. The ridge gap waveguide supports quasi-TEM wave propagation in the air gap between the metallic plates. The lower plate is textured with a 2D periodic structure, as well as intermediate ridges. The 2-D periodic structure introduces artificial magnetic conductor (AMC) boundary conditions that together with the smooth upper plate produce a stopband for parallel-plate modes and confine the energy along the guiding ridge. The proposed wave-guiding structure can be realized without any dielectric material, and no electrical connection between the plates is required. These features highlight this technology as a suitable candidate for millimeter and submillimeter band guiding structure for realizing microwave components. Figure 1-1 shows the general overview of this technology.

The design of a ridge gap waveguide consists of two major parts. Initially, the periodic electromagnetic band gap (EBG) structure should be designed to cover a specific frequency band. Several studies were done to compare the performance of different unit

cell configurations that exist in the literature [5]. Generally, a bed of nails structure is a suitable candidate that provides significant bandwidth and ease of fabrication. Figure 1-2 shows a bed of nail unit cell and its band gap, calculated using CST Eigenmode solver [6]. As it can be seen, the unit cell can cover 7.16 to 17.13 GHz. The effect of different dimensions of the unit cell on the band gap was thoroughly investigated in [5].
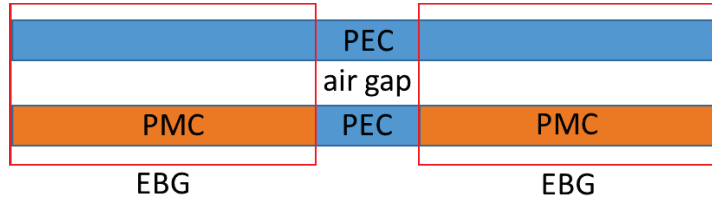
Figure 1-1.   Overview of the ridge gap waveguide.
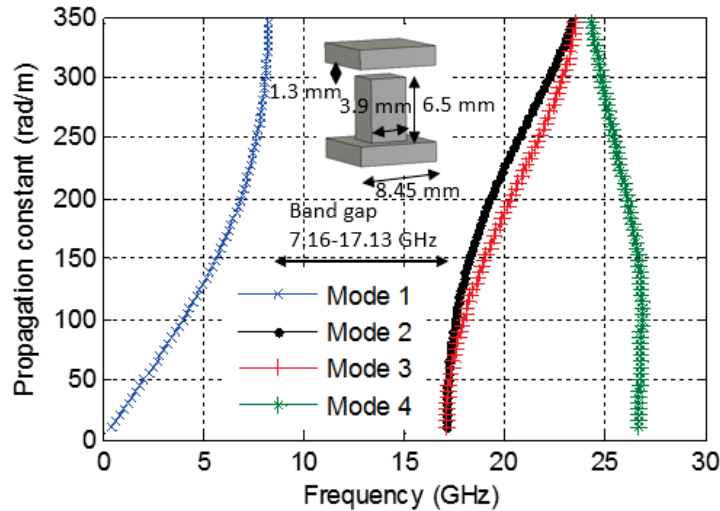
Figure 1-2.   Dispersion diagram of a periodic bed of nails structure as an EBG unit cell.

After the design of the periodic EBG structure, the dimensions of the ridge are calculated to have a 50 Ω transmission line. Different approaches can be taken to calculate the characteristic impedance of the transmission line. A closed form equation was introduced in [7] for this case which has a good agreement with the results from CST. It should be stated that the ridge gap waveguide's characteristic impedance varies versus frequency over the band gap provided by the EBG structure. Therefore, it should be categorized as a quasi-TEM medium, and not TEM.
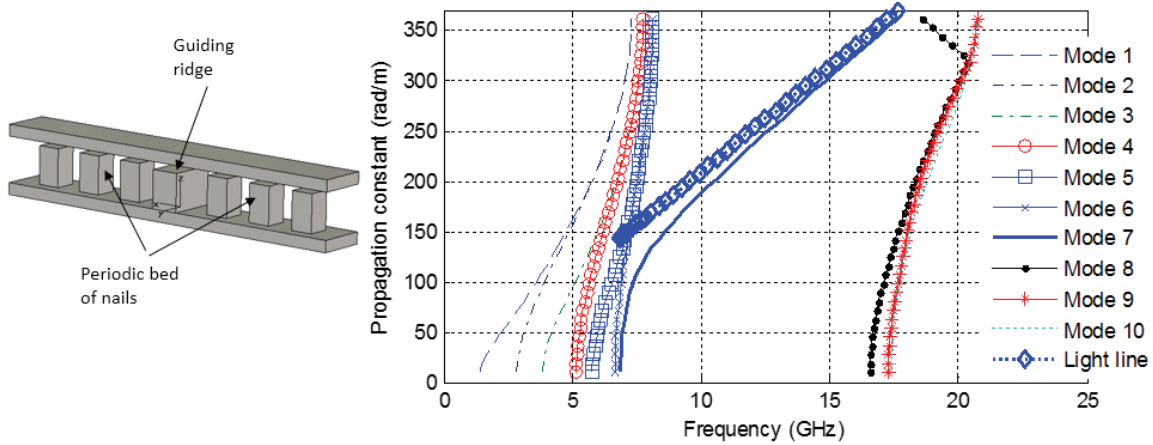
Figure 1-3. **Dispersion diagram of ridge gap waveguide that consists of a semi-periodic bed of nails and a guiding ridge. The propagation and periodicity are in the y-direction.**

The dispersion diagram of the complete ridge gap waveguide, which consists of the semi-periodic unit cells and the ridge, can be calculated using CST Eigenmode solver in a similar way. Figure 1-3 shows the dispersion diagram of the specific prototype that is covering the x-band. It is noticeable that the working bandwidth is decreased compared to what the unit cell can provide.

1.3. Printed Ridge Gap Waveguide

Another configuration of gap waveguide was proposed in [8] that can be fabricated by printed circuit board (PCB) technology. In this case, the unit cells are created by plated vias topped by microstrip patches (mushroom) that can provide the desired band gap. The capabilities of this new technique are promising since the structure is light and low cost and the performance regarding the loss is incomparably better than conventional microstrip waveguide. The dispersion diagram of a periodic unit cell along with the dimensions are shown in Figure 1-4. The unit cell is designed to cover 20-40 GHz to be used in millimeter band. The dispersion diagram of the complete printed ridge gap waveguide is presented in Figure 1-5. It is apparent that printed ridge gap waveguide cannot provide the bandwidth as large as the conventional ridge gap waveguide. However, as the manufacturing cost of PCB fabrication is significantly lower compared CNC

4

machining, printed ridge gap waveguide is an interesting solution for high-frequency microwave devices.
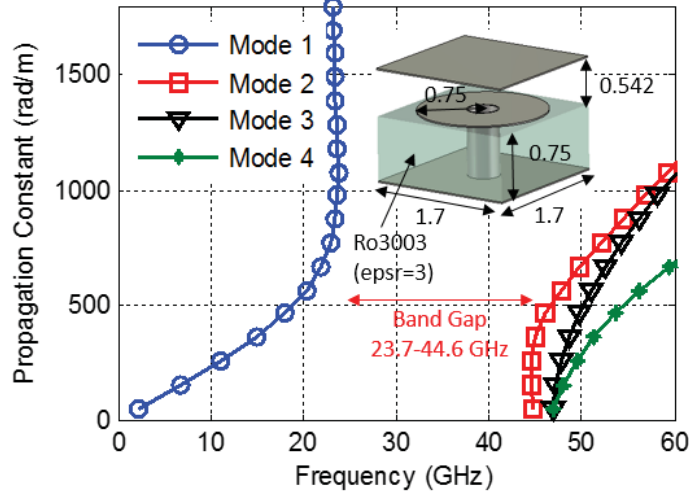
Figure 1-4.   Dispersion diagram of plated via topped by a circular patch.
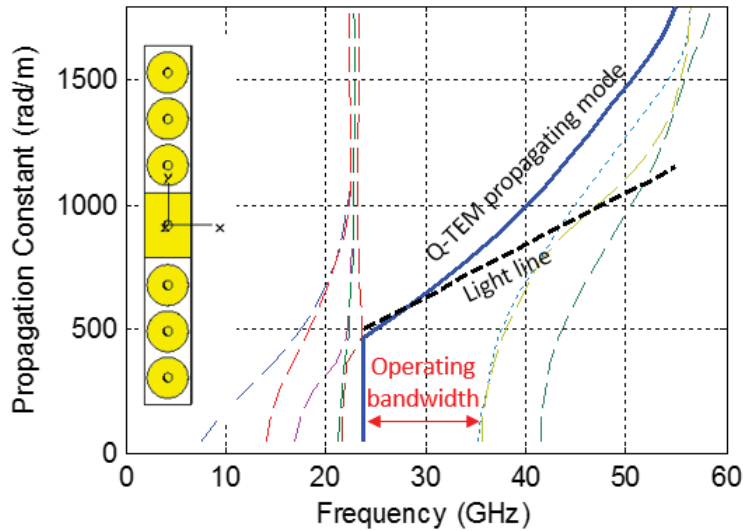
Figure 1-5.   Dispersion diagram of a PRGW consists of semi-periodic plated vias and short-circuited ridge.

The explained geometries of gap waveguide technology both for the regular and printed format, reveal that it has the potential to be a standard guiding medium for the applications that low-loss performance is required and at the same time, low-cost fabrication of the structure is a necessity. Since gap waveguide does not rely on any dielectric medium, the dielectric loss of them is avoided to a great extent. Also, electrical

5

contact is not required between different parts of the structure. As the result, devices in this technology have a simple mechanical assembly.

1.4. Motivation

One fundamental component of any communication system is the filter, which governs the characteristics of a communication transponder. With the introduction of new communication standards and the need to use the spectrum more efficiently, the number of the filtering devices in any communication system is increasing. Also, more constraints are being added to the performance of the filters. There has been huge research and development in filter design and optimization during past few decades, mainly after the introduction of the coupling matrix method in the 1970s [9], [10].

The ridge gap waveguide seems to be a good candidate to dominate the millimeter wave region and even terahertz frequency band. Hence, standard and practical filtering functions should be implemented in this new technology. There has been already a few publications on this issue [11]–[13], but in all of them, the classic theoretical approach in design and optimization of the filters is missing.

Due to the nature of the ridge gap technology, it is bigger in size compared to other guiding structures and much more complicated in details. Therefore, it is computationally expensive to be solved by a commercial EM solver. In order to be able to tune and optimize the filtering functions implemented in this new technology, some tools are required to be developed. The space mapping technique [14] along with coupling matrix theory will be used for the design, tuning and optimization of the filters in RGW. Several tools for the extraction of the coupling parameters from the simulated S-parameters are needed to be used in space mapping, which is developed during the work of this thesis.

1.5. Objectives

The concentration of the thesis is divided into three major parts:

Practical microwave bandpass and bandstop filters on ridge gap waveguide technology are developed in this thesis. The most popular microwave filter is the direct coupled cavity bandpass filter, which was already developed in a few publications. This class of filters is studied in detail, and one model has been fabricated and measured. The necessity for this task is characterization and studying the available and possible cavity structures suitable for this technology. The complexity and requirement of using the bandwidth as efficiently as possible in today's communication systems, compels the filter designers to use filters with transmission zeros at finite frequencies. To our knowledge, there has been no publication on filters with finite transmission zeros on RGW waveguide. This issue is addressed by this research, and a few models have been developed. Another advantage of the RGW is the ability of fabrication using PCB technology. It will be referred to as printed ridge gap waveguide (PRGW) technology. It is anticipated that PRGW has better performance compared to other technologies implemented on printed circuit boards. This topic is studied by design, optimization, and fabrication of several practical filters using PRGW in the millimeter frequency band. The results are compared with existing technologies for developing microwave filters using PCB such as microstrip filters.

Another concentration of this thesis is the development of a guiding structure in gap waveguide technology with improved characteristics. In Chapter 4, a modified version of PRGW is proposed with facilitated design properties and improved operating bandwidth. Few models have been developed, fabricated and measured on the proposed geometry consisting of waveguide lines and bends, bandpass and bandstop filters and feed network of antenna arrays.

A major part of this thesis is devoted to general filter theory, design, and optimization. In Chapter 5, a new methodology is proposed to design wideband and large scale bandpass filters and diplexers. The proposed method is the combination of group delay method [15] and space mapping [14], improved with additional techniques to provide a robust and efficient method to design filtering structures that normally requires many steps of full-wave optimization. The method is validated through the design of few prototypes in waveguide technology. Later, in Chapter 6, the developed method is used in optimization of an extremely large-scale integrated diplexer-power divider on gap waveguide technology.

1.6. Thesis Outline

This thesis is organized into seven chapters with abstract and references as follows:

Chapter 2 presents the design of perfectly tuned bandpass filters on a defected bed of nails cavity and ridge gap waveguide. The space mapping method and coupling matrix are used to tune and optimize the proposed structures that can overcome the computationally expensive nature of the gap wave technology. New input/output and inter-cavity coupling mechanisms are proposed and used in the designs. A new coaxial transition to ridge gap waveguide designed with improved performance and used. A fifth order Chebyshev bandpass filter is designed, fabricated and measured. The performance of the designed filter is compared with a rectangular waveguide filter to understand the benefits and drawbacks of the geometry. Moreover, classic bandpass filters with transmission zeros at finite frequencies using this technology are designed for the first time. Sample models for triplet and quadruplet sections are proposed and optimized.

In Chapter 3, a new concept of printed planar technology is introduced for efficient TEM bandpass filters in the millimeter-wave band. The new technology is self-packaged and shows great insertion losses compared to microstrip filters. The designs are based on the newly introduced ridge gap waveguide, which is composed of printed parallel-plate waveguide surrounded by beds of mushrooms that suppress the signal around the waveguide. Several examples are designed, optimized, and measured. All-pole bandpass filters and filters with finite transmission zeros are proposed and studied. The performance of the proposed designs is compared to microstrip filters with different packaging options. Also, an efficient transition from microstrip to printed ridge gap waveguide (PRGW) is developed and used in the circuits. The proposed circuits are low cost and realizable using conventional PCB technology. Measured results show good agreement with the analyses.

In Chapter 4, an improved concept is introduced to facilitate the design of low-loss planar circuits using printed gap waveguide technology. The method is based on using separate layers to realize the EBG cells and the lines. As a result, the operating bandwidth of the waveguide is increased compared to the printed ridge gap waveguide. Also, the design process is simplified regarding the placement of the cells around the resonators

and lines. Measured results of a line with two 90º bends and a quadruplet bandpass filter are presented that prove the concept. Also, the design of bandstop filters using the new proposed PRGW is discussed.

In Chapter 5 a new method is proposed for the design of large-scale, wide band resonator-coupled bandpass filters and diplexers. Corrected group delay responses of sub-circuits in combination with space mapping are used to compute the physical dimensions from the coupling matrix model. The coupling matrices are designed using the available theories. The method is based on dividing the structures into many sub-circuits and calculating the group delay responses of the reflection from which the coupling parameters and cavities' resonant frequencies can be extracted. Using a linear space mapping, we optimize the structures efficiently. Bandpass filters and diplexers with bandwidths up to approximately 22% have been designed successfully using the proposed method. A novel stacked cascaded quadruplet filter has been designed by this method. The design of wideband all-pole filters and diplexers are addressed in the paper. The concentration of this chapter is on waveguide technology to prove the effectiveness of the method. In the next chapter, direct application of the proposed method is observed to design a highly efficient and integrated module.

Chapter 6 presents a unique configuration to integrate diplexers and power dividers. The proposed configuration is based on coupling matrix and is realized on RGW. The design of the lumped element network is based on the addition of an extra term to the conventional error function of the coupling matrix to decouple the two ports of the power divider. The optimized lumped element network is implemented successfully on RGW using the method explained and developed in Chapter 5. Later on, the optimized design is used to realize an efficient, compact and novel module that integrates the diplexers and antenna arrays. Finally, a seventh order channel diplexer incorporated into the feed network of the antenna array is presented at Ka-band.

Chapter 7 concludes the thesis.

Chapter 2.

Bandpass Filters in Ridge Gap Waveguide

One solution to overcome the aforementioned problem of the electrical contract explained in Chapter 1 is to use structures that tolerate electrical connection between different parts of the device. Many designs have been proposed from the 1980s as NRD waveguide [1] and recently as ridge gap waveguide [3]. The ridge gap waveguide looks like a suitable candidate for millimeter and submillimeter band guiding structure for realizing microwave components, which is based on using electromagnetic band gap (EBG) in the parallel-plate waveguide to suppress propagation in all directions except in the desired one. The design and behavior of EBG surfaces were thoroughly studied in [5].

In [12] some cavities were proposed in a bed of nails forming an EBG surface to design bandpass filters without using any electrical connection. In [16], further studies were performed to characterize these cavities. Another design was presented in [11] for multiplexer filters using this technology with waveguide excitation. Also, a prototype was fabricated and measured in [17] for V-band applications. In all cases, the filter was not tuned even in the simulation model and also the measured results were even more distant from the designated transfer function. The problem arises from the fact that the bed of nails EBG surface has too many structure details and sharp edges, which makes it computationally expensive. Hence, optimization directly in a full-wave electromagnetic solver is not possible, as it will be very slow and most probably will be trapped in local minima. Also, a design of diplexer is proposed in [18], which suffers from the same issue.

In this chapter, we used an efficient, fast converging optimization method to design coupled-cavity filters that are realized in defected EBG surfaces. The proposed method is based on space mapping [14] using the coupling matrix (CM) as the coarse model, which converges in few iterations. The method is used to design a few classic bandpass filters in RGW technology.

Initially, a fifth order all-pole bandpass filter is designed, fabricated and measured. In this prototype, a new coaxial transition to the ridge gap waveguide is designed, which

has lower insertion loss and higher bandwidth compared to the classic design in [4]. The coupling mechanism between cavities is studied. A new mechanism to control input/output coupling is proposed and studied. The effect of electrical contact and leakage loss and comparison with conventional rectangular waveguide filters are discussed. To overcome the fabrication error, which caused disagreement between simulated and measured results in [12], and [11], tuning screws are used in the fabrication of a fifth order Chebyshev bandpass filter with center frequency of 11.59 GHz and 100 MHz bandwidth. Later, new configurations are proposed to realize bandpass filters with transmission zeros (TZs) at finite frequencies. Two triplet filters have been designed for a millimeter-wave band with TZ on the lower and upper side of the passband. Finally, a quadruplet section that can provide a TZ on each side of the passband is proposed and efficiently optimized.
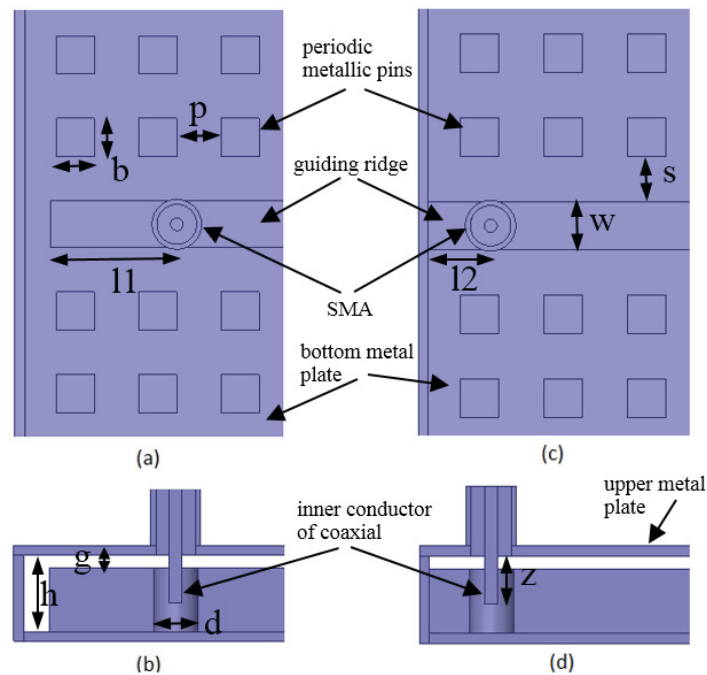
Figure 2-1. **Coaxial to ridge gap transition. a & b) Classical, and c & d) Improved. Parameters are as follow: b=s=3.9 mm, p=4.55 mm, w=4.75 mm, l1=13 mm, l2=6.2 mm, h=6.5 mm, g=1.3 mm, d=4.5 mm, z=3.6 mm.**

2.1. EBG Surface and Coaxial Transition to Ridge Gap Waveguide in X-Band

A design of ridge gap waveguide along with the EBG surface in 10-13 GHz was proposed in [4]. Fundamentally, the design can perform within 7.16-17.13 GHz, which is the band-gap of the parallel EBG surface along with a PEC surface, separated by a small air gap (much smaller than a quarter of a wavelength). However, the coaxial transitions narrow such bandwidth significantly. The new transition is proposed here in which the coaxial SMA is backed by a shorted quarter wavelength line instead of open half wavelength. Both classic and new design are shown in Figure 2-1. The insertion loss is compared for two back to back transitions of both cases as seen in Figure 2-2, which shows good improvement. The total length of the lines is approximately 4.5λ at 11.5 GHz.
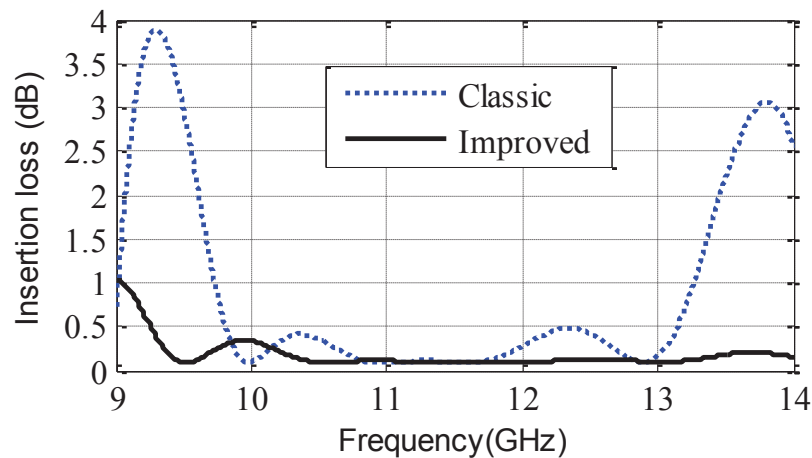
Figure 2-2.   Insertion loss in ridge gap waveguide for classic and improved coaxial transitions.

2.2. Cavities in Defected EBG Surface and Coupling between Them

By removing a few rods in a row from the periodic texture of the EBG surface, high-performance cavities are achieved with a quality factor comparable to conventional TE_{10} cavities in a rectangular waveguide [19]. The Q-factor varies from 6000 using silver as the forming conductor to 4800 for aluminum at 11.59 GHz. Here, poor electrical contact does not decrease the Q-factor as it does for rectangular cavities [19]. More studies were done in [16] regarding the cavities' Q-factor in defected EBG surfaces. Figure 2-3 shows two

cavities coupled to each other by one rod, which is identical to the rods used in the EBG periodic structure. Coupling between these cavities was controlled by changing the height of this rod. The coupling coefficient (ĸ) can be calculated by [20]:

$$\kappa = \frac{f_e^2 - f_m^2}{f_e^2 + f_m^2}$$ (2-1)

where f_e is the resonant frequency of half of the structure when a PEC boundary is placed in between and f_m is the same when a PMC boundary is used. Figure 2-3 shows the coupling coefficient as a function of middle rod's height. Both cavities are designed to have a resonant frequency of 11.59 GHz in the uncoupled situation. As observed, a wide band of coupling bandwidth can be achieved, providing flexibility to design different filter functions.
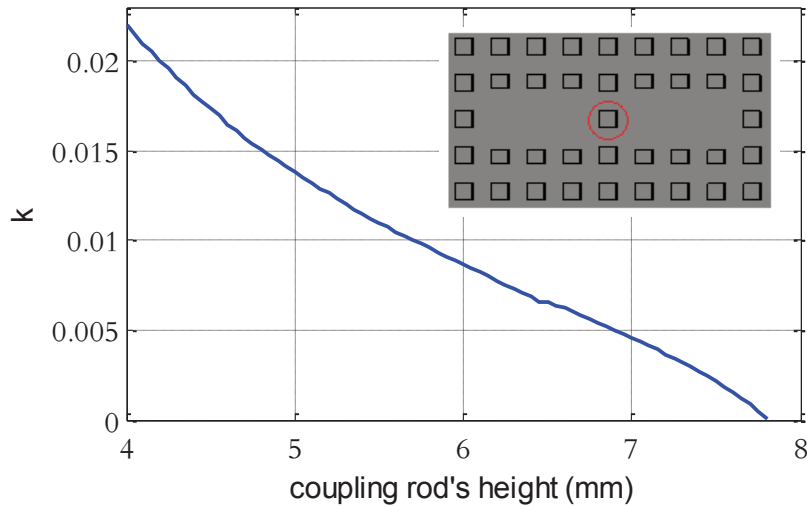
Figure 2-3. **Coupling coefficient as a function of central rod's height. A red circle marks the coupling's rod. The rest of the pins are of fixed height of 6.5 mm.**

2.3. Input/Output Coupling by Using a Tuning Screw

Figure 2-4 shows a ridge gap waveguide terminated into a defected bed of nails cavity. To control the input/output coupling, a screw is used in front of the ridge. The external quality factor (Q_e) of this structure can be calculated using group delay of S_{11} by [20]:

13

$$Q_e = \frac{\omega_0 \tau_m}{4} \qquad\qquad (\text{2-2})$$

where ω_0 is the resonant frequency (rad/sec) of the structure, which can be determined by locating the frequency in which the group delay of S_{11} is maximum. The parameter τ_m is the group delay at ω_0. As seen in Figure 2-5, a large range of coupling can be achieved by this method. Also, the screw has a negligible effect on the resonant frequency.
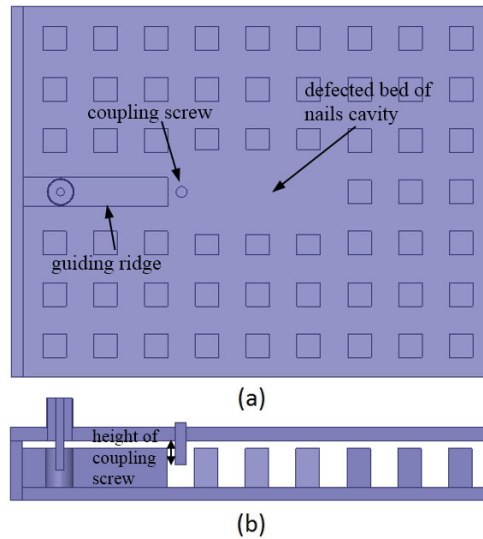
Figure 2-4. **Input/output coupling by using a screw from ridge gap waveguide to defected bed of nails cavity. a) Top view without upper plate, b) Side view.**
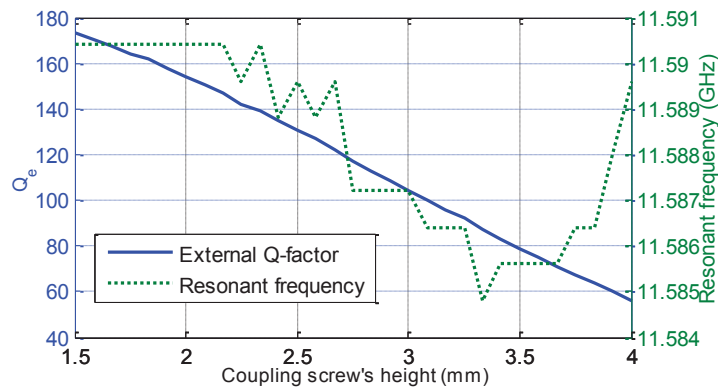
Figure 2-5. **External quality factor and resonant frequency versus coupling screw's height for the structure in Figure 2-4.**

2.4. Filter Design and Optimization Method

To describe the optimization method, a fifth order Chebyshev bandpass filter with center frequency of 11.59 GHz and 100 MHz bandwidth with 20 dB return loss is designed. Coupling matrix parameters are calculated as $R_i = R_o = 1.03$, $M_{12} = M_{45} = 0.8654$ and $M_{23} = M_{34} = 0.6357$. The structure is shown in Figure 2-6(a). For every cavity a tuning screw is assigned in the center. For the input and output cavities other extra screws are used to achieve input and output couplings. The filter design parameters are the width of the cavities (w), height of the middle rods (h), and length of input/output coupling screws (d_i/d_o). In order to control the width of the cavities, we change the size of the surrounding pins in both sides of each cavity. These pins can be larger or smaller compared to other pins in order to excite the cavity in the required frequency (11.59 GHz), which has a negligible effect on the bandgap of whole EBG array.

The optimization method is based on the space mapping technique [14] in which HFSS [21] is used as a fine model and coupling matrix as the coarse model. Here, we used a simple linear mapping between the two spaces. All dimensions of the fine model (w, h, d_i and d_o) have a mapping to the coupling matrix elements. We assign x_f as the vector which contains the parameters of the fine model and x_c as the vector that has the information of the coarse model. The parameter x_c^* is an ideal coupling vector that has the information about the coupling between cavities and the resonant frequencies of the cavities along with the input and output resistances. In the first step, the initial dimensions are calculated and preserved in $x_f^{(n=1)}$. In the following step, the coupling matrix of the response is extracted by using optimization. The initial response is far from the ideal one. Therefore, it is necessary to use a global optimization method such as Particle Swarm Optimization (PSO) [22]. The achieved parameters are saved in $x_c^{(n=1)}$. Then:

$$f = x_c^* - x_c^{(n)}$$

(2-3)

$$deld = f.d$$

d is the mapping vector and *deld* is the dot product of d and f. The new dimensions are calculated by:

$$x_f^{(n+1)} = deld + x_f^{(n)} \qquad\qquad (\,2\text{-}4\,)$$

The process continues until achieving the equi-ripple behavior. How fast the optimization converges depends on how good the mapping vector is chosen. Figure 2-6(b) shows S_{11} for all the steps. Here, in the fifth iteration, the results are converged.

Although personal computers are very powerful and can handle the optimization of conventional filters directly in the EM solver, for the proposed EBG structure it is not an option as it is computationally expensive and previous attempts failed to do so [11], [12], [17], [18].
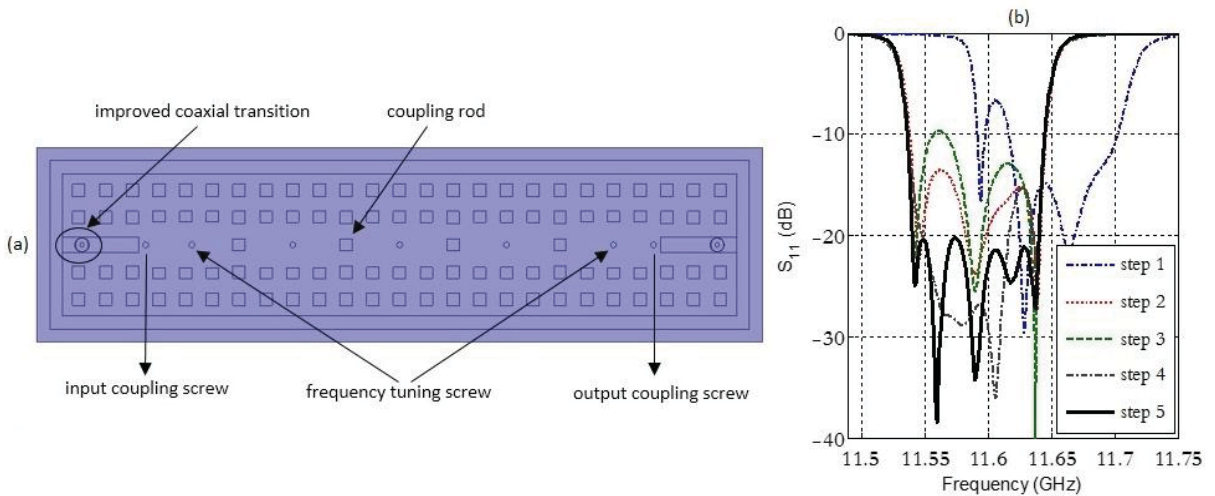
Figure 2-6. **a) Fifth order direct-coupled filter on defected EBG structure with tuning screws. b) The response of fine model in every step of the optimization procedure.**

2.5. Leakage Loss

In this section, a study has been performed to determine the number of the required rows of periodic texture to have good enough PMC boundary condition to avoid leakage loss as the structure is unbounded from the sides. The same filter designed in Section 2.4 is shown in Figure 2-7(a-c) with a different number of periodic texture rows, and the resulting S_{21} is provided in Figure 2-8. As seen, three rows of EBG periodic pins are enough to avoid any radiation. However, by using two rows of pins along with side-

walls the size can be reduced. In this case, the contact between side-walls and the upper plate is not critical. To model the effect of poor electrical contact, a gap between side-walls and the top plate is introduced in the structure with two rows of pins. Insertion loss as a function of the gap in center frequency (11.59 GHz) is plotted in Figure 2-9. Hence, it can be concluded that by using two rows of pins and side-walls, the size of the filter can be reduced and still no careful attention is needed to create perfect contacts. Figure 2-9 also shows the insertion loss for the same filter with three rows of periodic texture. As expected for this case, insertion loss is not affected by the gap between sidewalls and the upper plate, because leakage loss is already reduced to zero by the artificial boundary condition achieved by sufficient rows of EBG pins.

(a)

(b)

(c)

(d)
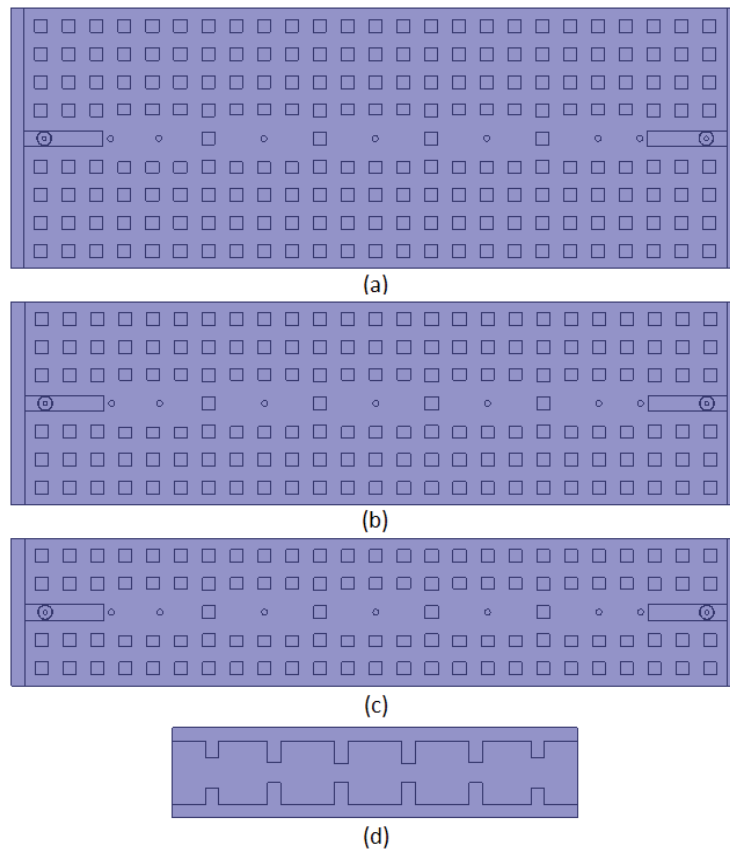
Figure 2-7.   Fifth order Chebyshev filter with a) four, b) three and c) two rows of EBG pins, d) same filter function implanted on the WR-75 rectangular waveguide.
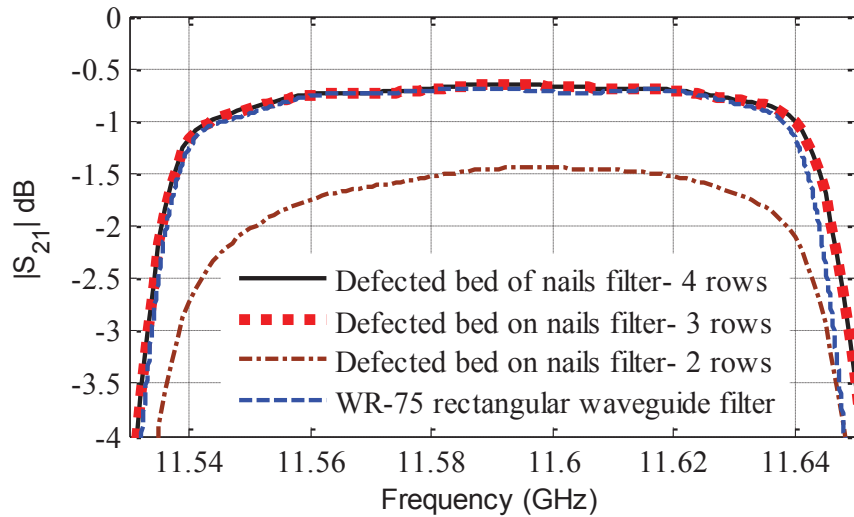
Figure 2-8. Simulated S_{21} of defected bed of nails filter with different rows of pins and same filter function on WR-75 rectangular filter.
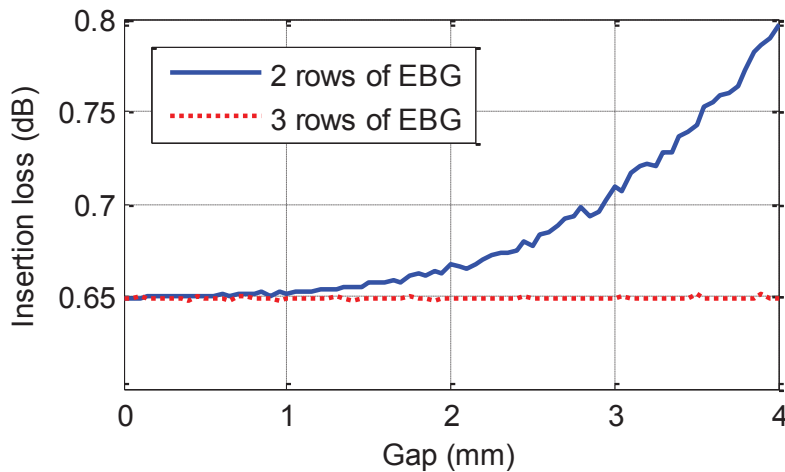
Figure 2-9. Insertion loss in center frequency (11.59 GHz) versus air gap between the upper plate and side-walls for defected bed of nails filter with two and three rows of pins.

2.6. Fabrication, Measurement, and Comparison with Rectangular Waveguide Filter

The tuned filter in Figure 2-6 was fabricated using CNC etching machine on Aluminum. Tuning screws are provided for resonant frequencies and input/output couplings. All the screws for connecting two parts of design are only for mechanical

stability and are not important in the case of creating electrical contact except for the two end sides that are shorting the excitation lines. Measured S-parameters are shown in Figure 2-11 and Figure 2-12, which show excellent agreement with the simulation. Measured insertion loss is 0.72 dB at the center frequency.
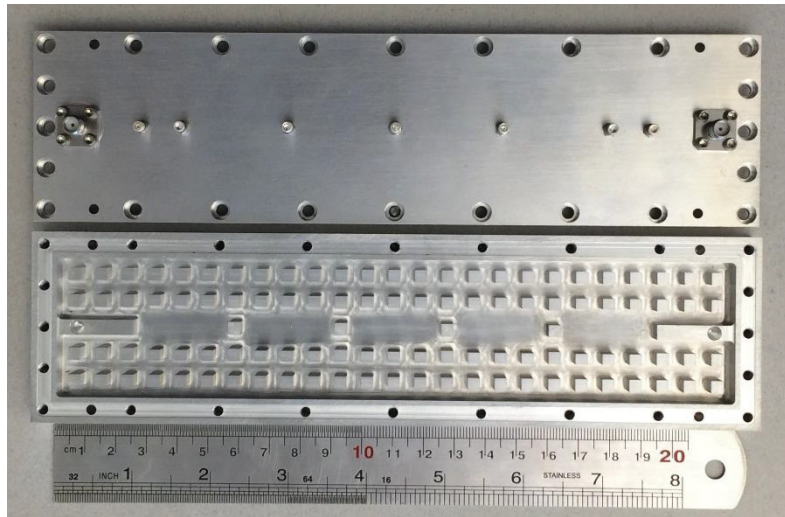
Figure 2-10. **Fabricated model of tuned 5th order Chebyshev filter on defected bed of nails structure. Two rows of periodic pins have been used to create artificial magnetic boundary condition.**
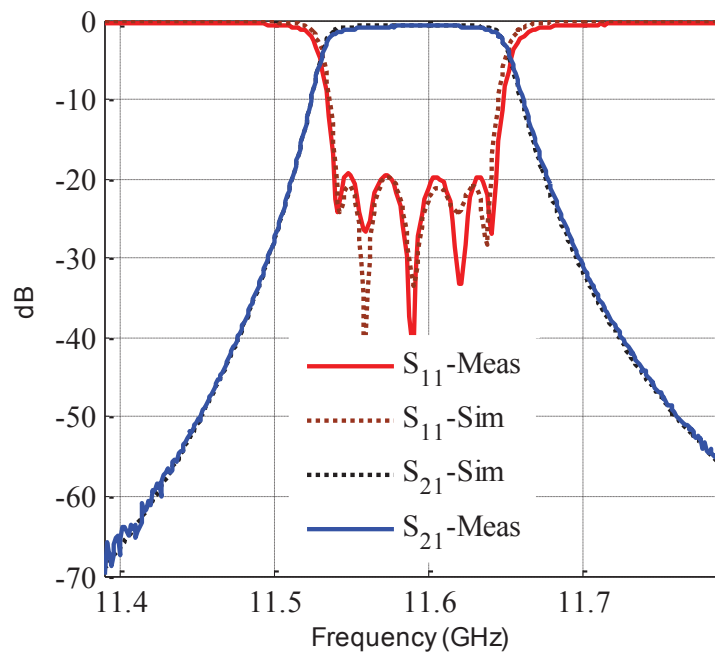
Figure 2-11. **Measured and simulated S-parameters.**
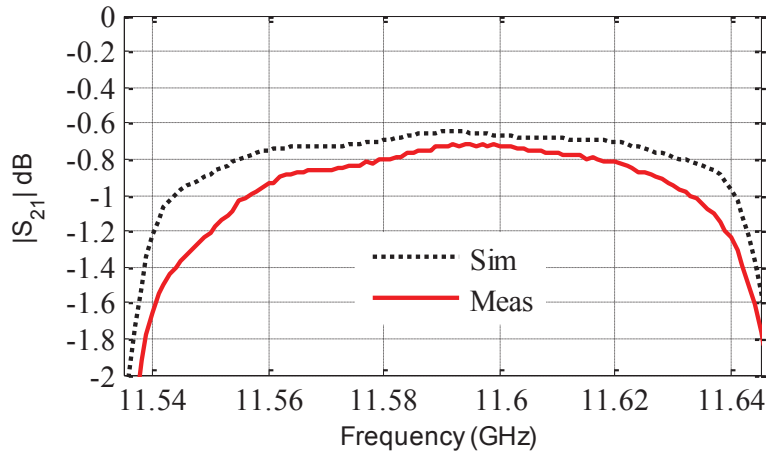
Figure 2-12.   Measured and simulated |S$_{21}$| for band pass filters on defected bed of nails.

To compare the performance of the designed filter with existing technologies, same filter function was implemented on the WR-75 rectangular waveguide in Aluminum (Figure 2-7(d)). As it can be seen in Figure 2-8, the performance of both technologies shows similar insertion loss. However, the size of WR-75 waveguide filter is considerably smaller.

2.7.   Design of Triplet Sections

To achieve better selectivity and higher rejection, it is necessary to design filters with transmission zeros at finite frequencies. In the following two sections, the design of bandpass filters with TZs at finite frequencies in RGW technology is discussed. All the designed examples have the passband in 34.75-35.25 GHz with 20 dB return loss. For this bandwidth, a new EBG cell has been designed which is shown in Figure 2-13 along with its dimensions and dispersion diagram. As it can be seen, the EBG cell has a bandgap at 22-44 GHz.

One classic filtering section with this capability is the triplet that is defined as a third order filter that can provide a TZ either on the right side of the passband or the left. The position of the TZ can be controlled by the cross-coupling between Resonator 1 and 3. A triplet section in RGW technology is shown in Figure 2-14. In the proposed geometry, all the resonators are performing in the same mode which is equivalent to the TE$_{101}$ mode

20

of the rectangular waveguide. Such a configuration results in a cross-coupling (M_{13}) with same sign compared to the direct couplings (M_{12} and M_{23}). By doing so, the TZ is located on the lower side of the passband. Similar to the previously designed filter, the couplings are controlled by the height of adjacent pins. These pins are marked in Figure 2-14. Resonant frequencies of the cavities are controlled by shifting the pins around them as can be seen in Figure 2-14. To avoid using any tuning screw, we used another mechanism to control the input/output couplings by adjusting the length of the lines that perturb Resonator 1 and 2. Using (2-2) external quality factors related to input/output couplings can be calculated.
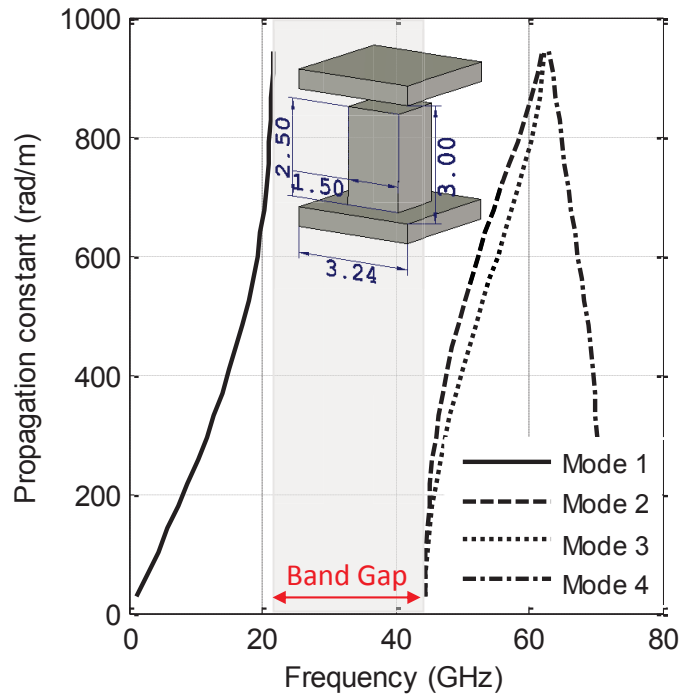
Figure 2-13.   Dispersion diagram of the EBG unit cell. Dimensions are in mm.

The optimized response of the triplet section in Figure 2-14 is simulated and presented in Figure 2-15 along with the response from the extracted CM. Minimum simulated insertion loss is 0.43 dB using Aluminum as the constructing material. The extracted CM is calculated as:

$$M = \begin{bmatrix} -0.0676 & -0.9104 & -0.4330 \\ -0.9104 & 0.4051 & -0.9319 \\ -0.4330 & -0.9319 & -0.0908 \end{bmatrix} \qquad (\text{2-5})$$

21

With $R_1 = R_2 = 1.1674$.
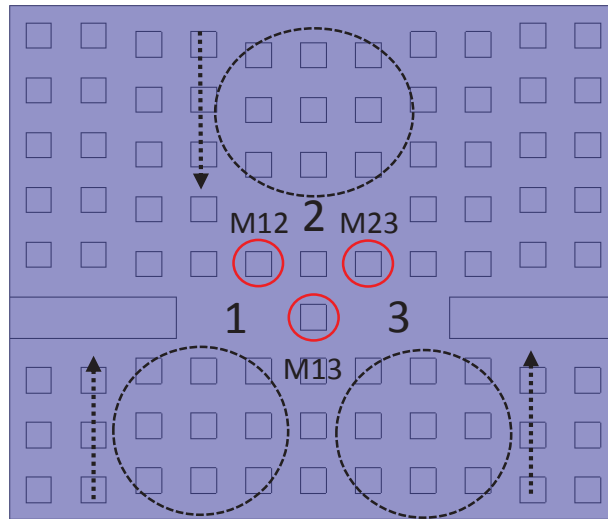
Figure 2-14. Triplet section filter with TZ on the lower side of the passband. Arrows show the direction that pins are shifted for each cavity to tune the resonant frequency.
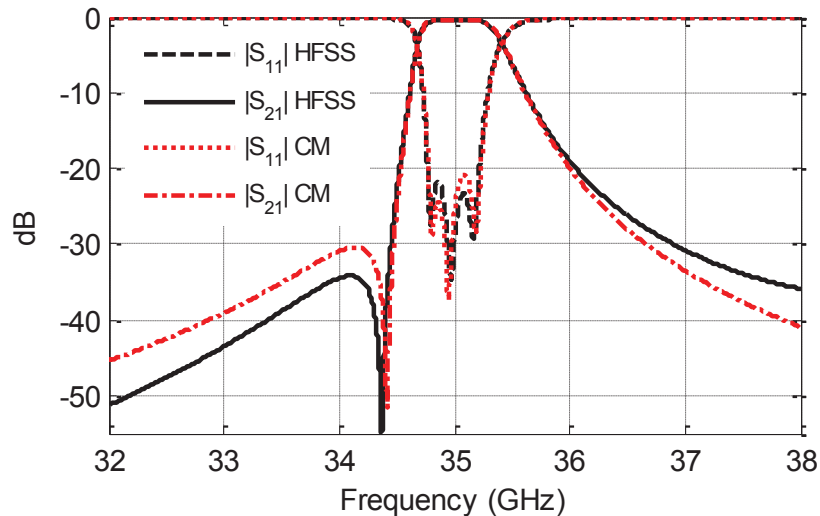
Figure 2-15. Simulated response of the triplet section in Figure 2-14. Response from the extracted CM is also shown.

To move the TZ to the upper side of the passband, the relative sign of M_{13} should be changed by using an oversized cavity for Resonator 2. By exciting Resonator 2 in the TE_{102} mode, the magnetic field changes sign once inside Resonator 2. As a result, M_{13} changes to positive and based on the CM theory, this yields a triplet section with the TZ on the upper side of the passband. To control the couplings, same methods from the

previous example are used. An optimized simulated response along with the response from the extracted CM are shown in Figure 2-17. Minimum simulated insertion loss is 0.4 dB. The extracted CM is calculated as:

$$M = \begin{bmatrix} 0.0376 & -0.9506 & 0.4296 \\ -0.9506 & -0.4472 & -0.9476 \\ 0.4296 & -0.9476 & 0.1237 \end{bmatrix}$$

(2-6)

with $R_1 = R_2 = 1.1416$.
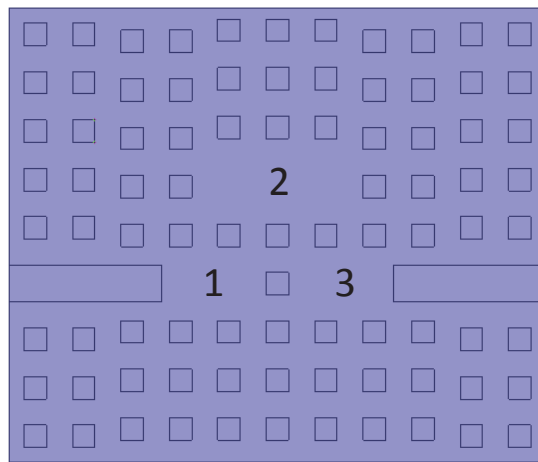
Figure 2-16.   Triplet section filter with TZ on the upper side of the passband. Resonator 2 is excited in TE$_{102}$ mode.
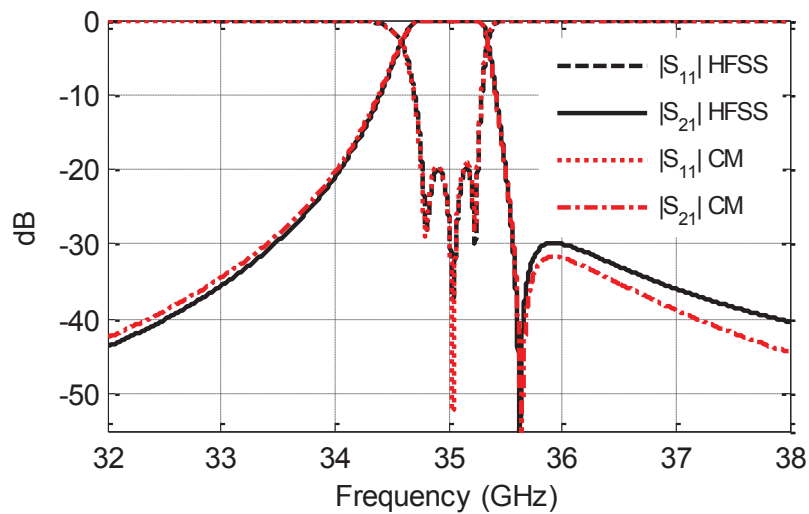
Figure 2-17.   Simulated response of the triplet section in Figure. 16. Response from the extracted CM is also shown.
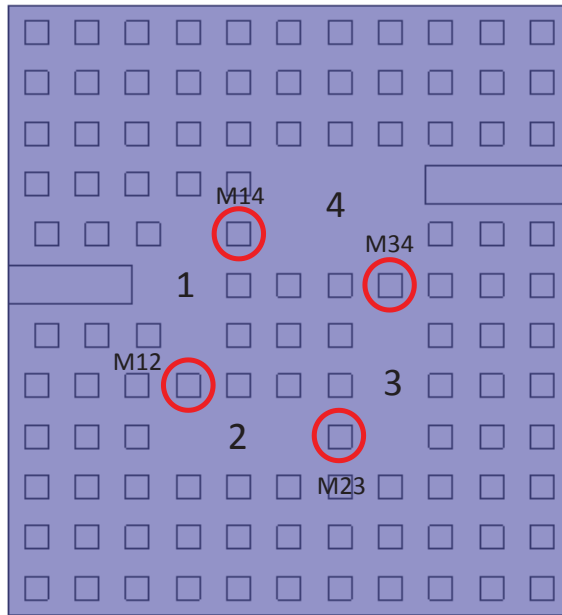
Figure 2-18. Quadruplet filter with symmetric response in RGW technology.
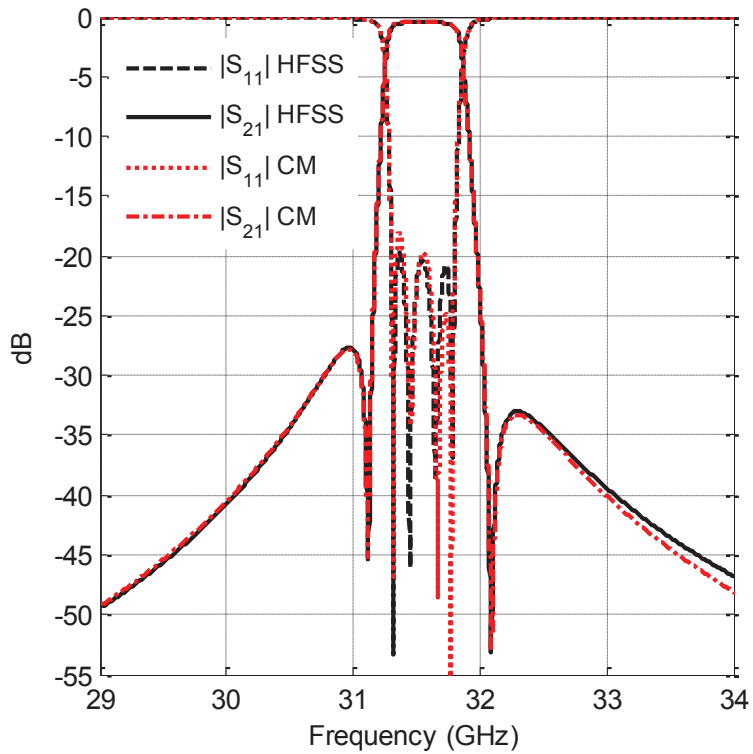
Figure 2-19. Simulated and extracted response for the quadruplet bandpass filter.

2.8. Design of Quadruplet Section

Here, the design of a quadruplet filtering section in RGW technology is discussed. A quadruplet section is a 4th order filter that can provide two TZs at finite frequencies. Here, we only discuss the realization of the filter with the symmetric response, which means a filter with a TZ on the lower side and another one on the upper side of the passband. Such a quadruplet filter can be realized with a single positive cross-coupling between Resonator 1 and 4. Similarly, this can be done by using an oversized cavity for Resonator 4. The geometry of the filter is shown in Figure 2-18. The pins that control the couplings are marked in the sketch. After the optimization of the circuit using the proposed method in Section 2.4, the final simulated response and the response from the extracted CM is calculated and shown in Figure 2-19. The extracted CM is:

$$M = \begin{bmatrix} -0.062 & -0.8733 & -0.0511 & 0.1827 \\ -0.8733 & 0.0448 & -0.7670 & -0.0497 \\ -0.0511 & -0.7670 & 0.0260 & -0.8527 \\ 0.1827 & -0.0497 & -0.8527 & -0.0444 \end{bmatrix} \qquad (2\text{-}7)$$

with $R_1 = R_2 = 1.0629$. It is noticed that the response of the filter is not completely symmetric due to the parasitic couplings between Resonator 2 and 4 and also between Resonator 1 and 3. Ideally, this pair of resonators should be completely isolated to achieve an entirely symmetric response. In the proposed structure in RGW technology, this isolation is implemented using three pins between them. These pins can eliminate any unwanted coupling as shown in the extracted CM in (2-6). The negligible remaining cross-couplings in $M_{13} = -0.0511$ and $M_{24} = -0.0497$ are causing the slight asymmetry as can be seen in Figure 2-19. The minimum simulated insertion loss is 0.45 dB.

2.9. Conclusion

In this chapter, a complete investigation on the design, optimization and realization of the bandpass filters in an RGW and defected bed of nails cavity technology has been presented. In waveguide technology, where cavities are machined and require to be shielded by another metal piece, electrical contact is critical to provide the required shield.

Gap waveguide technology eliminates the need for such electrical contact. Optimization of the circuits has been performed using a space mapping technique. This class of filters requires high computational efforts that make it impossible to optimize the design directly using a full-wave EM solver. Several geometries have been proposed for the realization of all-pole filters as well as filters with cross-couplings. The coupling mechanism between the cavities has been analyzed thoroughly. A new improved coaxial excitation and input/output coupling mechanism have been proposed and used for ridge gap waveguide at the filter input/output. The performance of the designed filter in the defected bed of nails EBG technology has been compared with conventional rectangular waveguide filter and found to be comparable in performance. Results have proven that defected EBG cavities can be a good candidate to be used in the millimeter band for filter devices.

Chapter 3.

Low-loss Planar Bandpass Filters for Millimetre-band Application using Printed Ridge Gap Waveguide

3.1. Introduction

Microstrip filters are a desirable solution for the millimeter frequency band, due to their low-cost production, small size and low weight, and dispersion-less propagation characteristics. However, despite numerous advances in PCB RF materials and circuit printing techniques, microstrip filters suffer from high insertion loss, especially in the millimeter-wave band. Two major reasons are radiation losses and dissipation of the materials. Radiation losses can be eliminated by using a metallic packaging box. However, the overall size of the filter becomes considerably larger and bulky. Regarding the dissipation of the RF substrates, in spite of considerable efforts and innovations for creating low-loss materials, the related losses are not acceptable for many applications. Therefore, a new planar TEM technology is required to address the rising demand for communication systems in millimeter-wave bands. Also, it should have the advantages of printed circuit technology and overcome their unacceptable loss behavior.

Gap waveguide technology as a metamaterial based guiding medium that doesn't need electrical contact with air-filled propagation environment can be considered as a suitable candidate for millimetre-band applications. In the original prototypes of the ridge gap waveguide, which were fabricated using CNC machine, periodic metallic pins create the EBG cells. Few examples of such a representation of gap waveguide were shown in Chapter 2. Few articles exist in the literature about bandpass filter designs based on this technology [11]–[13]. Recently, the printed version of the ridge gap waveguide (PRGW) was introduced [23], and some measured results were provided for antenna feeding applications at 60 GHz [8]. In this case, the unit cells are created by conducting plated vias topped by microstrip patches (mushroom) that can provide the desired band gap. The capabilities of this new technique are promising since the structure is light and low-cost and the performance regarding the loss is incomparably better than the

conventional microstrip transmission line technology. Realization of a guiding structure with air medium that doesn't need electrical contact and can be fabricated by PCB technology is a step forward in the microwave industry that needs to be promoted in all aspects of microwave design.

In this chapter, we developed the resonators and a coupling mechanism to have gap-coupled bandpass filters using the printed ridge gap waveguide technology. Initially, all-pole bandpass filters will be addressed, and two prototypes are designed and fabricated. Later on, filters with finite transmission zeros will be proposed. Measured results on triplet and quadruplet sections will be presented. An efficient transition between the microstrip line and PRGW is proposed and used in all the examples to be able to use a probe test connector for measurement of the circuits. It is possible to integrate these designs easily with printed circuit technology. In the last section of this chapter, the performance of these filters is compared to conventional microstrip filters. It is tried to investigate the concept, characteristic, and propagation in PRGW in depth along with the design guidelines. Since PRGW is a computationally expensive structure, design and optimization of the circuits have to be carried out efficiently with a minimum number of full-wave iteration of the complete structure. Therefore, several techniques are developed during this work which will flow during this chapter. These techniques will cover several pivotal rotations in order to transform the extracted coupling matrix to the correct geometry. In addition, the quality factor of different configurations of PRGW resonator is calculated and compared to microstrip cavities.

3.2. Construction of Printed Ridge Gap Waveguide and Transition to Microstrip

The printed ridge gap waveguide consists of quasi-periodic unit cells that along with the upper metallic plate creates the electromagnetic band gap structure (EBG), and a metallic strip that creates the parallel-plate TEM waveguide. The dispersion diagram of the unit cell is shown in Figure 3-1. The unit cell is a circular patch that is grounded using a plated via hole. Several factors can affect the bandgap. A detailed study to investigate these effects can be found in [5]. Here, the unit cell is designed to cover around the 20-40 GHz band. The parallel-plate part is inserted between the mushroom cells. It is important

to mention that the bottom of parallel-plate should be grounded using the plated vias to make sure that propagation only exists inside the air-gap. In this case, we call it printed ridge gap waveguide (PRGW) as shown in Figure 3-2 along with the dispersion diagram of the complete structure. The dispersion diagram in Figure 3-2 indicates that within the EBG of the cells, a single mode can propagate due to the existence of the ridge, which is close to the light line. Therefore, it is called a quasi-TEM mode. The operating frequency band of the guide is almost the same band gap of the unit cell shown in Figure 3-1. It can be seen that the band gap of the cells is a little smaller when emerged in the semi-periodic environment of the PRGW.
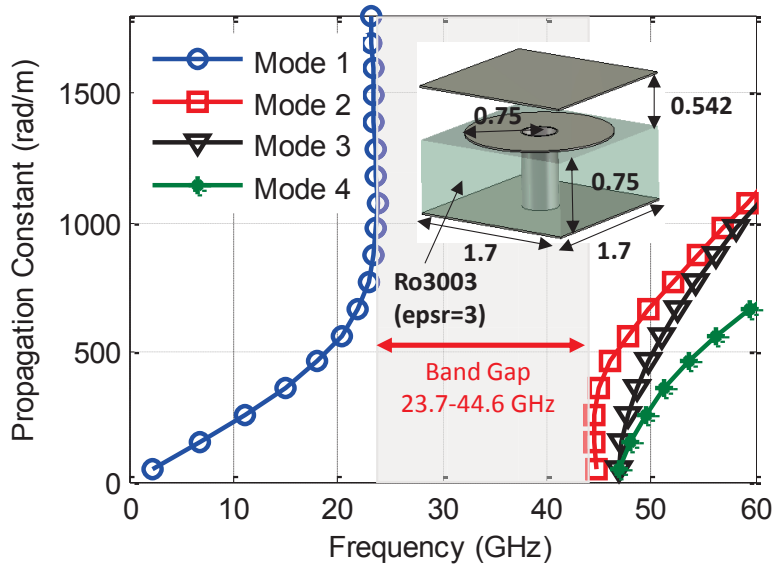
Figure 3-1. Dispersion diagram of the periodic plated vias topped with circular patches along with an upper metallic plate. Dimensions are in mm.

Since PRGW is not a standard technology that can be launched directly with standard measurement equipment, we designed an efficient transition from microstrip to PRGW. The transition is shown in Figure 3-3. The structure is kept very simple. The basic idea is to have 50 Ω lines in both microstrip line and PRGW. As the microstrip is printed over a dielectric material with ε_r = 2.2, its width will be narrower compared to PRGW line in which the propagation is in the air-gap. Figure 3-4 shows the simulated scattering parameters of the circuit in Figure 3-3. The thickness of the microstrip substrate is 0.508 mm. The selected parallel-plate air-gap is 0.542 mm, which is larger than the dielectric substrate thickness due to added thickness of the copper cladding. One important factor

that should be investigated is the required number of mushroom rows of cells in order to suppress and attenuate the signal away from the guiding ridge. In Figure 3-5, the insertion loss is simulated for different cases of PRGW launched with the microstrip transition using a different number of mushroom rows of cells around it. It is observed that three rows of these cells on each side of PRGW are enough to suppress efficiently any leakage since there is no considerable difference between using three or four rows of cells. The length of the PRGW line is approximately 2λ at 30 GHz. It should be stated that a considerable part of the insertion loss is due to the microstrip input/output lines.
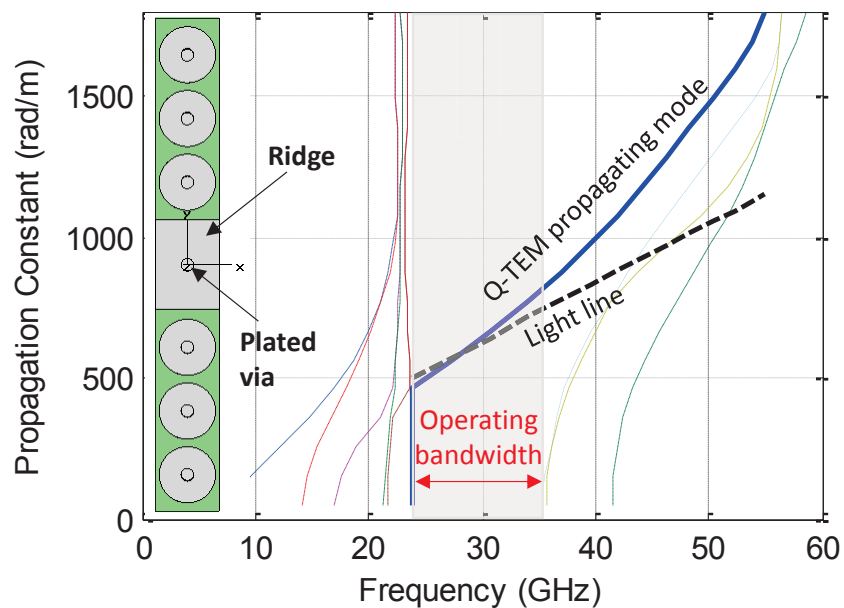
Figure 3-2. **Dispersion diagram of printed ridge gap waveguide. The structure is periodic in the x-direction. The metallic top plate is not shown.**

Ideally, there is electrical contact between the microstrip line and the parallel plates. However, this contact is not critical to the performance of the transition. In practice, there would be a small air-gap between them as shown in Figure 3-6(a). We studied its effect on the insertion loss of the whole structure. Figure 3-6(b) illustrates the effect of the undesirable air-gap in the insertion loss at 30.5 GHz, which is the center frequency of the structure. It is observed that for gaps smaller than 25 µm, the transition still has a good performance. The following measured results that will come in this chapter show the fact that by using sufficient pressure, maintaining such circumstances is not a difficult task.
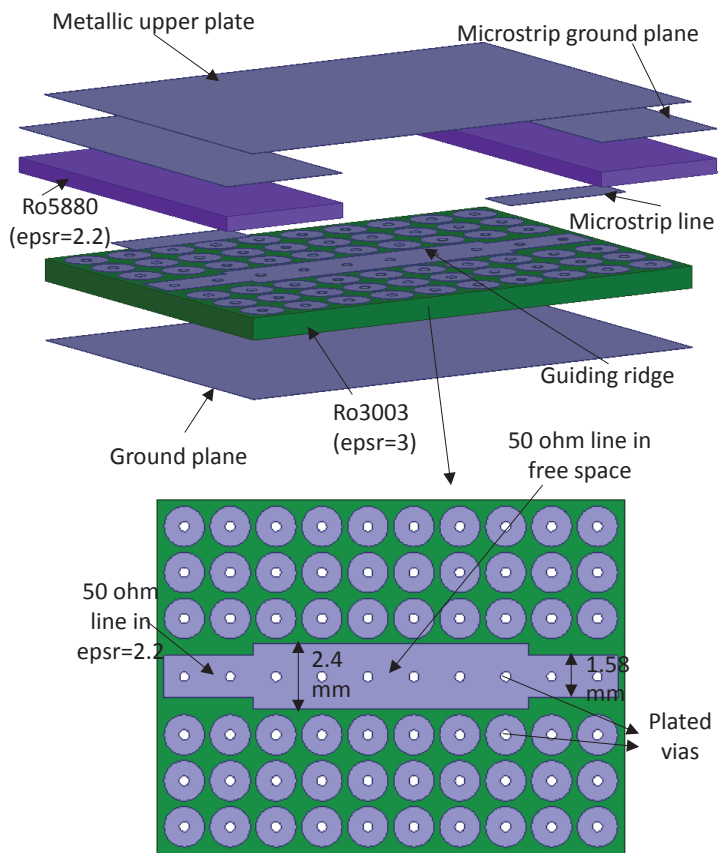
Figure 3-3. Microstrip to printed ridge gap waveguide transition. The top is the detail of the structure layers that are made of two dielectric substrates, and the bottom is the view of the printed layer for the ridge and the mushrooms top.
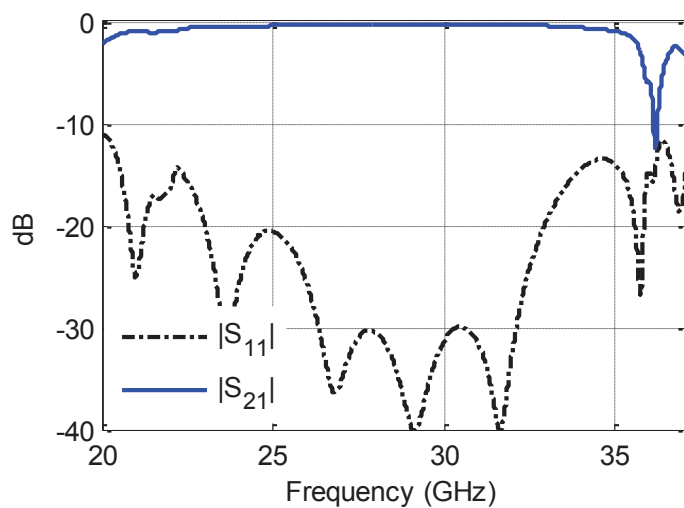
Figure 3-4. Simulated response of transition from MS to PRGW line.
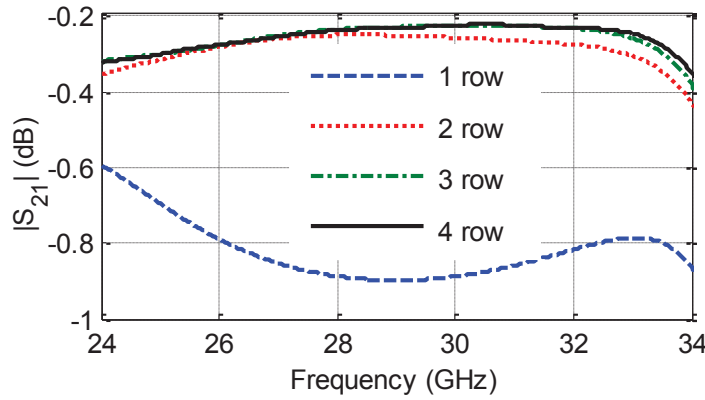
Figure 3-5. The magnitude of S_{21} of the microstrip to PRGW transition for a different number of EBG rows around the ridge.

3.3. Characterizing the Capacitive Gap Coupling Discontinuity in PRGW

The first step to design gap coupled bandpass filters with the new PRGW technology is to model the gap discontinuity as an admittance inverter structure. This can be done similar to microstrip filters. For this, several examples and methods can be found in the literature [24], [25]. The important point that needs to be considered is the compensation of the phase offset of the simulated results to obtain the accurate admittance parameters for the gap discontinuity. For the structure given in Figure 3-7, phase compensation should be performed in two steps, as the propagation constant is different inside the microstrip input/output lines and the air-gap of the PRGW. The shift to the first reference plane is performed numerically using the simulator. Then the corrected phase of the S-parameters (at reference plane 2) is:

$$\angle s_{ij}' = \angle s_{ij} + (lt - g) \times \beta. \tag{3-1}$$

where s_{ij} is the S-parameters at reference plane 1, and β is the propagation constant extracted at the desired frequency from the dispersion diagram in Figure 3-2. Other parameters are defined in Figure 3-7. Now, the corrected S-parameters can be converted to Y-parameters. The susceptances of the equivalent model in Figure 3-7 are:
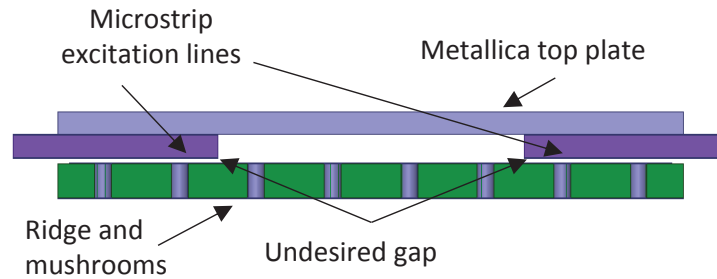
(a)
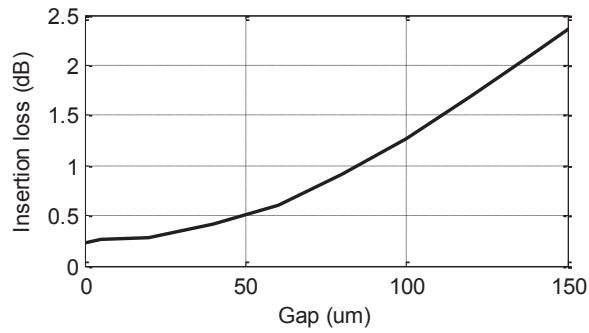
(b)

Figure 3-6.   **a) Cross section of microstrip to PRGW transition with the undesired gap between the lines. b) Insertion loss versus the gap size at 30.5 GHz.**

$$B_p = -\text{img}\,[Y_{21}]$$ (3-2)

                                                                        (3-3)
$$B_s = \text{img}\,[Y_{11}] + \text{img}\,[Y_{21}]$$

Y_{ij} is the corrected admittance parameters of the gap discontinuity. Using (3-2) and (3-3), we plot the capacitances for C_s and C_p at 30.5 GHz as shown in Figure 3-8. It is important to note that as the gap gets wider than a certain width (1.25 mm), inductive behavior replaces the capacitive behavior of C_s. The reason for this is the fact that in our model, the vias' position are fixed. Therefore, the edges of the gap get close to the vias as the gap width increases, which causes C_s to show an inductive behavior. As the required gap is much smaller, this change from capacitive to inductive behavior is not an issue.

33
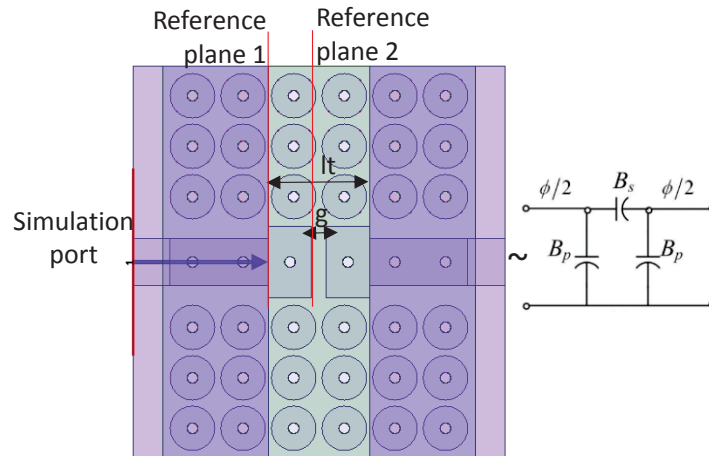
Figure 3-7. Gap discontinuity in PRGW.
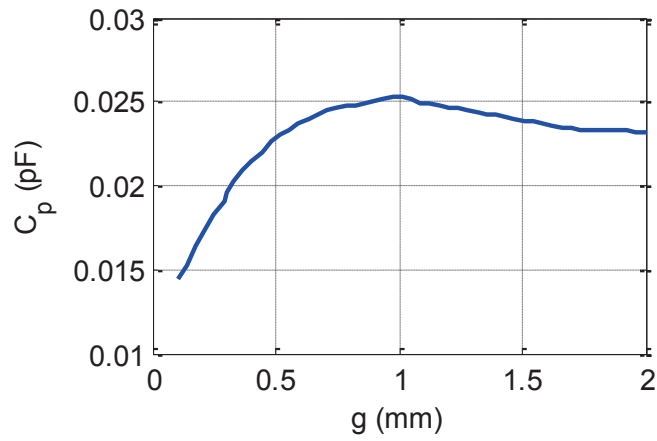
(a)
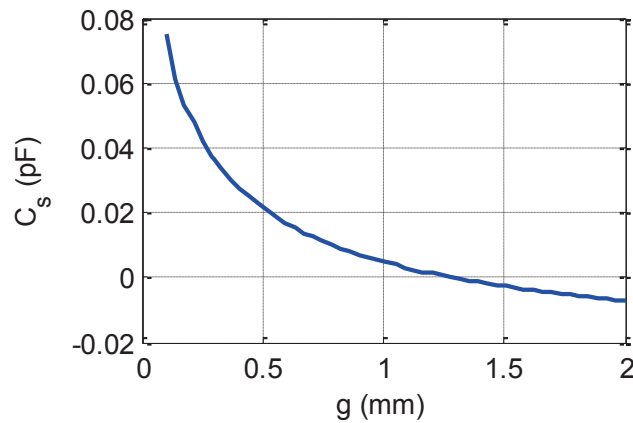
(b)

Figure 3-8. Calculated capacitances for the model of the gap discontinuity in Figure 3-7 at 30.5 GHz.

3.4. In-Line Chebyshev Filters

All the designed examples in this chapter are bandpass filters in 30-31 GHz with 20 dB return loss. The first prototype is a third order Chebyshev filter with the geometry shown in Figure 3-9. The resonators are half-wavelength lines that are coupled using the gap discontinuity introduced in Section 3.3. The procedure of finding the gap and resonator dimensions from Chebyshev coefficients using the capacitances in Figure 3-8, is a straightforward procedure and can be found in many references as [20], [24], [25]. It should be stated that all simulated structures include the microstrip excitation lines as depicted in Figure 3-3. The initial response of the structure in Figure 3-9 is shown in Figure 3-10. As expected, some optimizations are required to achieve the prescribed performance. This is due to the fact that the relative position of each gap discontinuity regarding the cells varies for each coupling gap and depends on the length of each resonator. Here, we used space mapping [14] in combination with the coupling matrix extraction method outlined in [26] as the course model. First, the coupling matrix of the initial response in Figure 3-10 is extracted. Later, a mapping is used to relate the CM to the length of the lines and gap dimensions. Here, we used a linear mapping by analyzing the sensitivity of the resonators and couplings. Depending on how accurate the extraction procedure and mapping are performed, the optimization will converge in few iterations. Since the PRGW environment is more complicated and computationally expensive than other structures, it is important to be able to optimize the design in a timely manner. The photo of the fabricated parts of this filter after optimization is shown in Figure 3-11. The optimized responses along with the measured results are shown in Figure 3-12. The minimum measured insertion loss is 0.8 dB. It is important to note that in the measurement, the reference plane is moved away from the connectors as shown in the insert photo in Figure 3-12. The extracted CM of the filter is:

$$M = \begin{bmatrix} 0 & 1.0283 & 0.015 \\ 1.0283 & 0 & 1.012 \\ 0.015 & 1.012 & 0 \end{bmatrix}$$ (3-4)

with $R_1 = R_2 = 1.2041$. Only the real part of the CM is shown and used in the design process. The optimized dimensions of the circuit are shown in Table 3-1. The cell size and period are same as in Figure 3-1.
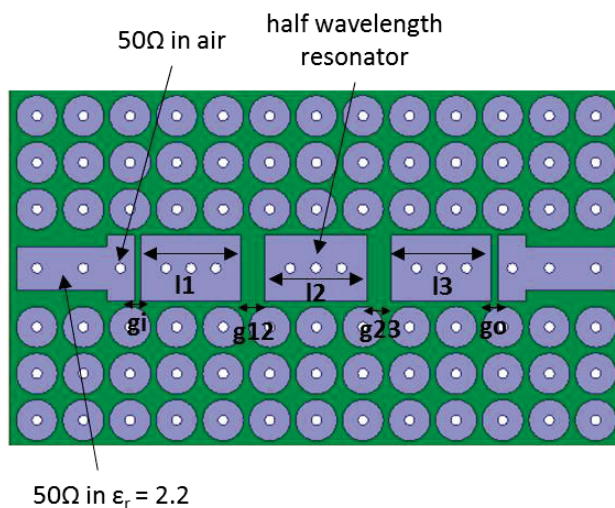
Figure 3-9. Third order Chebyshev bandpass filter in PRGW. Only the PRGW section is shown. The upper plate and MS lines are placed as illustrated in Figure 3-3.
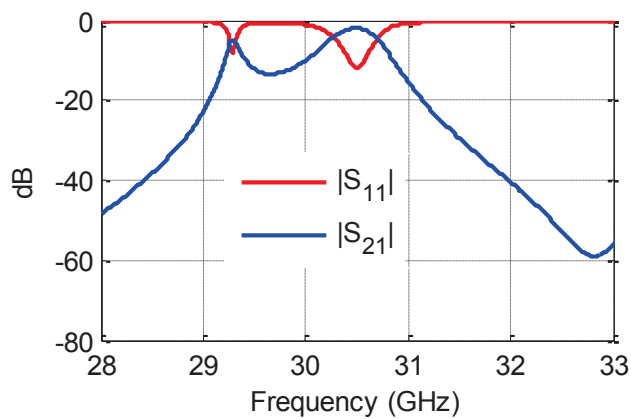
Figure 3-10. The initial response of third order bandpass filter of the structure in Figure 3-9.

Table 3-1. Optimized parameters of third order PRGW filter in Figure 3-9.

Parameter	Value (mm)	Parameter	Value (mm)
l1=l3	3.6486	gi=go	0.2404
l2	3.7256	g12=g23	0.8737

Layer 1:
lines, cells and vias

Layer 2:
MS excitation and
spacer

Layer 3:
top plate
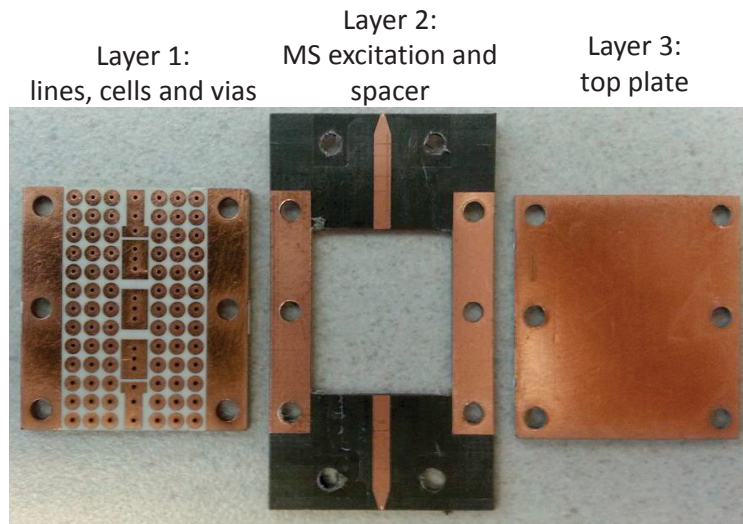
Figure 3-11. Fabricated third order bandpass filter in PRGW technology.
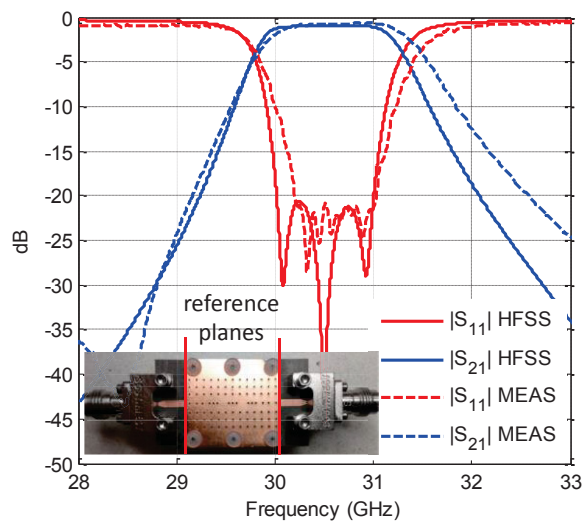
Figure 3-12. Simulated and measured results for third order PRGW bandpass filter. Fabricated filter assembled in 1.85 edge launchers is shown in the inserted photo. The reference planes of measurement also are shown.

Even though the concentration of this chapter is the loss behavior of planar bandpass filters, it might be of significance to discuss the rejection bandwidth of PRGW filters. PRGW filters have a limited rejection band due to the limited bandgap of the structure. Away from the single mode operating frequency band calculated in the dispersion diagram (Figure 3-2), parallel-plate guiding modes appear in the structure that ruin the rejection of the filter. We did not try to improve the rejection of this filter. The filter's

rejection can be improved by designing the cells with wider stopband. For this purpose, smaller air-gap should be used to reach to the desired rejection bandwidth. This feature of PRGW filters can be compared to waveguide filters which have a limited frequency band where single mode operation is present. However, using the appropriate unit cell configuration, the rejection bandwidth can encompass a variety of applications. Also, in Chapter 4 another solution is proposed to resolve this issue.

This filter is compared with another practical third order filter using microstrip technology as given in Section 3.8 to appreciate the PRWG technology. The microstrip filter requires proper packaging that increases its volume size.

The next example is a fifth order Chebyshev filter shown in Figure 3-13. The fabricated components of the prototype are shown in Figure 3-14. The design procedure is the same as the previous example with only one extra step. During the extraction of the coupling matrix from the simulated S-parameters, it is necessary to convert the full extracted matrix to in-line form. For this purpose, we calculated series of rotational angles and pivots. They are listed in Table 3-2. The optimized simulated and measured response of the fifth order filter is shown in Figure 3-15. The full extracted CM of the optimized filter is:

$$M = \begin{bmatrix} 0 & 0.4707 & 0.6166 & 0.3736 & 0.011 \\ 0.4707 & 0.8422 & 0 & 0.282 & 0.4822 \\ 0.6166 & 0 & 0 & 0 & 0.6165 \\ 0.3736 & 0.282 & 0 & 0.8898 & 0.3753 \\ 0.011 & 0.4822 & 0.6165 & 0.3753 & 0 \end{bmatrix} \qquad (\,3\text{-}5\,)$$

This CM is not usable in the optimization procedure since it does not obey the direct inline configuration. After applying the pivots, the CM transforms to:

$$M = \begin{bmatrix} 0 & 0.8609 & 0 & 0 & 0.011 \\ 0.8609 & 0 & 0.6352 & 0.046 & 0.015 \\ 0 & 0.6356 & 0 & 0.6491 & 0 \\ 0 & 0.046 & 0.6491 & 0 & 0.8678 \\ 0.011 & 0.015 & 0 & 0.8678 & 0 \end{bmatrix} \qquad (\,3\text{-}6\,)$$

with $R_1 = R_2 = 1.0113$. The value of the couplings between non-adjacent resonators are very small that can be ignored, which is vital for the optimization of the filters. Normally in microstrip filters, one important issue is how to minimize the parasitic couplings in order to achieve the prescribed response. However, here, because of the existence of the EBG cells, the parasitic couplings are negligible. The maximum measured insertion loss is 1.9 dB. Due to the radiation of input/output microstrip lines, a weak direct coupling between them is observed in the measured results. This coupling is below -40 dB and creates transmission zeros far away from the passband. The Optimized dimensions of the circuit are shown in Table 3-3.

Table 3-2. **Required rotations to convert the extracted CM of fifth order filter to the in-line configuration.**

Rotation number	Pivot [i, j]	$\theta_r = tan^{-1}(M_{u1,u2}/M_{v1v2})$			
		u1	u2	v1	v2
1	[4,2]	1	4	1	2
2	[3,2]	1	3	1	2
3	[3,4]	3	5	4	5
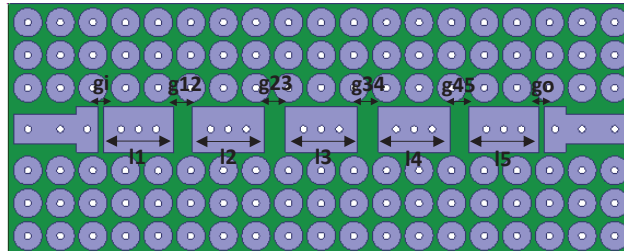
Figure 3-13. **Fifth order PRGW bandpass filter. The top plate and excitation lines are not shown.**

Table 3-3. **Optimized parameters of fifth order PRGW filter of Figure 3-13.**

Parameter	Value (mm)	Parameter	Value (mm)
l1=l5	3.6695	gi=go	0.2753
l2=l4	3.7351	g12=g45	0.979
l3	3.7364	g23=g34	1.1055

Layer 1   Layer 2   Layer 3

Device assembled in 1.85mm connectors
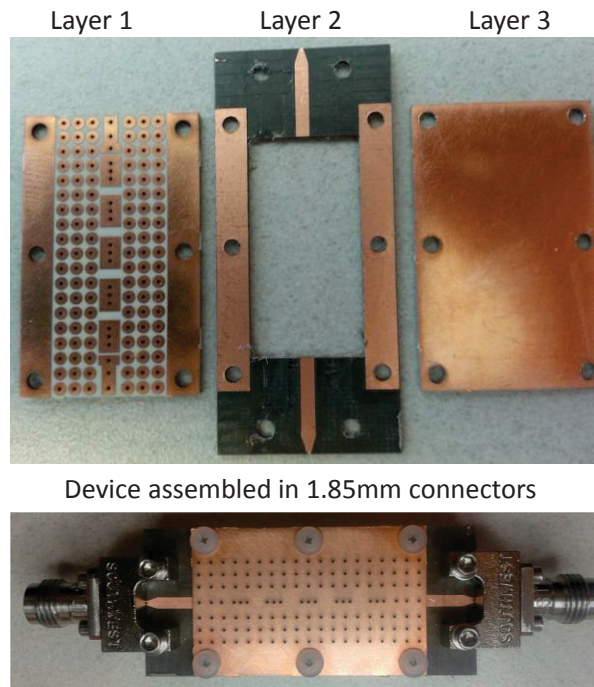
Figure 3-14.   Fabricated fifth order PRGW bandpass filter.
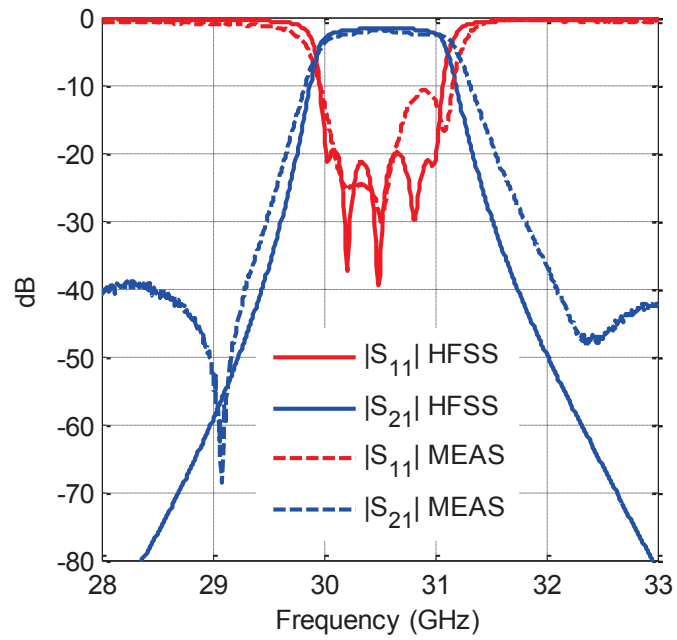
Figure 3-15.   Simulated and measured results for fifth order PRGW filter.

3.5. Triplet Sections

To achieve better selectivity, triplet sections were designed that can provide one finite transmission zero either on the lower or upper side of the passband. Figure 3-16(a) shows a third order filter with all half-wavelength resonators that can provide a bandpass filter with one transmission zero on the upper side of the passband. The second circuit (Figure 3-16(b)) uses a λ transmission line for resonator number 2 to realize a transmission zero on the lower side of the passband. In these examples, the width of the resonators is set to $\omega_0/2$=1.2 mm compared to the in-line cases to have enough separation of the orthogonal resonant modes from the passband. This does not create any significant change in the insertion loss. The simulated responses for both triplet filters are shown in Figure 3-17. The minimum simulated insertion loss is 0.85 dB for both cases. The extracted CM of the first triplet is:

$$M = \begin{bmatrix} 0.1217 & -0.8775 & 0.5363 \\ -0.8775 & -0.5158 & -1.0958 \\ 0.5363 & -1.0958 & 0.1229 \end{bmatrix}$$

(3-7)

with $R_1 = R_2 = 1.2202$.

(a)   (b)
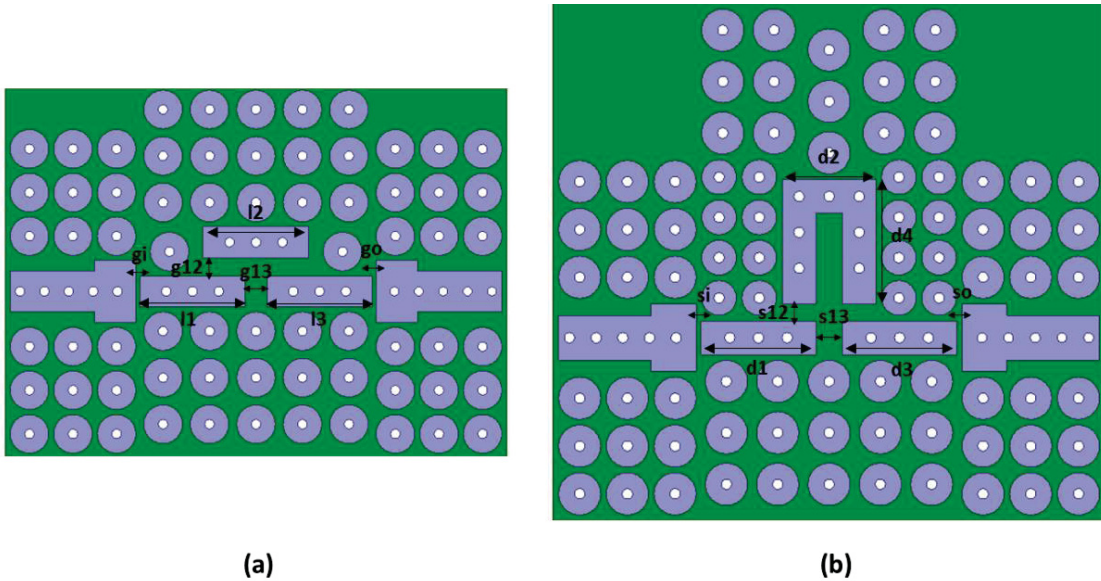
Figure 3-16. Triplet sections in PRGW technology.

(a)   (b)
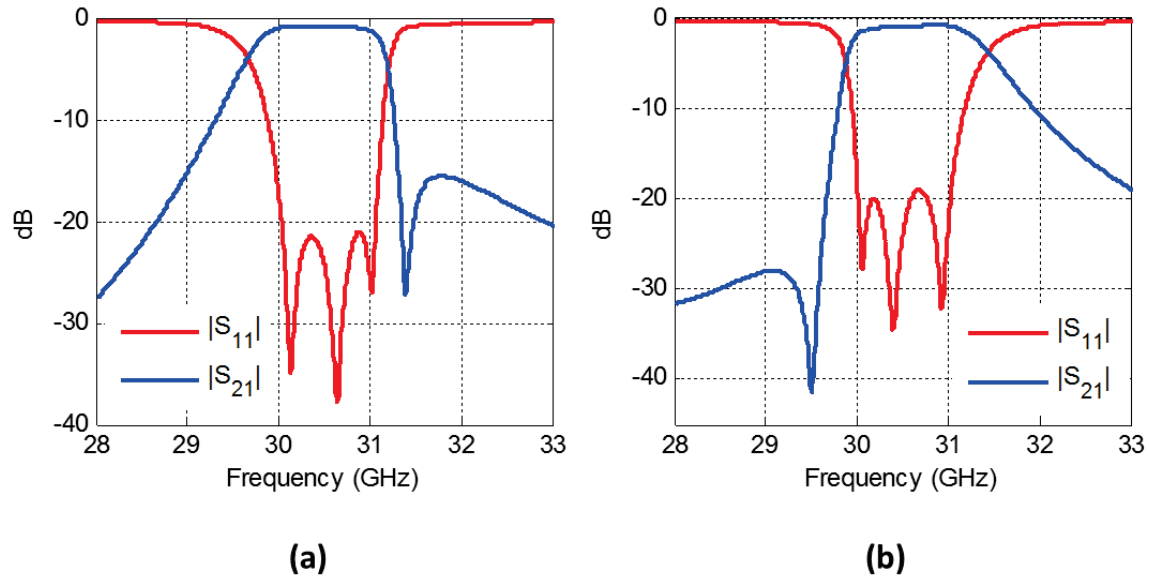
Figure 3-17.   Simulated response for triplet filter in a) Figure 3-16(a), b) Figure 3-16(b).

For the second triplet with TZ on the lower side of the passband, the extracted CM is:

$$M = \begin{bmatrix} -0.1217 & 0.8575 & 0.5363 \\ 0.8575 & 0.5181 & -1.0958 \\ 0.5363 & -1.0958 & -0.1229 \end{bmatrix} \qquad (\,3\text{-}8\,)$$

with $R_1=R_2=1.2202$. The photos of the fabricated components of the filter are shown in Figure 3-18. The measured results are plotted in Figure 3-19. For these circuits, considerable frequency shift exists, which is caused by the over-sized vias on the lines. Normally, the over-sized holes exist due to the use of the laser-driller in the PCB circuits. For the designed filters in the previous section, this effect was compensated before fabrications. Therefore, the frequency shift in the measurements is negligible. By simulating the designs with larger via diameter (4 mils bigger), very close response is achieved, which is shown in Figure 3-19. For the second trisection filter (Figure 3-16(b)), some of the unit cells around the λ resonator had to be smaller to fit in the restricted space. With the bigger via size, their bandgap is shifted to a higher frequency and therefore some spikes are present in both measured and simulated S-parameters below 30 GHz. The minimum measured insertion loss is 1 dB for both circuits. The optimized dimensions of

these circuits are shown in Table 3-4. It is worth mentioning that even though no EBG mushroom cell exists between the different arms of the λ-resonator in the second trisection, no coupling is present between them. This comes from the symmetry of the circuit that creates identical fields on both sides of the resonators that cancel any coupling.

Similar to the previous circuits, using a TRL calibration kit, the effect of the connectors and the loss of microstrip transitions were removed in the measured results.

Table 3-4. **Optimized parameters of triplets PRGW filters in Figure 3-16.**

Parameter	Value (mm)	Parameter	Value (mm)
11=13	4.0983	d1=d3	4.087
12	4.1246	d2	3.3447
13	3.7364	d4	4.4309
gi=go	0.1593	si=so	0.1768
g12	0.7139	s12	0.5925
g13	0.8529	s13	0.9447
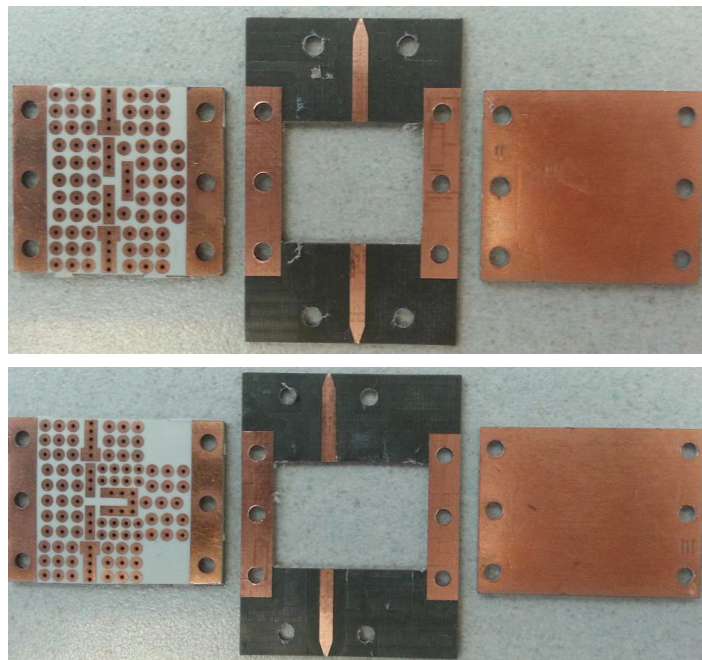
Figure 3-18. **Fabricated PRGW triplet filters.**
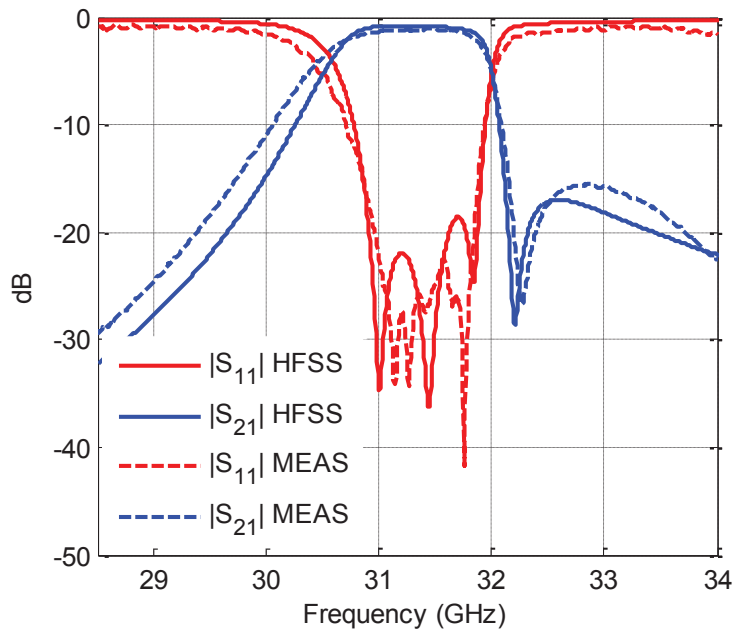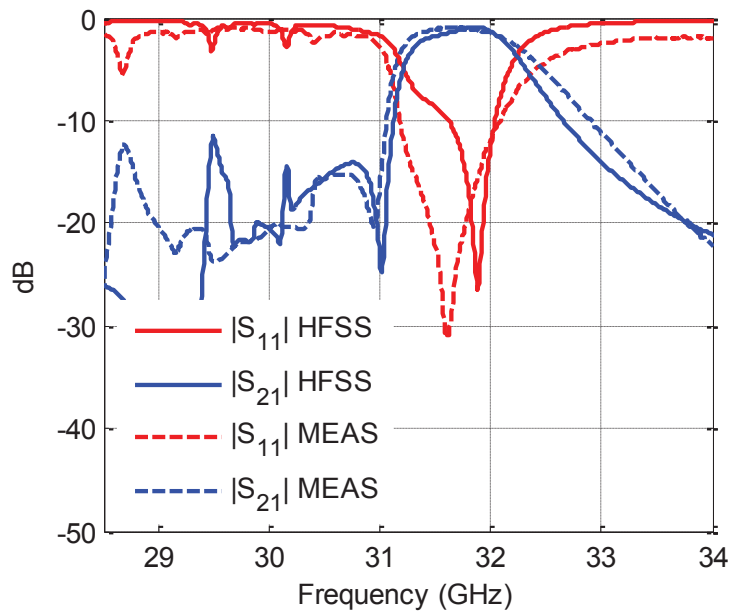
Figure 3-19.   Measured response compared to simulation considering the oversized vias for a) trisection 1, b) trisection 2.

3.6. Quadruplet Section

As the final example, we designed a quadruplet filter with a symmetric response. The coupling diagram of the filter is shown in Figure 3-20(a). In order to have a symmetric response with one TZ on each side of the passband, M_{14} should be positive. Otherwise, the response of the filter shows two TZs on the upper side of the passband. The geometry of the design is illustrated in Figure 3-20(b). Resonators number 1 to 3 are half-wavelength lines that are inter-coupled to each other. Resonator number 4 is a wavelength long to achieve the positive coupling of M_{14}. As a design strategy, one arm of the resonator number 4 (*l6*) is kept constant, and by optimizing the other arm (*l4*), the resonator is tuned to the correct frequency. Therefore, we have to use a slant shape, which doesn't have any effect on the performance. During the optimization of the circuit, the period of the unit cells in the middle degraded significantly, therefore it affects the ability of the mushroom unit cells to suppress the coupling between non-adjacent resonators. Consequently, the parasitic couplings of M_{13} and M_{24}, which ideally should be zero, are affected. The goal CM for this design is:

$$M = \begin{bmatrix} 0 & -0.8098 & 0 & 0.3525 \\ -0.8098 & 0 & -0.8348 & 0 \\ 0 & -0.8348 & 0 & -0.8098 \\ 0.3525 & 0 & -0.8098 & 0 \end{bmatrix} \tag{3-9}$$

with $R_1 = R_2 = 1.0295$. The extracted CM from the simulated S-parameters is:

$$M = \begin{bmatrix} 0.0083 & -0.8120 & -0.1514 & 0.3334 \\ -0.8120 & 0.0466 & -0.8164 & -0.1537 \\ -0.1514 & -0.8164 & -0.0032 & -0.8508 \\ 0.3334 & -0.1537 & -0.8508 & 0.0276 \end{bmatrix} \tag{3-10}$$

which shows the presence of considerable parasitic couplings. The simulated and extracted S-parameters are plotted in Figure 3-21. A single rotation can be derived to reduce the extracted CM from simulated S-parameters for the quadruplet filter geometry shown in Figure 3-20(a). By assuming the unknown angle θ, the rotation matrix for a [2, 3] pivot is:

$$R = \begin{bmatrix} 1 & 0 & 0 & 0 \\ 0 & \cos\theta & -\sin\theta & 0 \\ 0 & \sin\theta & \cos\theta & 0 \\ 0 & 0 & 0 & 1 \end{bmatrix}$$

(3-11)

The reduced CM is calculated by:

$$M' = R.M.R^t$$

(3-12)
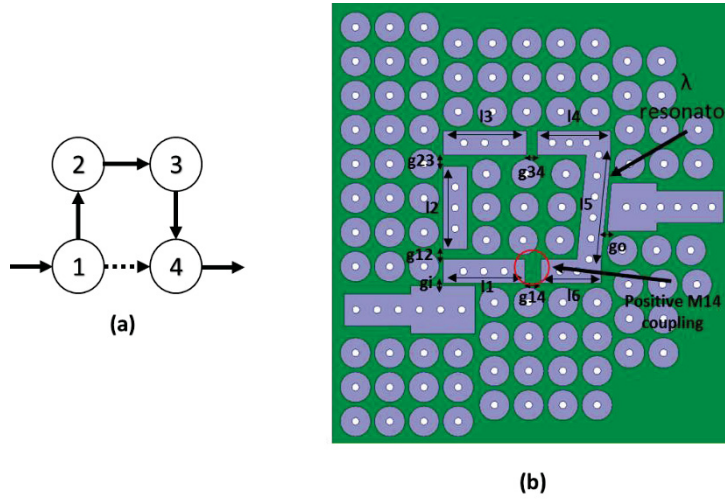
Figure 3-20. PRGW quadruplet filter a) coupling diagram, b) geometry.

where M is the full extracted CM from the simulated S-parameters using the method in [26], and R^t is the transpose of R. After applying the rotation, the elements that are supposed to be annihilated, in terms of the original CM, become:

$$M'_{13} = M_{13} \cos\theta + M_{12} \sin\theta$$

(3-13)

$$M'_{24} = M_{24} \cos\theta - M_{34} \sin\theta$$

By forcing M'_{13} and M'_{24} to zero simultaneously:

$$\frac{M_{13}}{M_{34}} = -\frac{M_{12}}{M_{24}} \tan^2\theta$$

(3-14)

46

which leads to:

$$\theta_r = \tan^{-1}\sqrt{-\frac{M_{24}M_{13}}{M_{12}M_{34}}}.$$

(3-15)

That gives the rotation angle.
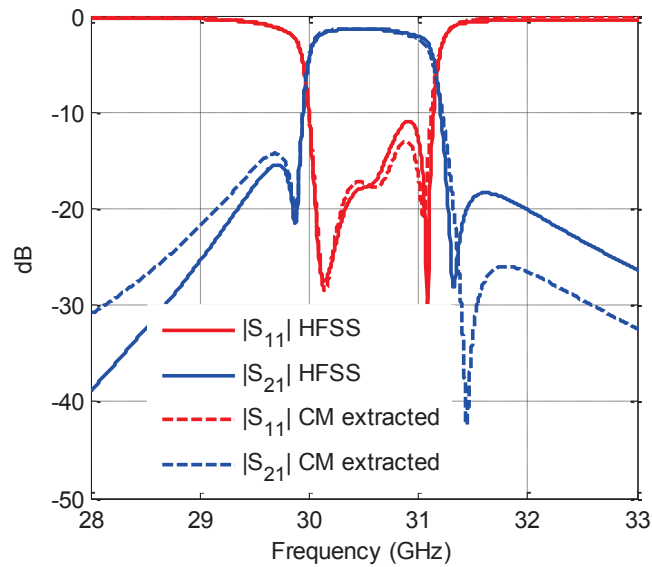
Figure 3-21.   Simulated and extracted S-parameters for PRGW quadruplet filter.
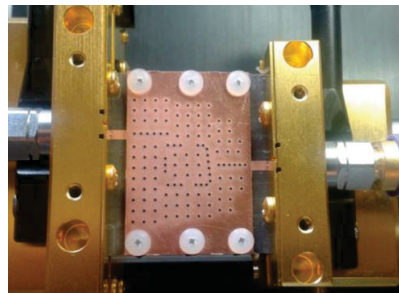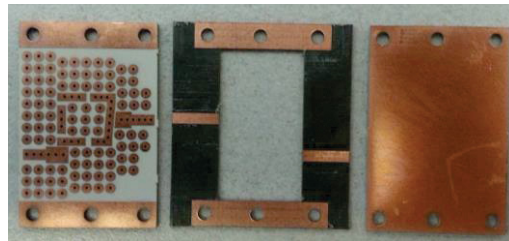
The device assembled in test fixture

Figure 3-22.   Fabricated PRGW quadruplet filter and the measurement setup.

By considering the approximate values of M_{13} and M_{24}, a new CM has been designed to achieve better reflection. However, this would cause some asymmetry in the response. The fabricated circuits and measurement setup are shown in Figure 3-22. The final optimized response is provided in Figure 3-23 along with the measured results. The measurement for this circuit was carried out using a universal test fixture, which caused some discrepancy due to limitations of the test fixture in this frequency band. The measured insertion loss is 2.5 dB. By using a better configuration to ensure isolation between resonators number 1 and 3 and also between resonators number 2 and 4, a better response can be achieved.
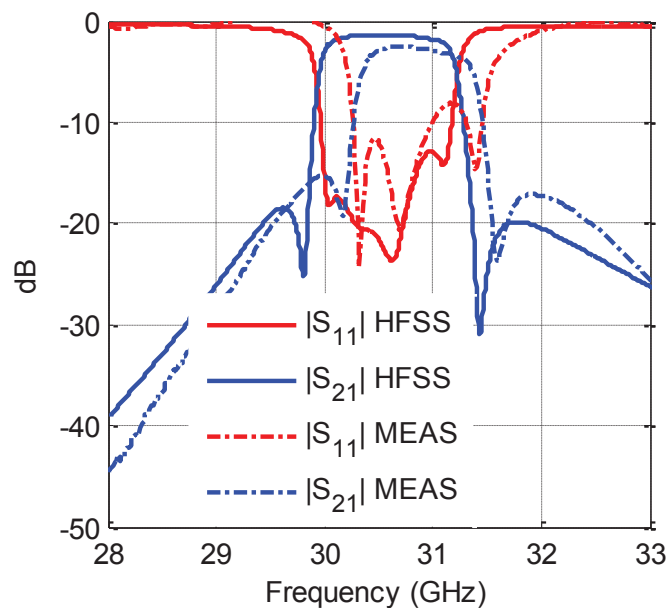
Figure 3-23.   Simulated and measured S-parameters for PRGW quadruplet filter.

Table 3-5.   Optimized parameters of quadruplet PRGW filter of Figure 3-20.

Parameter	Value (mm)	Parameter	Value (mm)
l1	4.0474	gi	0.1087
l2	4.1258	go	0.1705
l3	4.1381	g12	0.4962
l4	3.6378	g23	0.5679
l5	5.2114	g34	0.5486
l6	3	g14	0.8047

3.7. Fabrication and Measurement

All the circuits have been fabricated using the conventional PCB technique. The fabricated models consist of three layers. (1) The PRGW section, which has the resonators, and mushroom cells and contains plated vias, (2) microstrip excitation lines, which also maintain the required air-gap for the circuits, and (3) a metallic top plate that is realized using a substrate having a conductor on one side. The three layers connected to each other using some plastic screws. No adhesive is used, and contact between the ground plane of the microstrip excitation line and the top plate of PRGW is insured by pressure caused by tightening the screws. It should be noted that the microstrip excitation lines are not an integral part of the design, and we are using them in order to acquire the ability to measure the circuits. In a complete system implemented in PRGW technology, these lines are not present, and we expect better performance regarding the insertion loss. Also, the top plate does not have any texture and can be realized by any conductive surface or the low-cost FR4 substrates. Therefore, the main part of PRGW circuit is realized only in a single layer that contains all the cells, vias, and the ridge. During the measurement, an in-house TRL calibration kit is designed and used to move the reference planes away from the connectors and fixture probes and shift it to the beginning of PRGW line as shown in Figure 3-12. However, we still measure a portion of the microstrip lines that is packaged between the mushrooms and the top plate, which has a certain amount of dielectric loss and a small amount of leakage since it is already packaged. Overall, the measurements and simulations agree very well considering that all the circuits are hand-assembled, and they are the first prototype in this technology. In some circuits, considerable frequency shift exists, which comes from the over-sized via holes on the lines. Based on our analyses, the accuracy of via diameter is a major factor, and the oversize diameters should be compensated before fabrication as they act as inductances that vary with their diameters and consequently change the resonant frequency of the lines.

3.8. Comparison to Microstrip Filters

To compare the performance of the proposed technology to microstrip, several cases have been investigated by designing the same filter function in MS technology and

studying different packaging options for it. Initially, third order all-pole microstrip edge-coupled filter has been developed on an RO6010 substrate with ε_r = 10.2 and tan δ = 0.0023. We chose a thinner substrate with higher permittivity in order to have a fair comparison. If we have used the same material as in PRGW circuits, as it is a thick board with low permittivity, it would have increased the radiation loss. Also, we used the edge-coupled configuration to have a practical MS filter. The end-coupled microstrip filter with the required BW of 3.3%, will end up with very small and unrealizable gap dimensions. The performance of the circuit is compared to the third order PRGW filter designed in Section 3.4 (Figure 3-9) for three different scenarios. In the first scenario, the microstrip filter is enclosed in a metallic box. Later on, we designed an artificial magnetic conductor packaging surface and replaced the metallic enclosure with it. The AMC packaging for microwave circuits was proposed and studied in [27], [28] and in brief, it uses the periodic EBG structure to package the microstrip circuits instead of using PEC packaging. Here, we used a PCB periodic bed of mushrooms to package the predesigned microstrip filter.
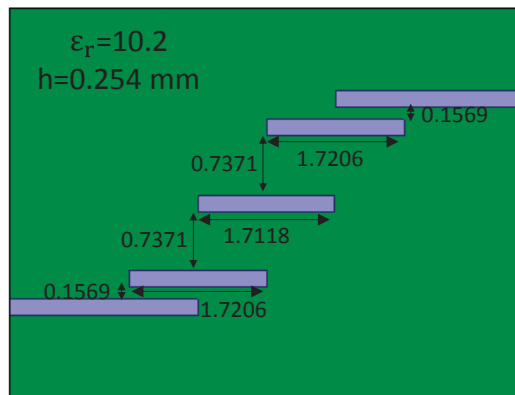
Figure 3-24. Edge-coupled microstrip filter. The dimensions are in mm.

(a)　　　　　　　　　　　　　　　　**(b)**
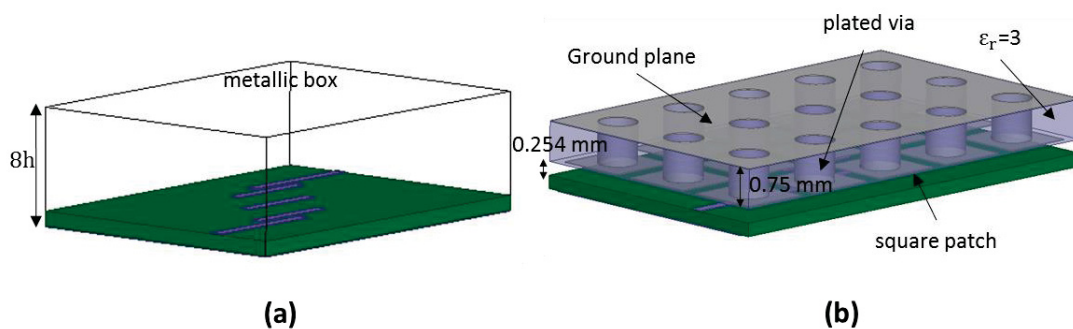
Figure 3-25. Third order edge-coupled bandpass filter with different packaging options: a) metallic packaging, b) AMC packaging.

The microstrip filter dimensions are shown in Figure 3-24. Figure 3-25(a) illustrates the filter in a metallic cavity package. Figure 3-25(b) demonstrates the filter in a cavity packaging with AMC cavity cover. The height of the metallic box is set to 8h as the standard procedure [24] to minimize the interaction with the filter. Finally, the microstrip filter without any packaging is included in the comparison. Figure 3-26 shows S$_{21}$ for all these cases over a wide frequency range of 10-50 GHz. In Figure 3-27, detailed performance of the filter in the passband is shown. PRGW filter has the lowest insertion loss (almost half of PEC packaged MS filter). AMC packaged filter shows more insertion loss compared to PEC packaged one. As expected, MS filter without any packaging has the worst performance to a level that it loses its functionality. It is important to discuss the rejection bandwidth of these filters too. As mentioned in Section 3.4, PRGW filters can only maintain the rejection in the bandgap of the cells. Figure 3-26 shows that the PRGW filter maintains the rejection between 25-38 GHz. At frequencies lower than 25 GHz, spikes appear which come from the resonant modes of the mushroom cells. At the 38 GHz, the orthogonal mode of the resonators is excited which can be put away by using a narrower line. In the case of the microstrip filter, the main factor that deteriorates the rejection of the filter is the resonant modes of the packaging box. Here, we tried to put them as far as possible by using the smallest possible box that doesn't interfere with the circuit itself. The first resonant mode of the box appears at 34.4 GHz. For AMC packaged filter, some spurious modes are excited at the lower side of the passband due to limitations of the stopband of the designed AMC surface. In order to extend the rejection bandwidth of PRGW filters, several methods can be applied. Adding extra plated vias on the resonators can increase the operating frequency band of the structure by making it as wide as the EBG cell without the ridge (Figure 3-1). Also, using narrower lines has the similar effect in addition to moving the orthogonal resonant mode further. Also, by having smaller air-gap dimension, the band-gap of the unit-cell increases [5]. Another technique that found to increase the operating frequency band of PRGW and consequently improves the rejection bandwidth of the filter is by separating the mushrooms surface from the waveguide bottom surface, which will be presented in the next chapter. This separation provides wider frequency band. Also, the design process is facilitated as there is no need to arrange the mushroom cells around the resonators and guiding lines as they stay unchanged in the bottom layer during the design procedure. Such a design requires an additional dielectric substrate that must be thin, which has other fabrication difficulties and

cost. Moreover, it will result in a lower quality factor of the line due to the additional dielectric loss of the substrate.
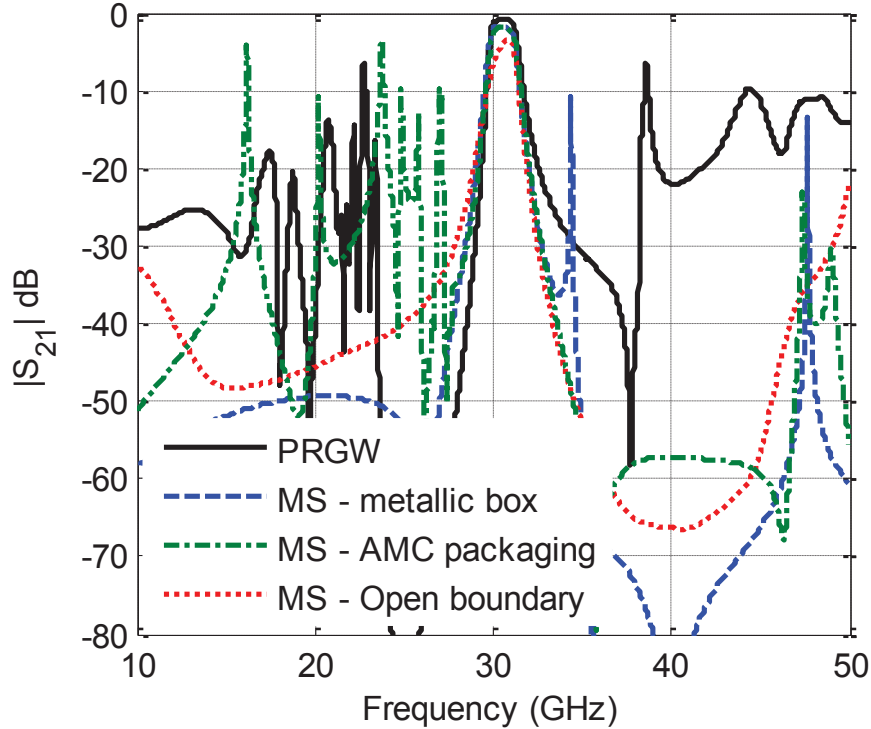
Figure 3-26.   Simulated S$_{12}$ for third order PRGW filter and MS filter with different packaging options.

The performance of these filters has been compared to narrow band designs. Therefore, the same filters have been developed at 30.5 GHz with 330 MHz bandwidth (1%) on PRGW and MS. The performance of the designed filters regarding the insertion loss is compared in Figure 3-28. As expected, PRGW filter has the superior performance compared to PEC packaged and open MS filter in terms of the insertion loss.

As the last comparison, the quadruplet filter presented in Section 3.6 is compared with its similar design in MS technology. The MS filter is shown in Figure 3-29 along with the dimensions in Table 3-6. For this circuit, RO3203 with thickness h=0.254 mm is used, which has a lower permittivity (ε_r=3.02) and also lower loss tangent ($tan\delta$=0.0016). The design is similar to its PRGW equivalent with some minor differences. Generally, in MS technology couplings are weaker. Therefore, the gaps are much smaller. For the output coupling, we used the long parallel line to provide the necessary coupling. The

performance is compared to different cases in Figure 3-30. As expected, PRGW has the best loss performance but suffers from low rejection bandwidth. However, the MS filter packaged in the metal box shows many spurious spikes, which comes from the modes of the box itself. For this specific design, it was a challenging act to arrange the box size to avoid having any resonant mode in the passband and at the same time, for the box to have the minimum influence on the filter. Here, we had to have the passband of the filter between TE_{101} and TE_{102} resonant mode. For the MS filter without any packaging, the loss has increased to an unacceptable value.
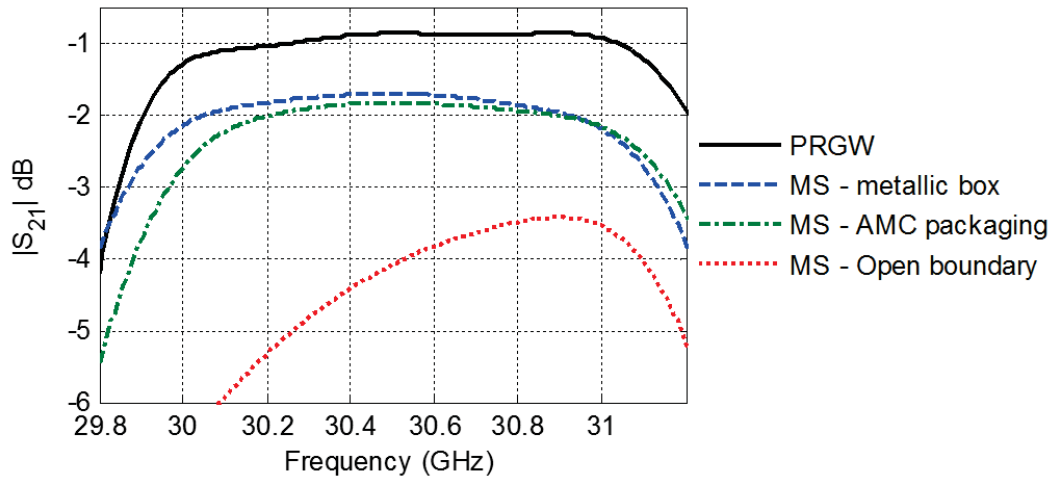
Figure 3-27. **Simulated S_{21} for third order PRGW filter and MS filter with different packaging options**

The quality factors of the resonators in various cases can be calculated using the imaginary part of the extracted CM for each case. The effective unloaded quality factor for the ith resonator of a filter can be found by [26]:

$$Q_u(i) = \frac{f_0}{BW} \cdot \frac{1}{\sigma(i)} \qquad (3\text{-}16)$$

where f_0 is the center frequency, and BW is the bandwidth of the filter, and $\sigma(i)$ is the imaginary part of the ith diagonal element of the CM. The imaginary part of the CM can be extracted using the same procedure in [26]. By calculating the Q-factor for the resonators other than the ones in the input/output, the loss of the feeding network and transitions can be excluded. Table 3-7 shows the Q-factors for the different cases, such as half-

wavelength wide PRGW (used in all-pole filters in Section 3.4), narrow half-wavelength and wavelength PRGW (used in triplet and quadruplet filters in Section 3.5 and 3.6), and MS with different packaging options for two different substrates. As it can be seen, PRGW resonator has significantly higher Q-factor compared to all other cases. Although MS filters are smaller and cheaper compared to PRGW, they are not practical in the millimeter wave band as shown above. A functioning MS filter should be accompanied by a metallic packaging box, which makes the total size, price, and weight of the structure considerably bigger compared to PRGW.
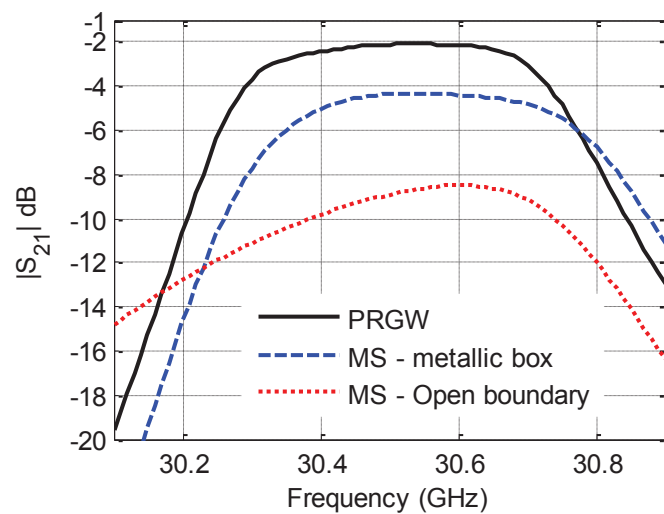
Figure 3-28. **Simulated S_{21} for third order PRGW filter and MS filter (BW=1%) with different packaging options.**
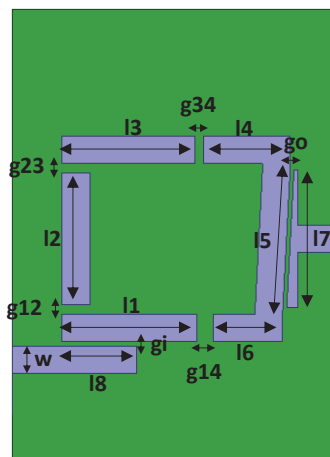
Figure 3-29. **Quadruplet bandpass filter in microstrip technology.**

Table 3-6.   Parameters of quadruplet MS Filter of Figure 3-29.

Parameter	Value (mm)	Parameter	Value (mm)
l1	2.8999	l8	1.6
l2	2.8586	gi	0.0936
l3	2.8527	go	0.92
l4	1.8778	g12	0.1984
l5	3.2677	g23	0.2062
l6	1.5	g34	0.196
l7	2.8911	g14	0.3553
w	0.5954		

3.9. Conclusion

New technology has been introduced for designing TEM printed gap-coupled bandpass filters in millimeter-wave band. Several design examples have been presented that show excellent insertion loss performance compared to microstrip filters. The designs are based on ridge gap waveguide, which is a quasi-TEM propagation medium realized by a printed parallel-plate waveguide surrounded by a bed of mushrooms. The propagation medium is air; therefore, the effect of dissipation is largely removed from the circuit's performance. In addition, the circuits are self-packaged and do not need a metallic enclosure. No electrical contact is required in the designs. Measured results show good agreement with the simulations. Due to the inherent resemblance of PRGW to the microstrip line, many existing structures that are based on microstrip lines technology in the past decades can be implemented using PRGW technology to benefit from low loss properties and still maintaining low-cost fabrication and dispersion-less propagation characteristics. Also, the proposed technology is self-packaged and is much thinner compared to microstrip technology after packaging.
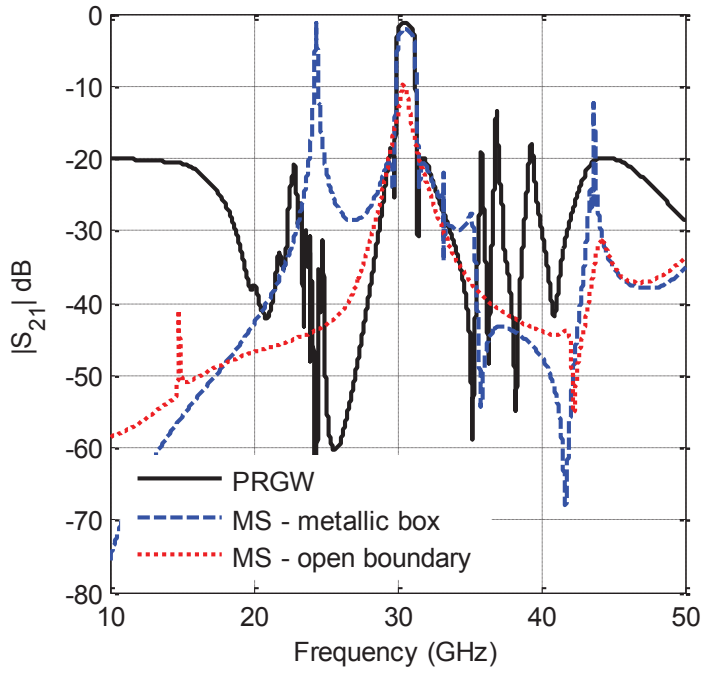
(a)
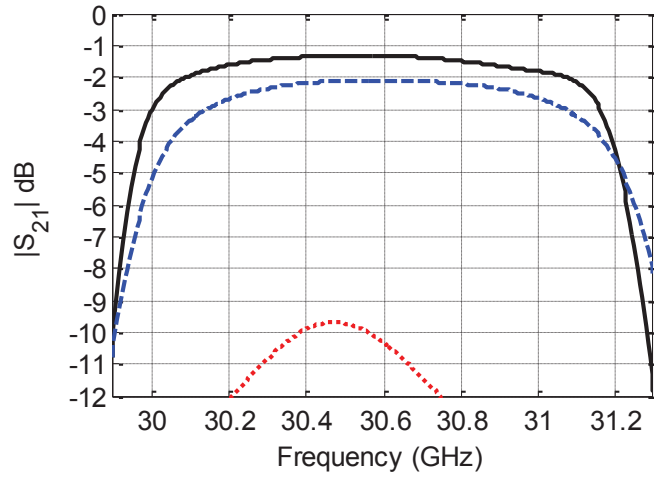
(b)

Figure 3-30. Simulated S_{21} for quadruplet PRGW filter and MS filter with different packaging options. a) wide-band performance, b) response in the passband.

Table 3-7. **Extracted unloaded quality factor of PRGW resonator and MS resonator with different packaging options.**

Structure	σ	Q_u
PRGW - Wide λ/2 resonator	0.0461	662
PRGW – Narrow λ/2 resonator	0.0502	608
PRGW – Narrow λ resonator	0.0851	358
MS λ/2 - PEC packaged (RO6010)	0.1257	243
MS λ/2 - PEC packaged (RO3203)	0.1109	275
MS λ/2 - AMC packaged (RO6010)	0.1310	233
MS λ/2 – Open (RO6010)	0.3752	81

Chapter 4.

New Printed Ridge Gap Waveguide with Facilitated Design Properties

4.1. Introduction

Printed ridge gap waveguide (PRGW) was introduced in [23] as a low-loss planar guiding structure for millimeter-wave band applications. Using PRGW, a new class of planar filters has been introduced in the previous chapter, which shows promising low loss behavior at 30 GHz bands. The proposed filters do not need a metallic packaging box as in MS filters. Therefore, they are smaller and lighter. The unloaded quality factor and loss performance of these filters are incomparably better than MS filters.

On the other hand, PRGW filters suffer from small rejection bandwidth as illustrated in Section 3.8 due to the limited electromagnetic bandgap of mushroom cells when combined with the ridge. As a matter of fact, the EBG cell that was used in Chapter 3 has a relatively wide forbidden band with an approximate ratio of 1:2. However, when emerged in the semi-periodic environment of PRGW, the usable frequency band is limited. Another drawback of these filters is the complexity of the design regarding the arrangement of the mushroom cells around the resonators and lines. It is a challenging and tedious process to place the periodic mushroom cells in the circuit in a way that the periodic texture does not lose the homogeneity and can isolate the different parts of the structure.

In this chapter, we are addressing these issues by separating the layers in which the mushroom cells and the ridge are printed. It is shown here that this configuration results in a guiding structure with a relatively wider bandwidth that improves the rejection bandwidth of the filter. By having the cells on a different layer, the design process is facilitated because the mushroom cells are not coinciding with the lines and resonators. Therefore, the structure has better flexibility, and more complicated circuits can be designed easily. Also, the low-loss characteristics of PRGW that was shown in Chapter 3 are preserved. A line with two 90 degree bends, a quadruplet bandpass filter, and a 4×4

antenna array are designed, fabricated and measured in to prove the concept that shows major improvement.
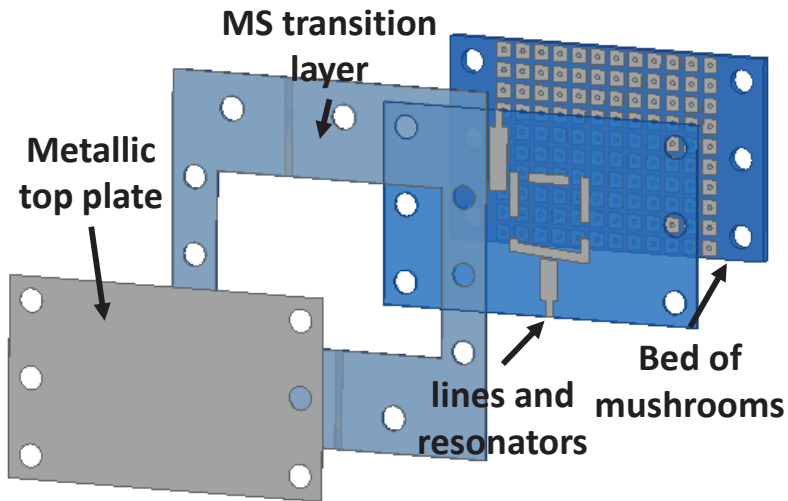
Figure 4-1.   Geometry of quadruplet filtering section using versatile PRGW.

4.2. Geometry of Versatile PRGW

The structure of the proposed PRGW filter is shown in Figure 4-1 in different layers. The first layer is composed of conductor plated vias topped by square patches, which is called a bed of mushrooms. This layer acts as artificial magnetic conductor (AMC). On the second layer, resonators, and lines (ridge) are printed. Therefore, it is very similar to an MS circuit with one major difference; there is no metallic ground plane in this layer, but rather an AMC on the lower layer. The third layer has dual purposes. The MS transition lines are printed on this layer from the input and output sides till they reach the circuit and beyond that, it acts as a spacer by removing the remaining dielectric substrate to maintain the required air-gap. The MS transition is designed based on the transition for regular PRGW that was used in Chapter 3, with some modification. Similarly, the basic idea is to have a 50Ω line in both microstrip and PRGW environment to preserve a good matching in the whole band. It is important to note that the third layer is merely for measurement purposes. The RGW is not a standard technology to be connected to a standard fixture probe. Therefore, it is necessary to use some kind of transition. Finally, a metallic top plate is placed that can be realized by a conducting surface or a low-cost FR4 substrate on one side of the conducting surfaces is only needed in this case.

It can be seen that the presented PRGW is very close to the original PRGW in Chapter 3. The main difference is that the EBG cells and ridges are separated by different layers which has many benefits as described in the introduction, without adding much complication and cost. It is important to note that the propagating mode exists in the air-gap between the second layer and the top plate. Therefore, the dielectric loss of the substrates is avoided to a great extent.
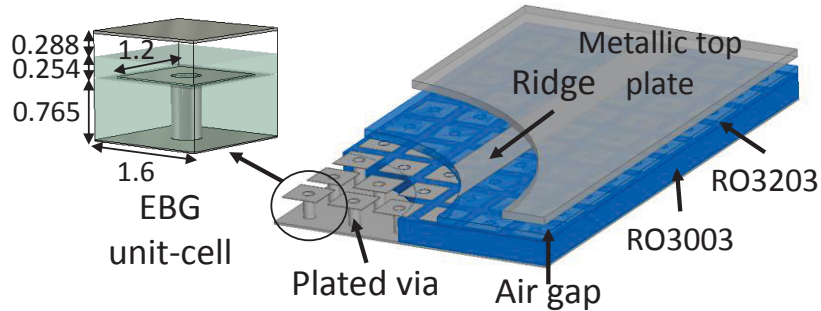
Figure 4-2. **Geometry of printed ridge gap waveguide using two separate substrates for ridge and EBG cells. The geometry of a single EBG mushroom cell is shown. Dimensions are in mm.**
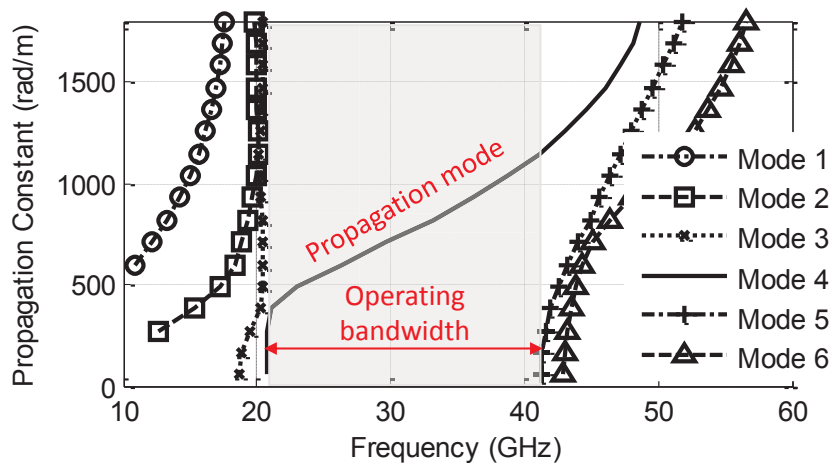
Figure 4-3. **Dispersion diagram of the proposed printed ridge gap waveguide.**

4.3. Dispersion Diagrams and Operating Frequency Band of the Structure

The unit cell of the bed of mushrooms and the complete waveguide section are shown in Figure 4-2. The gap between the square patch and the metallic top plate consists
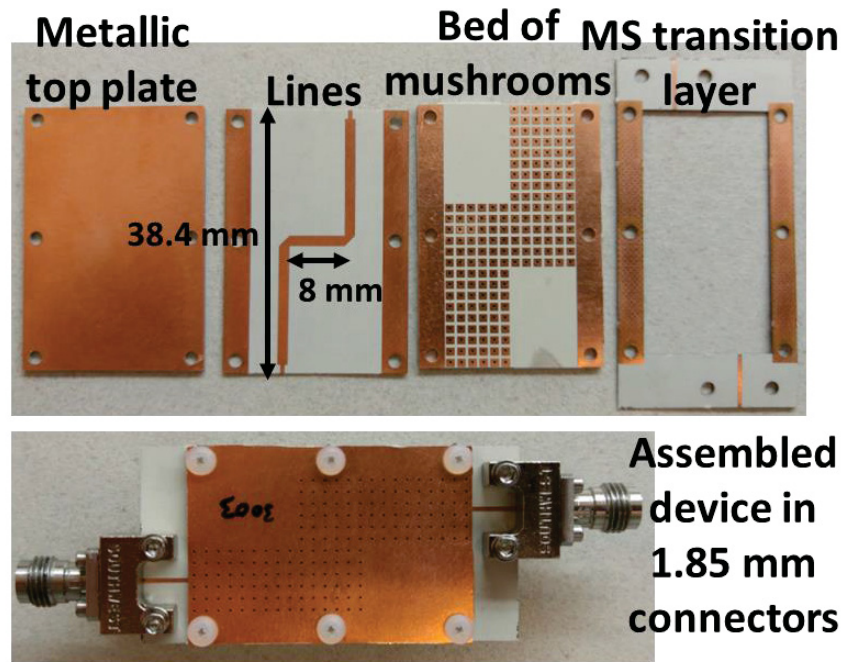
Figure 4-4. Fabricated parts and assembled circuit for a line with two 90 degree bends. The total length of the line is approximately 4.6λ at 30 GHz.

of two different materials. The top portion is air and bottom is made from a dielectric with ε_r=3.02. We designed the cell to have a band-gap in 20-40 GHz. Using the designed EBG cell, the complete geometry of the waveguide is constructed by printing the ridge over the dielectric material in the gap and arranging the cells in a semi-periodic configuration as shown in Figure 4-2. The dispersion diagram of the guide reveals that in the same bandgap of the EBG cell, a single mode is present, which shows a quasi-linear behaviour as shown in Figure 4-3. It can be shown that the operating bandwidth of the guide is almost as wide as the band gap of the EBG cell (unlike the regular PRGW that the guiding bandwidth is less than the EBG cell band). Therefore, much wider operating bandwidth can be achieved compared to the regular PRGW. This can improve the rejection bandwidth of the bandpass filters designed in this technology. To prove the concept, a line with two 90 degree bends is constructed and measured. The fabricated parts are shown in Figure 4-4. Different layers are connected using few plastic screws without any adhesive. The measured results compared to the simulation are shown in Figure 4-5. In order to preserve a good TRL calibration accuracy with a single delay line, the measurements are performed in the 25-35 GHz band that shows good agreement with the simulation. The measured insertion loss gets as low as 0.4 dB for the total line length of

4.6 λ at 30 GHz. Based on our analyses, displacement of the lines relative to the mushrooms does not have any adverse effect on the matching level.
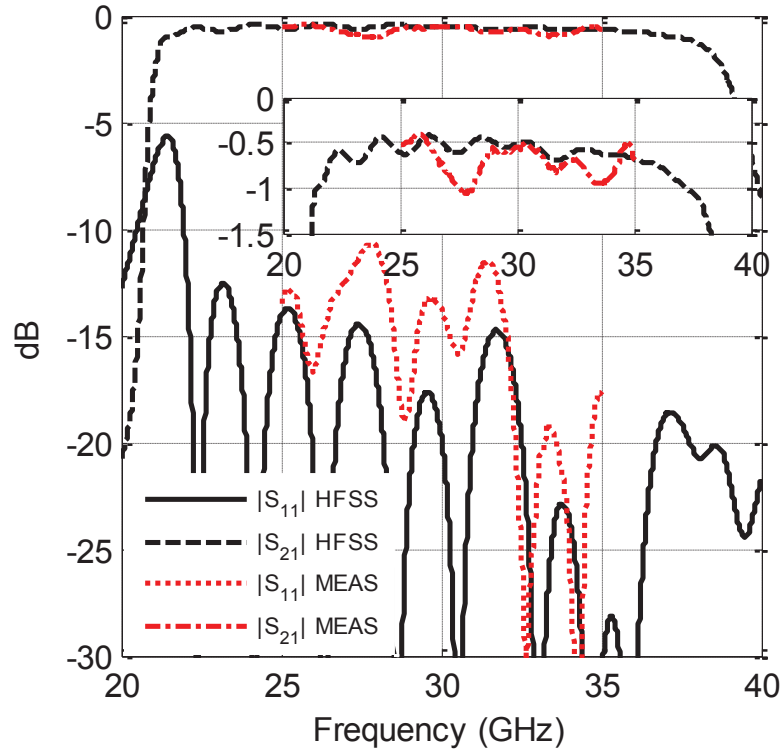
Figure 4-5. **Simulated and measured response of the circuit in Figure 4-4. TRL calibration removes the effect of the MS excitation lines.**

4.4. Design of Quadruplet Bandpass Filter

Using regular PRGW requires the careful arrangement of the mushroom cells between and around the resonators and the lines. In addition, during the optimization of the circuit, the period of the cells might be degraded significantly. This leads to a parasitic coupling between non-adjacent resonators, which is shown in the design of the quadruplet filter in PRGW technology in Section 3.6. Using the proposed configuration, the EBG cells are designed independently regardless of the resonators' position and are placed on the very bottom layer. During the optimization, this layer stays unchanged. Therefore, appropriate isolation between non-coupled resonators can be assured, which speeds the optimization process and also removes some constraints that use to be imposed to assure specified separation between the lines and the mushrooms. Figure 4-6(a) shows the

coupling diagram and the geometry of the middle layer where input/output lines and resonators are placed. In order to have a symmetric response with one transmission zero (TZ) on each side of the passband, the coupling between Resonator 4 and Resonator 1 (M_{14}) should be positive. Otherwise, the response of the filter shows two TZs on the upper side of the passband. Therefore, a λ transmission line is used for Resonator 4. The design is very similar to the quadruplet filter in Section 3.6. The main difference is the arrangement of the EBG cells and line that are now placed on two different layers. Optimization of the design is carried out by extracting the coupling matrix (CM) of the circuit from the simulated S-parameters and using a linear mapping to find the correct dimensions of coupling gaps and resonators' length to reach to the required CM in an iterative procedure. Similar to the previous designs, the method outlined in [26] is used to extract the CM analytically. The simulated response is calculated using Ansys HFSS, which is the response of the complete circuit as shown in Figure 4-1 including input/output microstrip excitation lines.

(a)   (b)
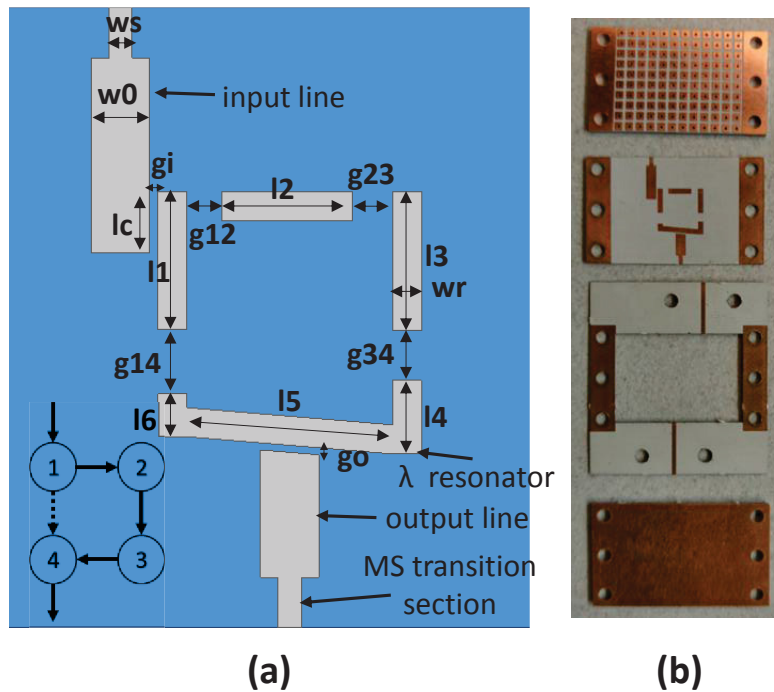
Figure 4-6. **a) Middle layer of the quadruplet bandpass filter configuration with the coupling diagram. b) Fabricated parts. Dimensions are as follow: l_1=3.5673, l_2=3.3773, l_3=3.5857, l_4=1.8919, l_5=5.3141, l_6=1.1, l_c=1.6, g_i=0.2106, g_{12}=0.8942, g_{23}=1.024, g_{34}=1.2968, g_{14}=1.6632, g_o=0.1029, w_s=0.5954, w_0=1.5, and w_r=0.75 all in millimeters.**
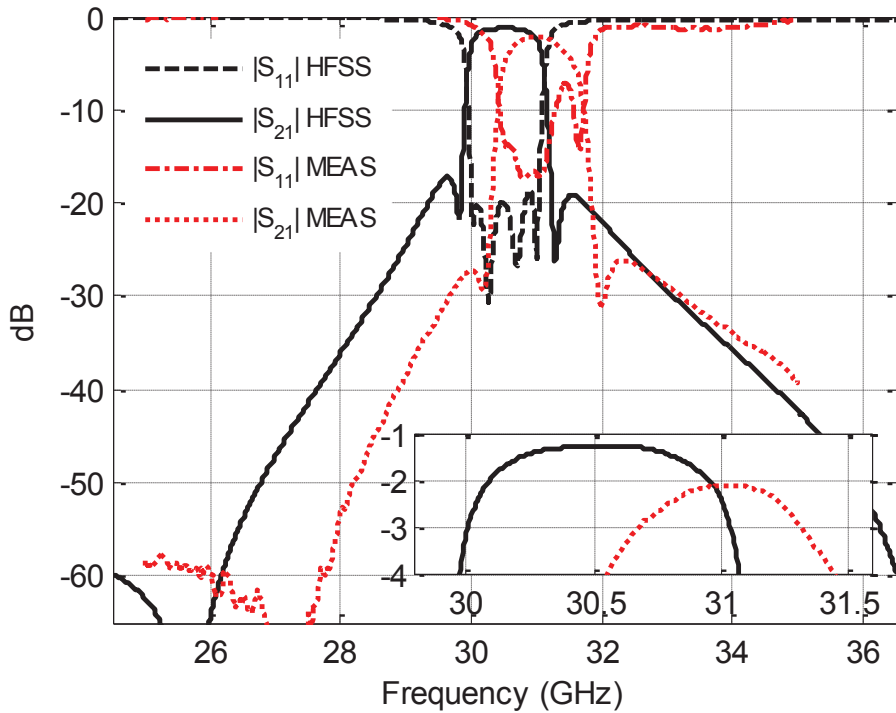
Figure 4-7.   Simulated and measured response of the quadruplet bandpass filter.

The optimized response of the filter is plotted in Figure 4-7 along with the measured results. Extracted CM of the optimized simulated response is calculated as:

$$M = \begin{bmatrix} -0.0880j & -0.7981 & -0.0830 & 0.3715 \\ -0.7981 & -0.0719j & -0.8378 & -0.0847 \\ -0.0830 & -0.8378 & -0.0771j & -0.8230 \\ 0.3715 & -0.0847 & -0.8230 & -0.0829j \end{bmatrix} \tag{4-1}$$

with $R_1 = R_2 = 1.0295$. Using the imaginary values of the diagonal, the unloaded quality factors of the resonators are calculated by (3-16). By calculating the Q-factor for the two resonators in the middle, the loss of the feeding network and transitions can be excluded. Therefore, the half-wavelength PRGW resonator has unloaded quality factor between 396 to 424, which is analogs to a narrow $\lambda/2$ resonator of regular PRGW, which Q-factor was extracted in Section 3.8 and listed in Table 3-7. As it can be seen, by using the new configuration proposed in this chapter, due to the additional loss of the extra dielectric layer, the Q-factor of $\lambda/2$ resonator decreased from 608 to around 420. The measured results in Figure 4-7 show an acceptable agreement with the analyses in general as a first

prototype trial. Some frequency shift and additional losses are observed in the measurements, which are due to the possible existence of additional air-gap between the layers. The additional air gap can be avoided by stacking the layers using adhesive and pressure as used in the conventional method of multi-layer structures. The minimum simulated and measured insertion loss of the filter are 1.2 and 2.3 dB, respectively.

4.5. Low-loss Bandstop Filters Based on PRGW

Bandstop (Notch) filters are a necessary component in communication systems when some particular interfering frequency need to be suppressed. In This section, required geometry to realize bandstop filters based on PRGW is developed. The improved realization of PRGW is chosen for this purpose since arranging the resonators with required spacing between them is troublesome in the classic PRGW due to the existence of the EBG cells. Later on, the performance of the designed filters will be compared to rectangular waveguide technology and microstrip.

4.5.1. General Design Method of Bandstop Filters

The classic design of bandstop filters are discussed in references such as [24], [25] using the definition of slope parameter and by designing each cavity resonator separately. Each slope parameter can completely define the characteristic of a cavity and the coupling to the main line. The circuit model in Figure 4-8 shows a bandstop filter with an arbitrary order. Initially, the required slope parameters can be calculated using Chebyshev coefficients for a filter with pre-defined bandwidth and order using the following equations:

$$\left(\frac{Z_u}{Z_0}\right)^2 = \frac{1}{g_0 g_{n+1}}$$

(4-2)

$$x_i = \omega_0 L_i = \frac{1}{\omega_0 C_i} = Z_0 \left(\frac{Z_u}{Z_0}\right)^2 \frac{g_0}{g_i FBW} \quad \textit{for i= 1 to n}$$

where g_i (i = 1 to n) are the Chebyshev coefficients of order n, Z_0 and Z_u are the impedance of the input/output lines and the lines between the resonators, C_i and L_i are the capacitance and inductance values of the circuit model and *FBW* is the fractional bandwidth of the filter. Later, by using full-wave analyses, each cavity resonator and its coupling to the main line can be designed based on its slope parameter using the following equation:

$$\frac{x}{Z_0} = \frac{f_0}{2\Delta f_{3dB}}$$

(4-3)
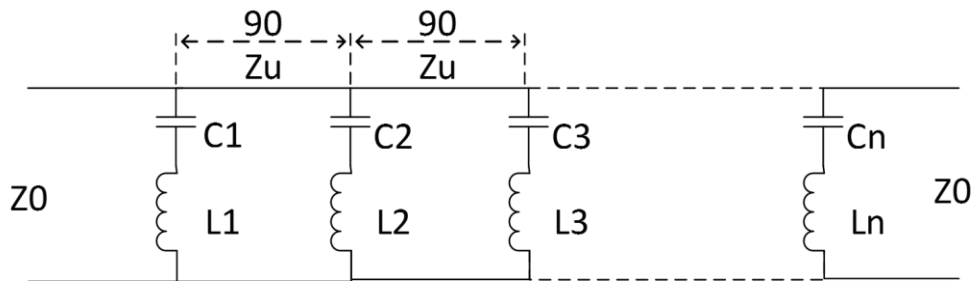
Figure 4-8.   The equivalent circuit of an nth order classic bandstop filter.

In many structures, the resonators are placed at the distance of $\lambda_g/4$ from each other. However, this causes strong interaction between them that affects the rejection level severely. Therefore, in many cases, it is obligatory to maintain a distance of $3\lambda_g/4$ between the cavities. This decreases the matching level of the passband of the filter due to the increased phase error of the lines. By increasing the number of the resonators and consequently, the order of the filter, keeping an acceptable matching level in the passband of the filter becomes more difficult. This problem gets more severe for the cases that the passband is relatively large. To overcome this issue, quarter wavelength sections with appropriate impedances can be placed between the resonators to achieve the required matching level. This was done on microstrip line in [25]. Some closed-form formulas have been presented to calculate the impedance of the transformer lines for a limited number of the cases up to a third order filter. Circuit model of such a representation of bandstop filter is shown in Figure 4-9.
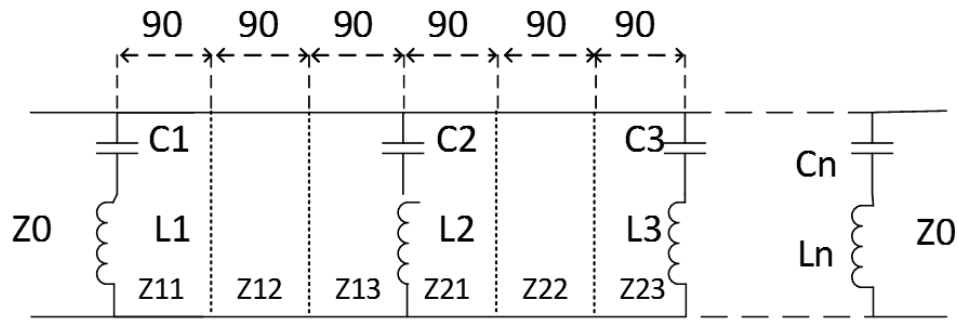
Figure 4-9. Circuit model a bandstop filter with non-uniform waveguide sections.
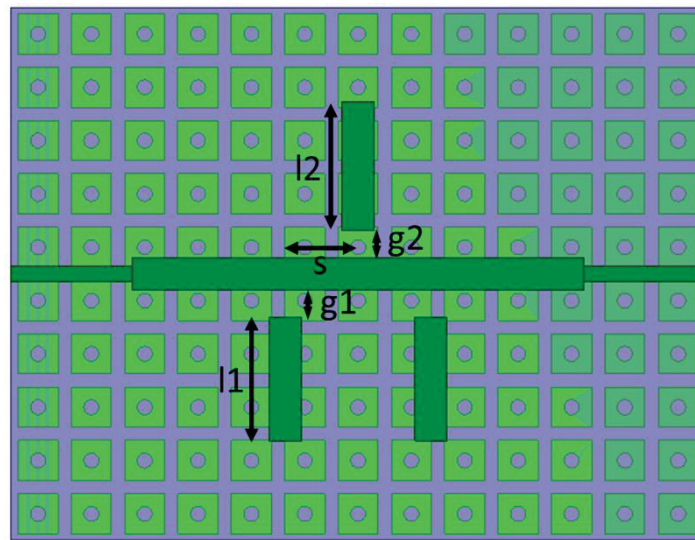
Figure 4-10. Third order bandstop filter using PRGW technology. The top metallic layer and microstrip transitions are not shown.

4.5.2. Realization of a Third Order Bandstop Filter on PRGW

Figure 4-10 illustrates the geometry of the proposed bandstop filter on the new improved PRGW. Resonators are realized using half wavelength lines that are coupled to the main line. All the layers are placed as shown in Figure 4-1, which include MS transition lines too. Since the structure is symmetric, it is only required to design two resonators and gap dimensions. For the proposed PRGW, as the structure is not uniform, careful attention is needed in the design of each resonator section regarding the relative placement of the mushroom cells beneath it. Therefore, it is important to consider the correct geometry of cells in the model of each section. Another parameter that should be calculated carefully

is the spacing between resonators (*s*). Based on theory, the resonators should be spaced at a quarter of a wavelength distance from each other that can be calculated from the dispersion diagram in Figure 4-3. However, due to the effects of the mushroom cells that excited some evanescent modes, the parameter, *s,* has to be modified to realize the required 90˚ phase difference.
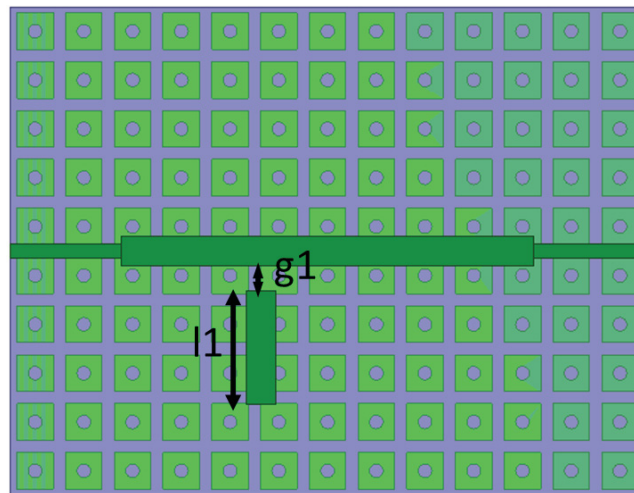
Figure 4-11.   EM model for the design of Resonator 1.
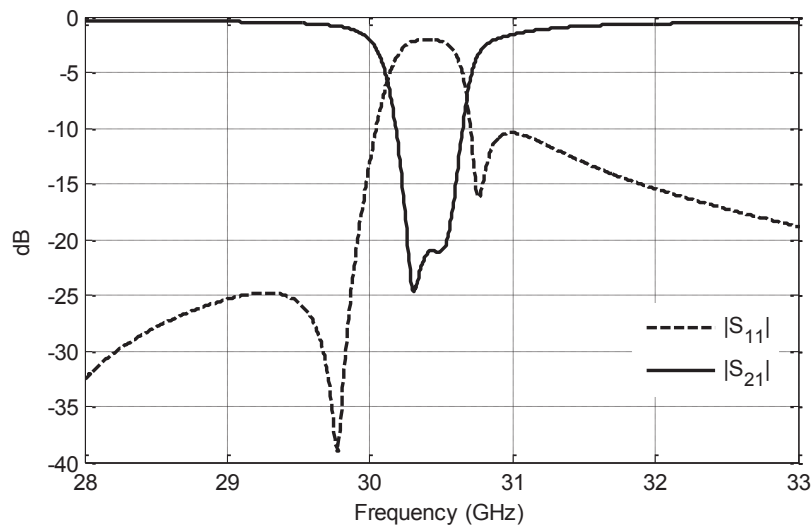
Figure 4-12.   The initial response of the third order bandstop filter using the parameter *s*=2.2 mm.

As an example, the design of third order filter in 30-31 GHz with 0.1 dB ripple is discussed here. After calculating the Chebyshev coefficients, using (4-2), the slope

parameters are $x_1 = x_3 = 0.5912$ and $x_2 = 0.5316$. Then, using (4-3), each resonator and gap are calculated by full-wave simulation of resonator's model that includes the correct position regarding the mushroom cells. For the parameters s, the initial value is chosen from the dispersion diagram for $\lambda_g/4 = 2.2$ mm at the center frequency of 30.5 GHz.

Table 4-1.   Optimized parameters of the third order bandstop filter in Figure 4-10.

Parameter	Value (mm)	Parameter	Value (mm)
l1	3.4902	g2	0.756
l2	3.6205	s	2.05
g1	0.7578		
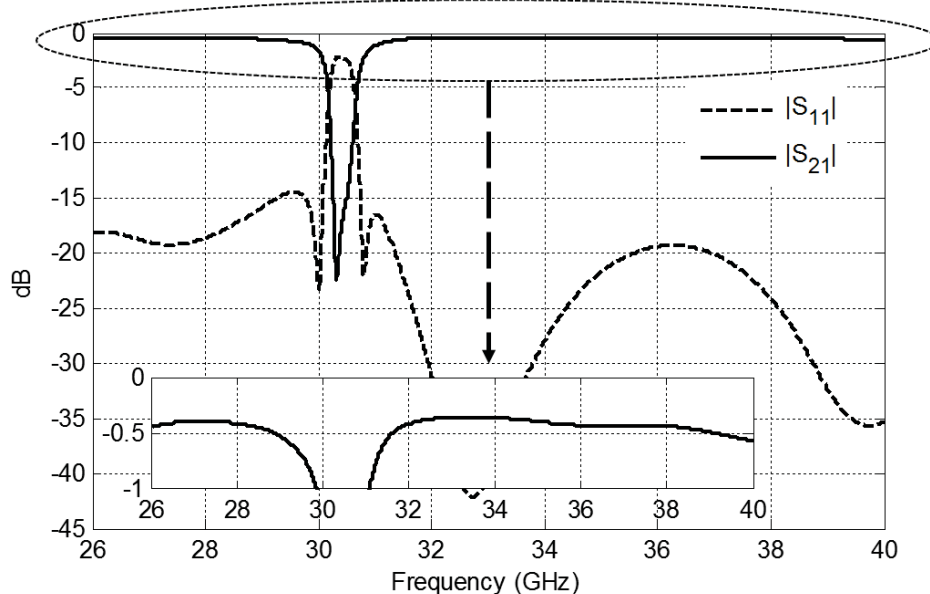
Figure 4-13.   Final optimized response of third order bandstop filter using the corrected separation between the resonators (s=2.05 mm).

The EM design model of Resonator 1 is shown in Figure 4-11. Figure 4-12 shows the initial response after calculation of all the parameters. As it can be seen, the response is not completely symmetric. By performing some analyses on the circuit model in Figure 4-8, it can be concluded that the separation between the resonators is bigger than $\lambda_g/4$ which causes such behavior. As there is no exact method to calculate the parameter, s, it is required to repeat the design procedure for few iteration of s to find the correct values. Therefore, the parameter, s, is decreased in 0.05 mm increments. For each new

69

value of *s,* it is necessary to redesign the first resonator as its relative position to the mushroom cells has changed. Finally, by using *s*=2.05 mm, the symmetric response is achieved which is shown in Figure 4-13. The final optimized parameters are listed in Table 4-1. The designed filter has a god matching level in the passband in a way that is covering the complete Ka-band. Also, the insertion loss performance is satisfactory considering that no packaging box is present in the structure and as the result, the structure is compact and light.
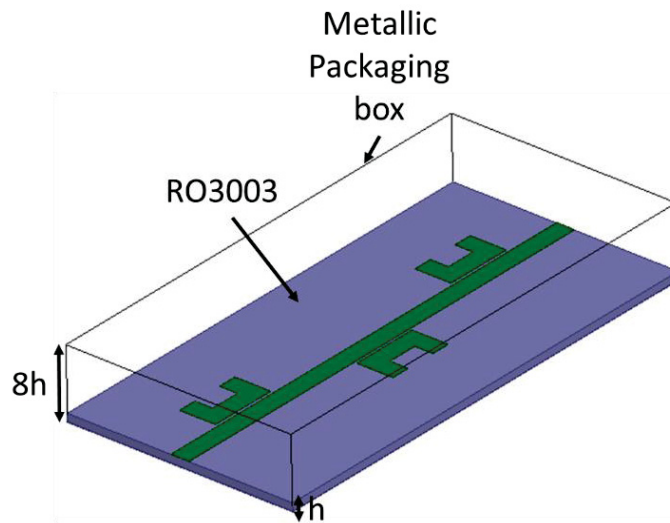
Figure 4-14.   Third order MS bandstop filter.

4.5.3.   Comparison to MS and Rectangular Filters

In order to comprehend the benefits of the proposed gap waveguide technology, it is important to compare the performance of the designed bandstop filter to other available technologies in different aspects. To this end, same third order filter is developed in MS and waveguide technology. The geometry of the MS filter is shown in Figure 4-14. To have a fair comparison, same RO3003 material with the same thickness of 0.254 mm is used. Because the couplings in MS circuits are weak, it is required to use a folded configuration for the resonators. Otherwise, the gap sizes would end up as some unrealizable values. The spacing between the resonators in this design had to be specified at $3\lambda_g/4$ since the interaction between the resonators is very strong due to the radiation of MS lines at this frequency band. In the PRGW design, the existence of the mushroom cells cancels such an interaction. Therefore, the resonator could be put $\lambda_g/4$ apart. Also, a metallic packaging

70

box is required to avoid the radiation loss from the circuit. The height of the box is set at 8*h* with *h* being the thickness of the substrate as a standard procedure [25].
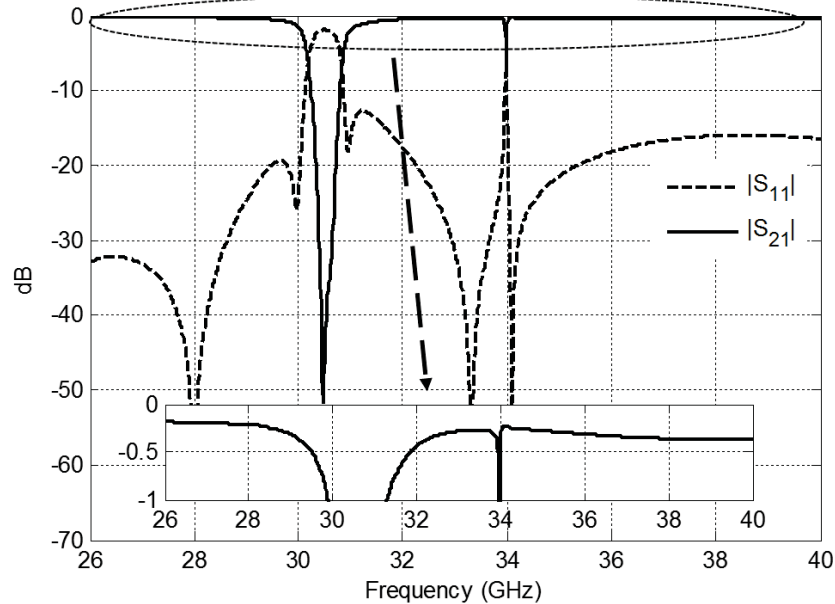
Figure 4-15.   Simulated response of third order MS bandstop filter.

Interestingly, the loss performance of the MS filter is better than the PRGW structure. However, due to the resonant modes of the packaging box, spikes appear in the passband of the filter. After performing optimization on the size of the packaging box, optimum performance is achieved to maximize the usable passband. However, a single resonant mode still exists at around 34 GHz. Moreover, the size of the structure is considerably bigger and heavier compared to PRGW filter due to the existence of the metallic packaging box and large spacings between the resonators. A similar issue was observed in Section 3.8 where the bandpass PRGW filters are compared to MS prototypes. Packaging the MS circuits is known as a crucial and troublesome issue mainly because of the resonant modes of the box itself.

In order to compare the PRGW technology with waveguide technology, the same filter is designed using a WR-28 standard waveguide. As the matter of the fact, the PRGW waveguide in this chapter is designed in order to compete with a WR-28 standard that covers the Ka-band (26.5-40 GHz). Therefore, it is of interest to compare their

performance with a similar design. Several geometries are feasible to realize the same third order filter with 0.1 dB ripple. The first geometry is shown in Figure 4-16 in which resonators are coupled to the main waveguide using H-plane irises. In such a configuration, it is not possible to place the resonators $\lambda_g/4$ apart from each other, since the resonators coincide with each other. Therefore, the filter is designed with $3\lambda_g/4$ separation between them. The simulated response of the filter is plotted in Figure 4-17 after designing all the parameters as it explained in the Section 4.5.1. The return loss in the passband deteriorates due to increased phase difference between the resonators. Therefore, it is required to improve the design with a non-uniform waveguide section between them as in the model of Figure 4-9. Such a design is very complex and requires many optimization procedures.
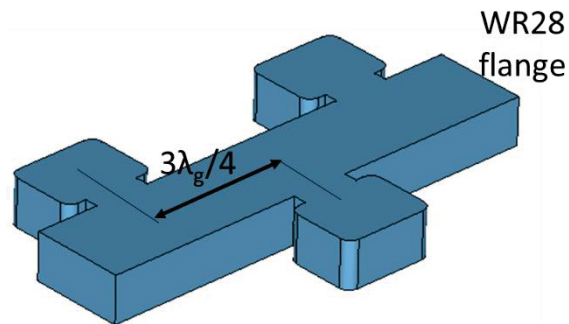
Figure 4-16.   WR-28 bandstop filter with H-plane irises.

Another possible configuration to realize bandstop filters in waveguide technology is shown in Figure 4-18 where the resonators are coupled to the waveguide from wide wall. In such a structure, the resonators can be placed at a $\lambda_g/4$ spacing from each other. However, the interaction between the resonators is strong and causes a discrepancy between the intended reject bandwidth and the achieved one. Also, the rejection level deteriorates strongly, and three ripples with high values appear in the S_{21}. This is shown in Figure 4-19. Therefore, this configuration is not a desirable one in waveguide structures. Interestingly, even in such a case, it not possible to cover the complete Ka-band with acceptable matching level. As it can be seen, at the high end of the band, the return loss deteriorates significantly. In all the waveguide examples, insertion loss is significantly lower compared to PRGW filter in the frequency range that acceptable matching level is achieved. However, covering the full operating bandwidth is not possible with a simple structure.

It can be concluded from the discussion in this section that a dispersion-less guiding medium is a more desirable solution to realize bandstop filters. It is shown in the case of the MS and PRGW bandstop filters that these configurations can provide a wide matched passband because they support a dispersion-less mode, while for the rectangular waveguide, since the propagation constant varies nonlinearly versus frequency, the phase difference between the resonators changes significantly at different frequencies. This phase error affects the matching in the passband of the filter at frequencies away from the stopband.
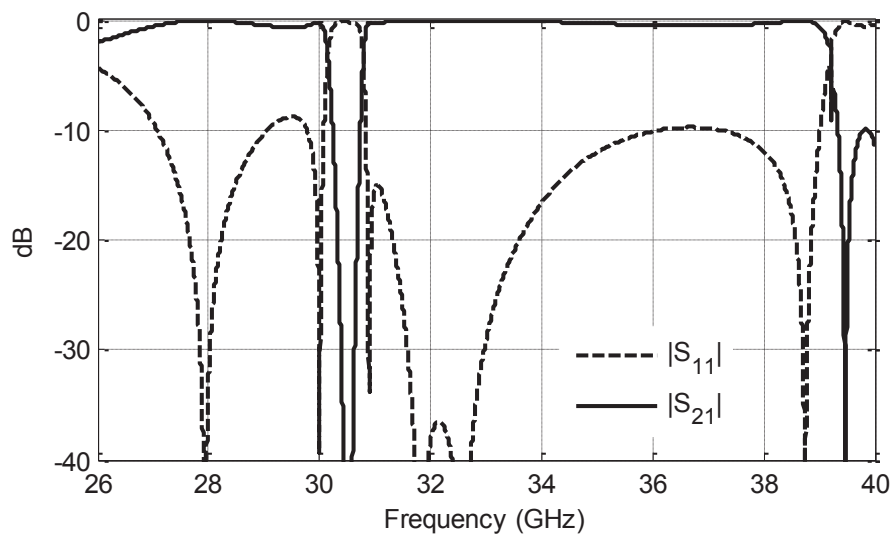
Figure 4-17.   Simulated response of the WR-28 bandstop filter in Figure 4-16.
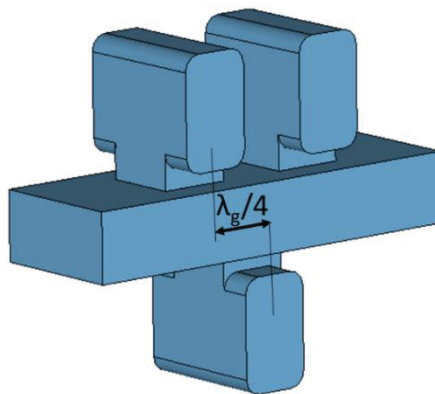
Figure 4-18.   WR-28 bandstop filter with resonators placed on the wide wall.
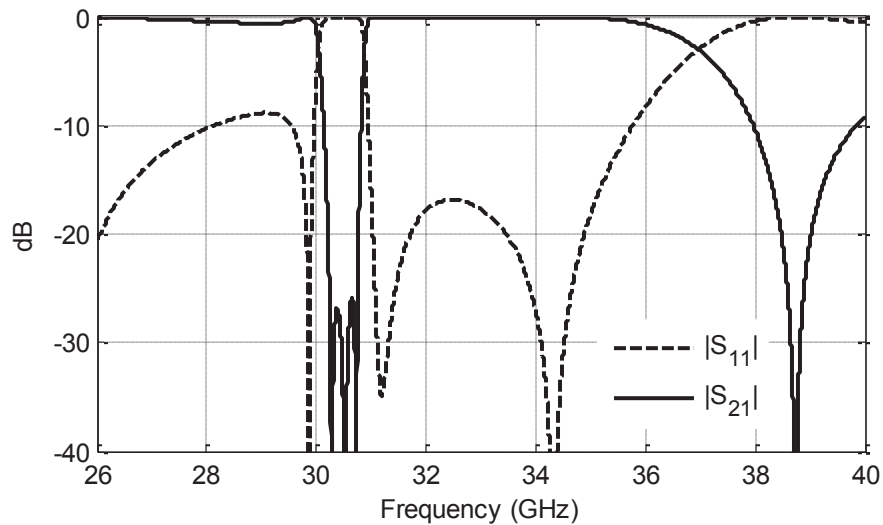
Figure 4-19. Simulated response of the WR-28 bandstop filter in Figure 4-18.

4.6. Low-loss Feeding Network for Antenna Arrays Using the Proposed PRGW

The antenna is the key element of any communication system, which can be utilized in mobile phones and the new generation of base stations at millimeter-waves. However, propagation loss at this frequency band is huge compared to the low-frequency band. Hence, it is required to design high-gain antenna arrays with low-loss and wide impedance matching as well as good radiation efficiency. Therefore, various approaches have been implemented to design high-gain antennas operating at millimeter-wave frequency bands. A survey on the development of high-gain antennas shows that several works have been carried out to increase the antenna gain at millimeter-wave. For instance, microstrip array antenna was suggested in [29], [30]. In [29], the authors designed a 4×4 patch antenna array fed by a modified L-shaped probe to achieve a gain of 15.2 dBi over 25.5% bandwidth. Although the antenna was printed on a single substrate and its fabrication is easy, the gain is not sufficient for practical applications, and it suffers from low radiation efficiency due to using the microstrip feeding network. The low-temperature co-fired ceramic (LTCC) technology is a promising candidate for millimeter-wave applications, and several works have been carried out to use this approach for high-gain antenna and bandwidth enhancement at millimeter-waves [31]–[35]. Such a technique is costly and has fabrication complexity.

The SIW feeding network is also another promising technique for designing antenna arrays at millimeter-waves. Although it has a good performance in terms of radiation efficiency, when it is employed in large arrays of millimeter-wave, the radiation efficiency is deteriorated [36], [37]. Moreover, integration of the active elements in SIW technology is an unsolved problem.

Recently, ridge gap waveguide has attracted considerable attention, owing to the fact that it can be employed as a low-loss transmission line compared to the microstrip line and SIW at millimeter-wave. Many authors deployed this technology in designing the feeding networks of antenna arrays at millimeter-wave [8], [38], [39]. For instance, a 2×2 slot-array antenna based on the ridge gap waveguide feeding network was proposed in [38] with a maximum gain of 12.2 dBi at 12-15 GHz. Also, a slot array antenna by using PRGW feeding network is reported in [8] where each slot antenna is the source of four radiating cavities backed slot radiators. Although the directivity corresponds to 20.1 dB at 60 GHz, the side-lobe level is less than -6.5dB at 62 and 66 GHz, which restricts its application. Furthermore, loading the subarray increases the height of the antenna and adds complexity to the design.

In this section, a planar 4×4 antenna array is developed based on the proposed PRGW over 28.8-34 GHz. To achieve a proper impedance matching as well as gain, we have used magneto-electric (ME) dipole antenna as a radiator. A prototype of the antenna is fabricated, and its performance is measured. The measured results confirm that the antenna gain is higher than 20 dBi in the frequency range of 29.7-33 GHz. Also, the radiation efficiency is better than 88% in the entire frequency band of 28.7-33 GHz. The resulting radiation patterns in the E- and H-planes prove that there is a good agreement between the simulated and measured results. Also, the SLL in both E- and H-plane is less than -12 dBi over a frequency range of 29-33 GHz.

The advantage of the proposed 4×4 ME dipole antenna arrays is achieving 16.5% matching bandwidth, 2 dB gain bandwidth of 16.3%, and maximum radiation efficiency of 88% at 30 GHz. The performance is excellent compared to the 4×4 antenna arrays in [35] with impedance matching of 13.96%, 2 dB gain bandwidth of 8.1%, and radiation efficiency of 63.1% at 37 GHz. In addition, due to using the proposed microstrip transition, we can

easily excite the antenna by microstrip line instead of a waveguide. By using the modified PRGW, the ridge is separated from the plated vias. Therefore, we have this degree of freedom to select a proper distance between each element in both E- and H-plane so as to prevent the excitation of grating lobe compared to the former slot antenna arrays with PRGW, which suffers from the grating lobe [8], [39].
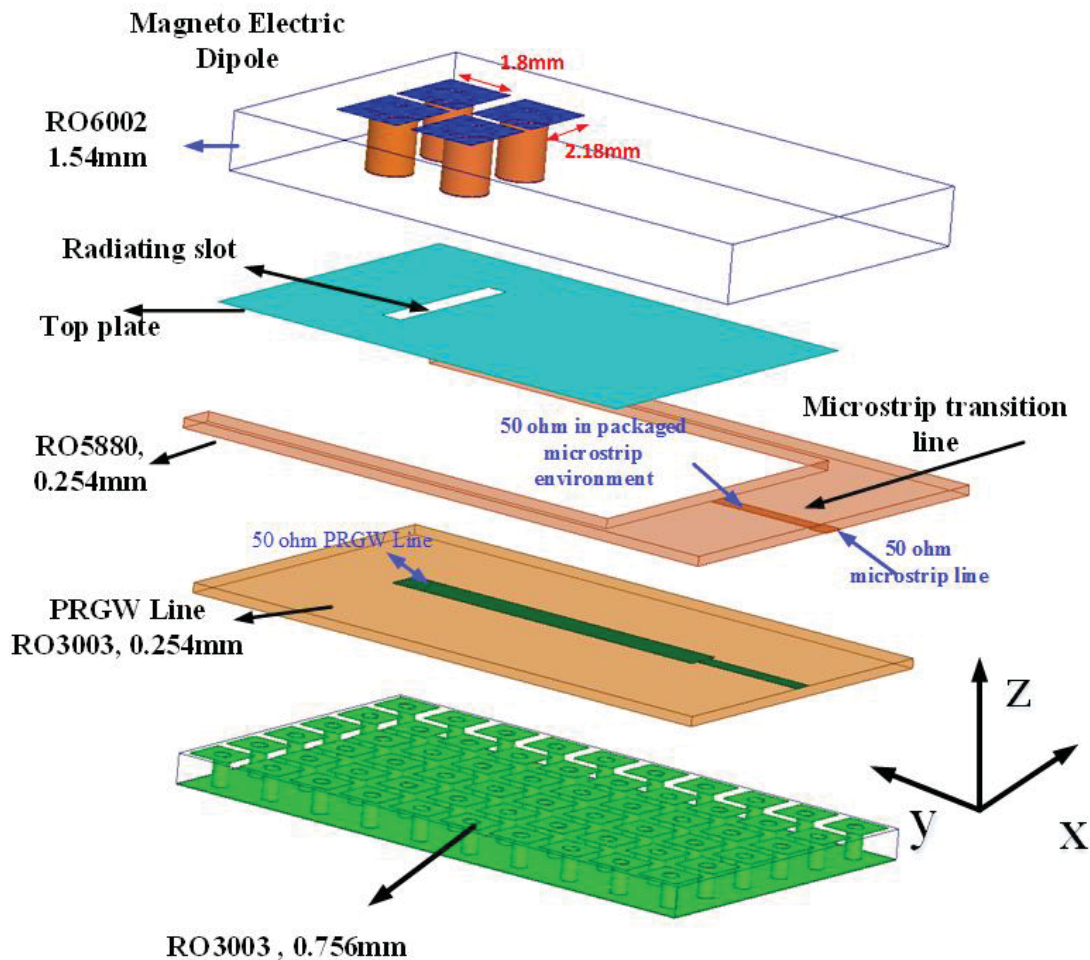
Figure 4-20.   The structure of the PRGW ME dipole antenna.

4.6.1.   Magneto-Electro Dipole Antenna

The configuration of the proposed ME dipole antenna based on a printed ridge gap waveguide is shown in Figure 4-20. The top plate is the ground of the fourth layer (RO6002 with a relative dielectric constant 2.9, and thickness of 1.54 mm), where the rectangular slot with dimensions of 1.8 × 1.2 mm^2 is etched on that to couple the electromagnetic waves toward the z-direction. The slot antenna itself has a narrow frequency bandwidth.

To increase the bandwidth, a Magneto-Electric (ME) dipole antenna is applied as indicated in [40]. In fact, the Magneto-Electric dipole antenna consists of an electric and magnetic dipole, which is made to achieve a wider bandwidth as shown in Figure 4-21, compared to the slot antenna. The ME dipoles are printed on the top layer of the fourth substrate (RO6002). The top dipole patches are connected to the ground plane by vertical vias with a radius of 0.6 mm. In fact, the electric dipole corresponds to the two pairs of rectangular patches and a magnetic dipole is related to the aperture between the rectangular patches. Loading the slots by the ME dipole antennas increases the antenna gain by 3 dB as shown in Figure 4-22, compared to the slot antenna.
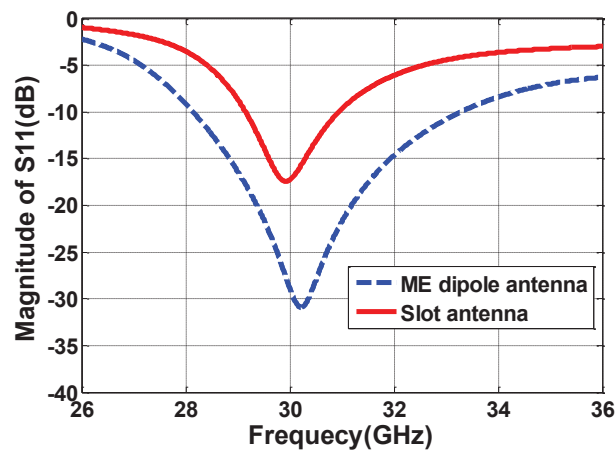
Figure 4-21.   The S-parameters of the slot antenna and ME dipole antenna.
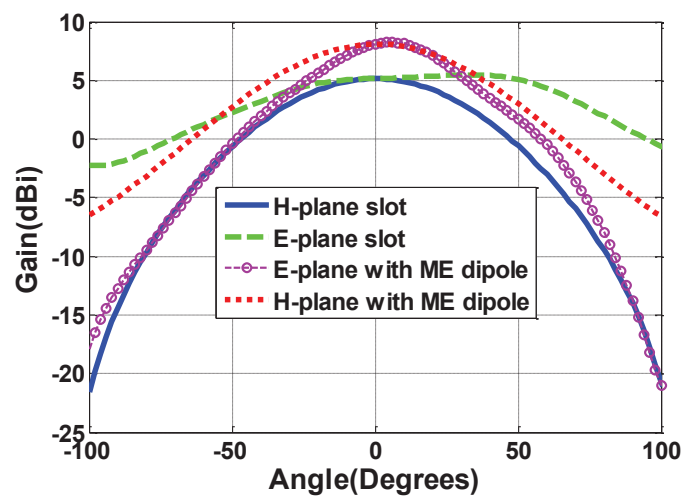
Figure 4-22.   The E and H-planes radiation pattern of the ME dipole antenna and a slot antenna.

77

4.6.2.   A 4×4 ME Dipole Array Antenna

In this section, we propose a design of a 4×4 array antenna to achieve an antenna gain of 19 dBi and higher. For this purpose, first of all, we have designed a T-junction feeding network to cover the frequency bandwidth from 28-35 GHz. The proposed T-junction is shown in Figure 4-23. The configuration of different layers is as explained in Figure 4-1 in which all the lines and circuit details are printed on the second layer. In Figure 4-23 the metallic top plate and the substrate for microstrip transitions are not shown. The resulting S-parameters of the T-junction power divider are shown in Figure 4-24. It can be seen that the magnitude of S_{11} is below -10 dB over the frequency band of 26-38 GHz. Also, the power is equally distributed on the two arms with the same magnitude.
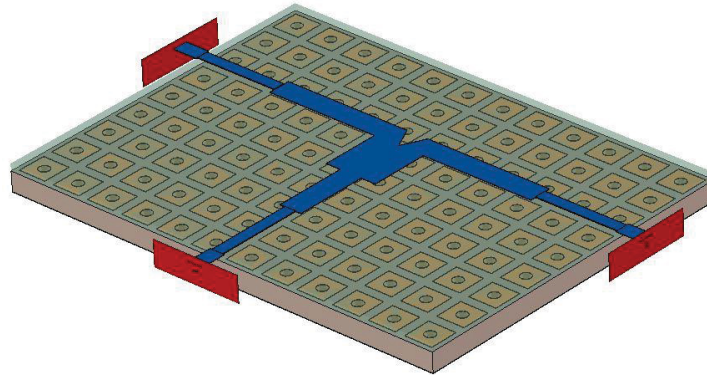
Figure 4-23.   The schematic of the T-junction power divider.
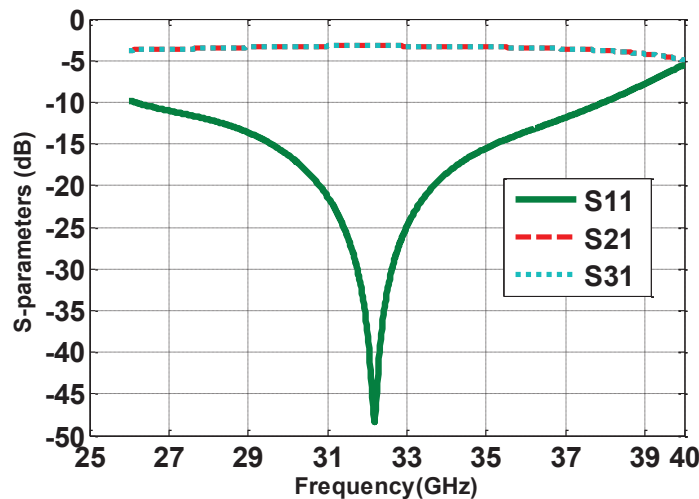
Figure 4-24.   The S-parameters of proposed T-junction power divider.
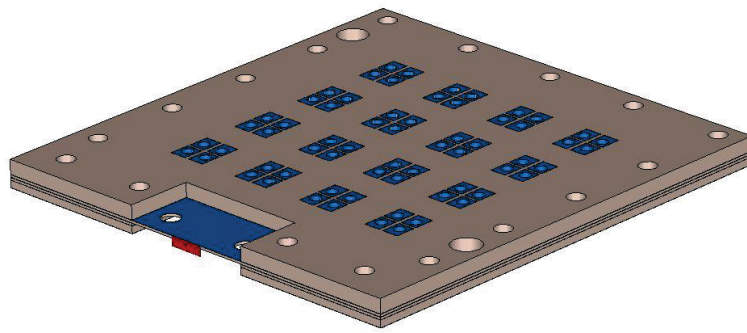
(a)
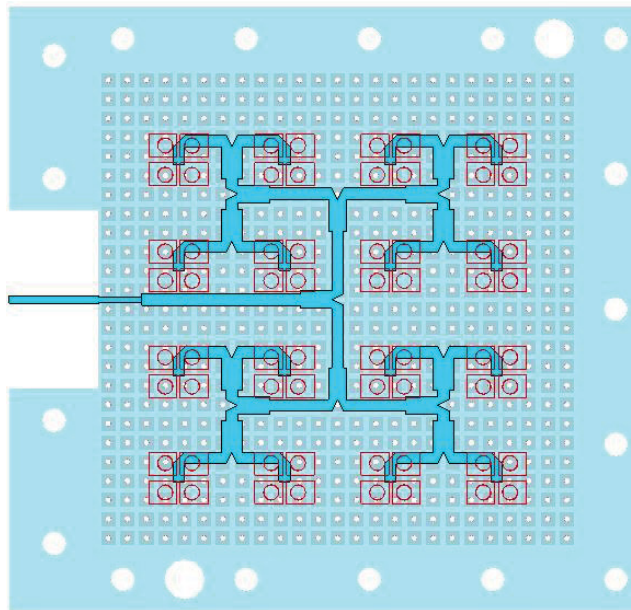
(b)

Figure 4-25.   The schematic of a 3D configuration of 4×4 ME dipole array antenna.
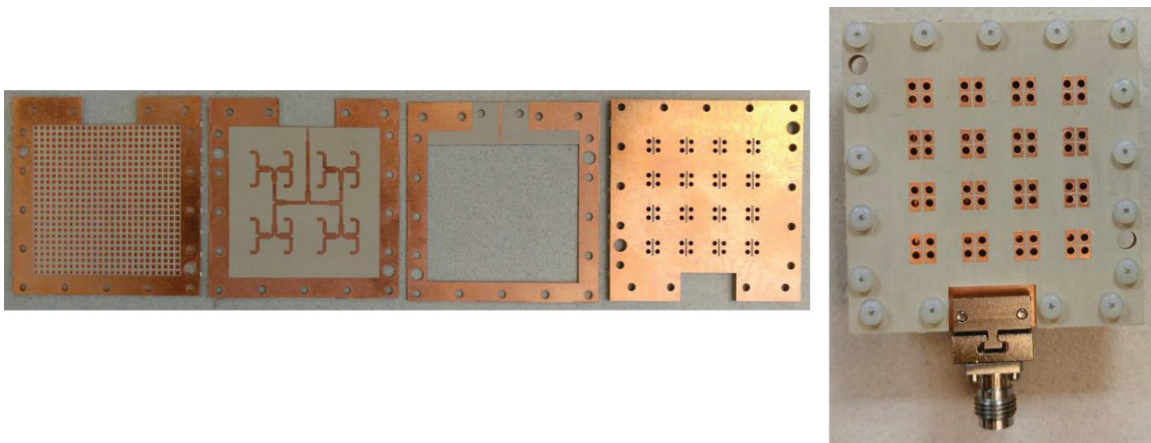
Figure 4-26.   The photograph of the proposed array of 4x4 ME dipole antenna.
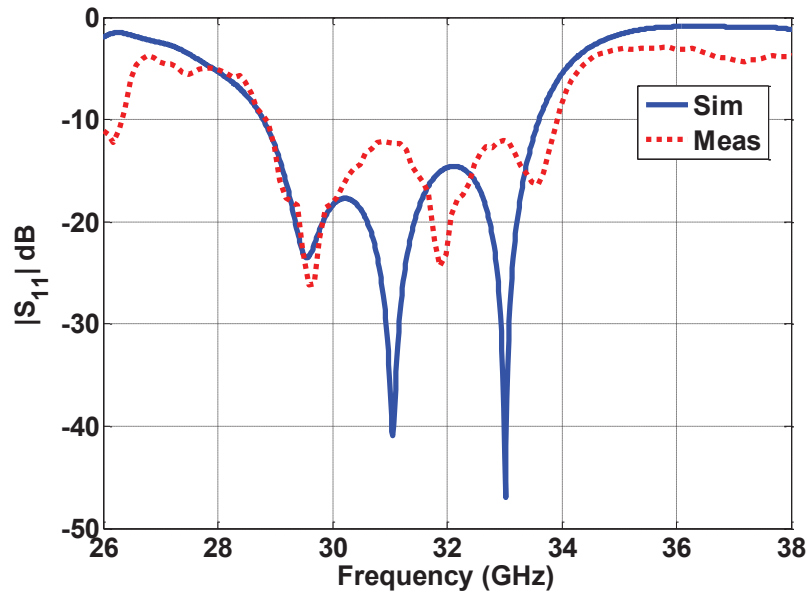
Figure 4-27. **The reflection coefficient of 4x4 ME dipole antenna array**.

Using the developed antenna element and the T-junction, a 4×4 array of ME dipole based on PRGW technology was designed. The 3D and 2D perspective of the 4×4 array of ME dipole antennas are shown in Figure 4-25. This configuration is comprised of three substrate layers as explained in Section 4.6.1 for the single ME dipole antenna. In the first layer, an array of mushroom-like EBG cells is located. In the second layer, a 4×4 feeding network is used to split the input power to 16 antenna elements. The propagation in the feed network is inside the air-gap between the second layer and the top plate except some fringing fields in the dielectric materials. Therefore, the loss of the substrates is avoided to a great extent. To transfer the power from the feed network towards broadside radiation, ME dipole antennas are used on the third layer. It should be noted that with the current ridge gap waveguide, the designer has more freedom to adjust the distance between each ME dipole element to be less than λ_o, so as to suppress the grating lobe. Hence, the distance between each antenna element in both the E- and H-plane is selected to be 0.83 λ_o at 30 GHz to prevent the effect of a grating lobe in both planes. It is important to mention that we have created 18 circular holes on the edge of each substrate to align and connect the layers precisely by using screws.
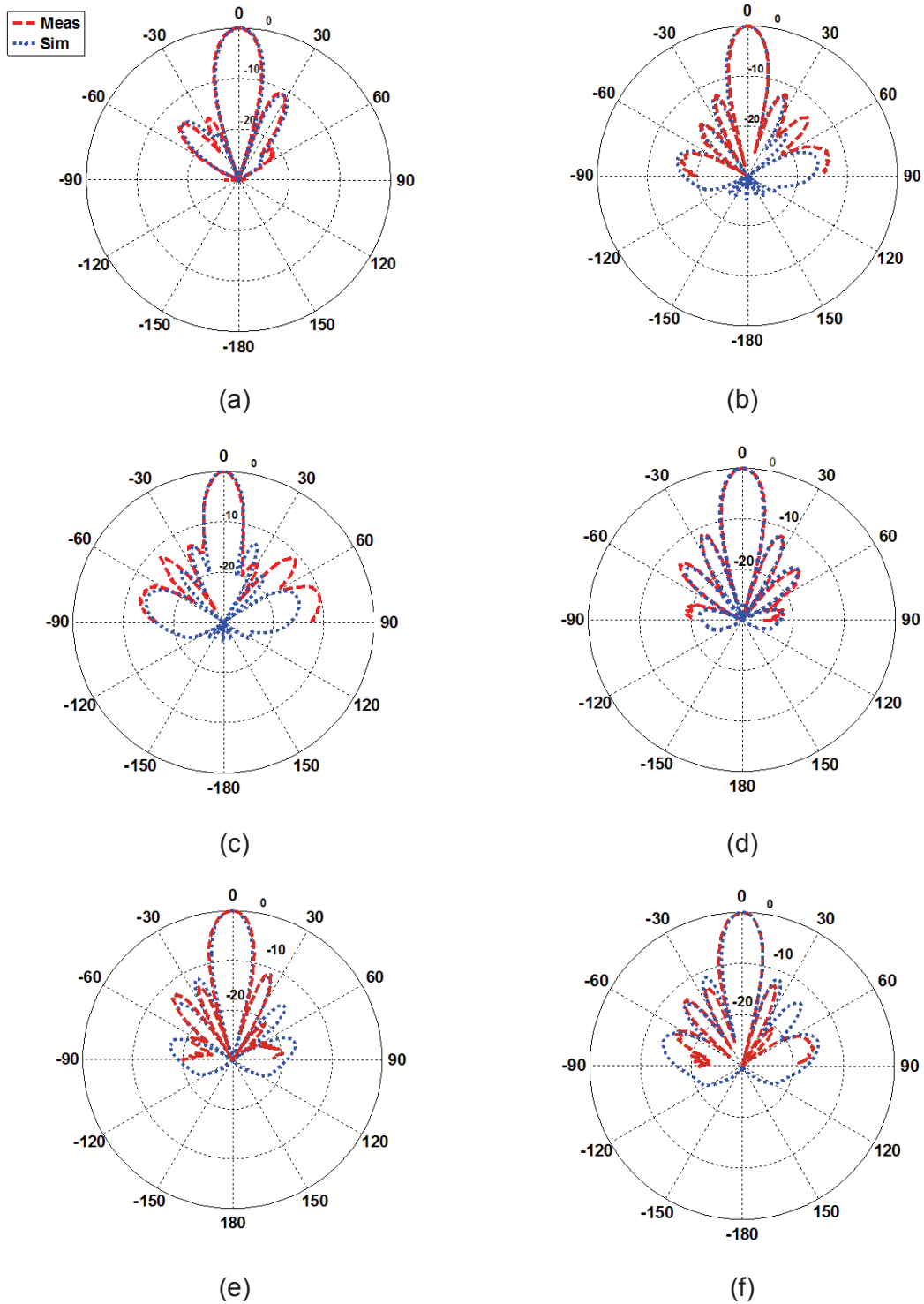
Figure 4-28. Measured and simulated normalized radiation patterns of 4x4 array antenna in the E-plane at (a) 30 GHz, (b) 32 GHz, (c) 34 GHz, in the H-plane at (d) 30 GHz, (e) 32 GHz, (f) 34 GHz
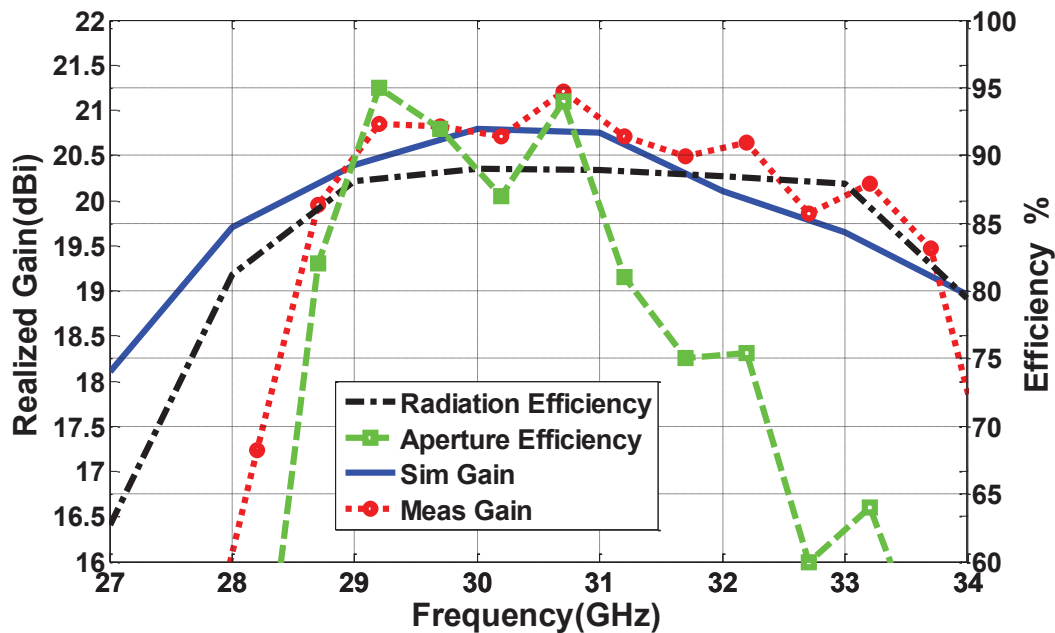
Figure 4-29. The simulation and measured realized gain along with the efficiency of the 4x4 ME dipole antenna array.

The fabricated prototype is shown in Figure 4-26. To measure the characteristics of the antenna, an end-launch 1.85 mm connector is used. The magnitude of the reflection coefficient is shown in Figure 4-27 for both simulation and measurement. The measured reflection coefficient is smaller than -10 dB over the frequency band of 28.8-34 GHz. The resulting radiation patterns of the antenna array in the E-plane at three different frequencies of 30, 32, and 34 GHz are shown in Figure 4-28(a-c). It can be seen that the SLL is less than -12 dB over the entire frequency band , which is better than the 4 x 4 antenna array in [8] with side-lobe level of -6.5 dB. Also, there is a good agreement between the simulated and measured results. Furthermore, the H-plane radiation patterns at 30, 32, and 34 GHz are shown in Figure 4-28(d-f), where the magnitude of SLL is also better than -12 dB. The antenna gain is calculated by using the gain comparison method. Also, the effect of the connector loss is taken out from the measurement. The measured realized gain of the 4×4 ME dipole antenna arrays, shown in Figure 4-29, indicates that the antenna gain is more than 20 dBi over the frequency range of 29.8-33 GHz. Also, the maximum gain of 21.2 dBi occurs at 31.5 GHz.

We have compared the characteristics of the proposed ME dipole antenna array with the former reported SIW antenna arrays in Table 4-2. It can be perceived that the

proposed 4×4 antenna has a better performance in terms of bandwidth, gain, as well as efficiency compared to the SIW antenna arrays in [34], [35], [41]. Most importantly, it has a 94% aperture efficiency at 30 GHz. Moreover, the 8x8 ME dipole antenna arrays have an excellent radiation efficiency of 81.3% compared to those in [32] and [37], which had a radiation efficiency of 31% and 68.5%, respectively.

Table 4-2. **The comparison of the proposed ME dipole antenna array with the former SIW antenna arrays at 30 and 60 GHz.**

	Size (λ_0)	Bandwidth %	Peak Gain (dBi)	Efficiency %	Element number	Aperture Efficiency
This work	$3.5\lambda_0 \times 3.4\lambda_0 \times 0.28\lambda_0$ @30 GHz	16.5	21.2	88	4×4	94
[35]	$3.2\lambda_0 \times 3.2\lambda_0 \times 0.31\lambda_0$ @37 GHz	13.96	19.1	63.1	4×4	-
[34]	$4.2.\lambda_0 \times 4.2\lambda_0 \times 0.096\lambda_0$ @60GHz	13	16.5	20.2	4×4	-
[41]	$2.35\lambda_0 \times 2.24\lambda_0 \times 0.05\lambda_0$ @30 GHz	14.28	13.5	92	2×2	-
[32]	$6.2\lambda_0 \times 9.4\lambda_0 \times 0.38\lambda_0$ @60 GHz	17	22.1	33.6	8×8	86
[37]	$6.08\lambda_0 \times 6.8\lambda_0 \times 0.82\lambda_0$ @60 GHz	14.1	26	68.5	8×8	86

4.7. Conclusion

A new concept has been presented to design low-loss planar circuits using printed gap technology with improved design feasibility. The concept has been performed by separating the EBG mushrooms from the guiding lines and resonators in two different layers. Such a geometry provides many benefits in terms of design procedure and bandwidth, and still the low-loss behavior of gap waveguide technology is preserved. Three measured examples have been presented to prove the concept. The first one is a long line with two 90° bends that shows low losses and good return loss behavior. Another example is a quadruplet bandpass filter. The third example is a 4×4 antenna array based on the ME dipole concept. The quality factor of a half wavelength resonator in the presented configuration has been calculated and compared to conventional gap waveguide technology that was discussed in Chapter 3. The design of bandstop filters using the proposed structure is discussed. By proposing a robust procedure, bandstop filters can be designed in PRGW. The performance of the bandstop filter is compared to

MS and waveguide filters with different geometries. It is shown that proposed PRGW has some advantages compared to an MS line regarding loss performance and being a self-packaged circuit. Compared to the rectangular waveguide, the PRGW has considerably lower fabrication cost and weight. Also, since the PRGW is a TEM waveguide, it supports dispersion-less propagation. Therefore, it is preferred in many applications, such as in the design of bandstop filters that was discussed in Section 4.5.

Chapter 5.

Use of Group Delay of Sub-Circuits in Optimization of Wideband, Large-Scale Bandpass Filters, and Diplexers

5.1. Introduction

The coupling matrix [10] for the design of cavity-coupled microwave filters has been an interesting research topic for more than five decades. Hence, considerable development and optimization techniques are based on this method [20], [42]–[44]. Plenty of configurations have been developed based on the coupling matrix (CM) that probably can satisfy the filtering requirements of any existing communication system. However, the classic coupling matrix methodology is limited to filters with narrow bandwidth. The definition in [45] of narrowband filters, are those with less than 1% of bandwidth. Some attempts were made to extend the coupling matrix to filters with arbitrary bandwidths as in [46], which is promising. However, it suffers from complexity, and not many designs based on this method exist in the literature. In addition, extracting the coupling parameters from simulated or measured scattering parameters is useful in the optimization of filters, but questions still exist for designs based on this method. For moderate bandwidths, the classical coupling matrix method [47] can be used. However, it needs huge optimization efforts when the initial response is not close to the ideal response. Moreover, conventional coupling matrix extraction methods as [26], [48], [49] and also optimization based extraction cannot be used as the dispersive behavior of coupling elements will yield additional transmission zeros, which leads to non-zero couplings that do not exist in the electromagnetic model. Another coupling matrix extraction method that was proposed in [15] is based on the group delay response of each sub-circuit for the tuning of each coupling element and resonator, one by one. This technique was proposed for narrowband filters, but as in this method the group delay response of the sub-circuits in the passband is used, the dispersive behavior in wideband cases will not intervene with the extraction process. However, the extracted values should be considered as an equivalent coupling because the couplings are not constant over the wide passband. Here, we are using this

technique in combination with space mapping method to calculate the dimensions in the design of wideband large-scale bandpass filters and diplexers from the pre-designed coupling matrices.

In this chapter, a systematic procedure is proposed by dividing the structures into many sub-circuits and extracting the equivalent coupling matrix by optimization of the lumped element model based on CM. Then a mapping is needed to relate the circuit parameters to the electromagnetic (EM) model. The calculated response will not be identical to ideal required behavior in some cases, but it is good enough to be used in a full-wave EM optimization that will converge easily by using the correct goal function. Initially, the method is explained during the design of a novel stacked cascaded quadruplet filter with 6.7% bandwidth. This is the first design that we optimized using the proposed method. Later, we introduce a technique to make the design procedure independent of full-wave optimization by mimicking the loading effect of the last cavity in each sub-circuit. Wideband all-pole filters with fractional bandwidths up to 20% are designed based on this method. Finally, the design of wideband high-order diplexers is addressed. Using the proposed method, a diplexer with a total bandwidth of approximately 20% is designed without using any full-wave optimization.

5.2. Stacked Quadruplet Configuration

Initially, we will explain the optimization method using a novel compact geometry. We used two quadruplets (CQ) in a stacked configuration to achieve an eighth order bandpass filter with four transmission zeros (TZs). The geometry is shown in Figure 5-1. The passband is between 7.25 and 7.75 GHz. The rejection requirements are very high in this design. It is required to have 70 dB rejection level below 7 GHz and 90 dB beyond 8 GHz. Hence, one TZ is located on the left side and three on the right side of the passband to achieve the requirements. For compactness and size constraints, a stacked configuration is used. The required reflection is -18 dB. Using the traditional synthesizing procedure outlined in [47], the resulting coupling matrix is a full matrix, which requires series of similarity transforms to annihilate the non-existing couplings based on the diagram in Figure 5-1(d). The relations for the required pivotal positions and rotation angles can be found in [50]. The resulting coupling matrix is shown in Table 5-1. Input and

output resistances are equal to $R_1 = R_2 = 0.9$. Scattering parameters of the calculated coupling matrix are shown in Figure 5-2, which can satisfy the rejection requirements of the design. It should be mentioned that M_{57} is small enough to be neglected; however, we decided to implement it in the design to maintain the generality of the method. An interesting point about the matrix in Table 5-1 is that all the couplings are positive except M_{78}, which is realized by an E-plane iris as shown in Figure 5-1(b). The response of the filter is not sensitive to the sign of M_{45}, which is the realized coupling by the slot. This slot couples the two quadruplets, which are realized in two different planes.

Table 5-1.   Calculated coupling matrix for cascaded quadruplet filter.

	1	2	3	4	5	6	7	8
1	0.0104	0.7715	0	01575	0	0	0	0
2	0.7715	-0.1573	0.3213	0.4094	0	0	0	0
3	0	0.3213	-0.7742	0.3592	0	0	0	0
4	0.1575	0.4094	0.3592	0.0518	0.5405	0	0	0
5	0	0	0	0.5405	0.0256	0.5380	0.0031	0.0608
6	0	0	0	0	0.5380	0.0105	0.6212	0
7	0	0	0	0	0.0031	0.6212	0.012	-0.7851
8	0	0	0	0	0.0608	0	-0.7851	0.0104

5.2.1.   Stacked Coupled TE$_{101}$ Cavities

As shown in Figure 5-1, Cavities 4 and 5 are coupled to each other by a slot in the lower plate. This configuration allows us to have a compact filter by arranging each quadruplet in a different plane. The structure is shown in Figure 5-3 along with the coupling coefficients that is calculated by [20]:

$$k = \frac{f_e^2 - f_m^2}{f_e^2 + f_m^2}$$

(5-1)

where f_e is the resonant frequency of half of the structure when PEC boundaries are placed in between and f_m is the same when PMC boundary is used. The distance of the slot from the sidewalls controls the coupling. As the magnetic field is stronger near the walls for the

TE_{101} mode in a rectangular cavity, moving the slot away from the walls decreases the coupling.
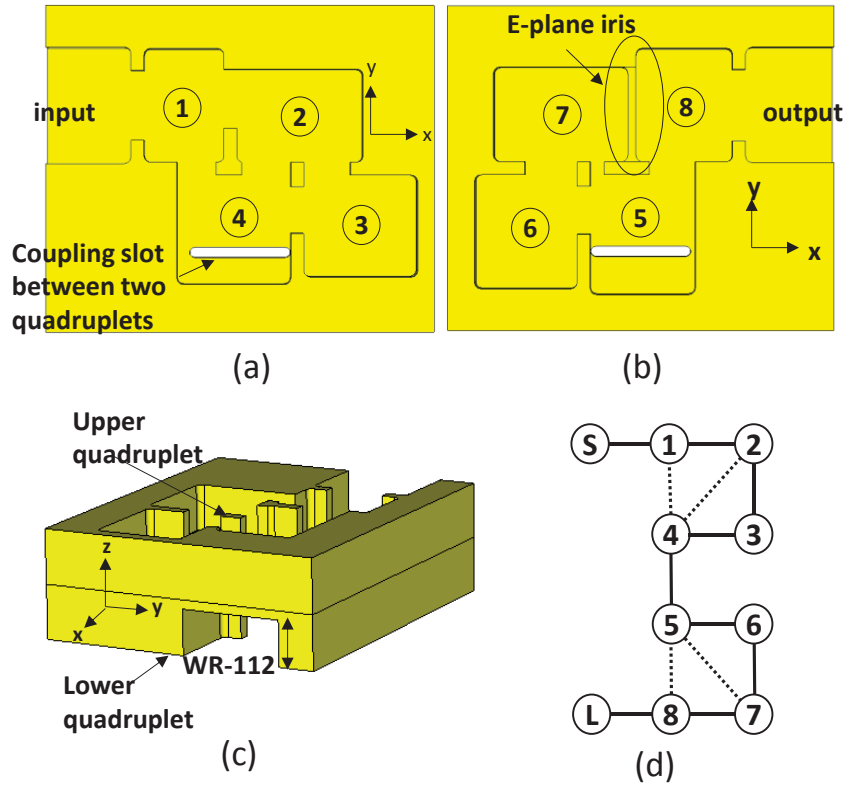
Figure 5-1. Stacked eighth degree bandpass filter. a) Upper quadruplet. b) Lower quadruplet. c) Complete structure without the covers. d) Coupling diagram.
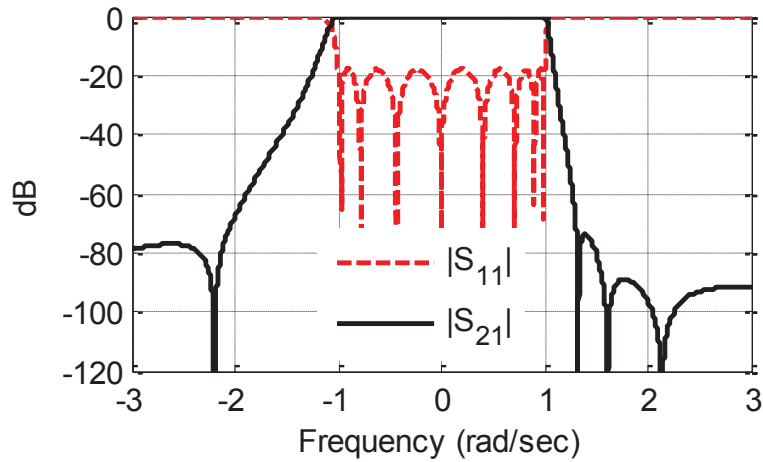
Figure 5-2. Response of calculated coupling matrix in Table 5-1.

Due to fabrication restrictions, the width of the slot is kept constant at 0.1" (2.54 mm). It is beneficial to have the slot as long as possible because the slot has its resonant mode that should be kept away from the passband of the filter as far as possible. When the length of the slot is 25 mm, the slot mode is resonating at 6.14 GHz. Therefore, we can anticipate that the rejection response of the complete structure will degrade at this frequency. Whether the coupling is capacitive or inductive depends on the length of the slot. In this specific design, a wideband coupling is needed, and the short slot cannot deliver the required un-normalized coupling of k_{45} = 0.0361, and the response of coupling matrix of Table 5-1 is not sensitive to the sign of M_{45}.
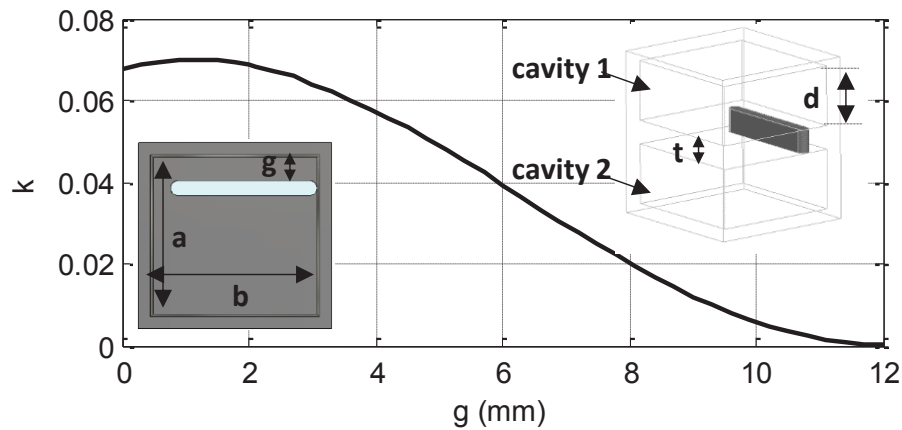
Figure 5-3.   Coupling coefficient of two stacked rectangular cavities in TE$_{101}$ mode. Parameters are as follow: a=26.8 mm, b=28 mm, d=12.6238mm, t=5mm, l=25mm.

5.2.2.   Design and Optimization Method

The design procedure consists of two steps. In the first phase, the initial dimensions are calculated using space mapping [14] in which the coarse model is the CM. The second phase is fine-tuning the design using full-wave EM solver. In the first step, the structure is divided into two sub-circuits as in Figure 5-4. First sub-circuit (Figure 5-4(a)) is the upper half that contains Cavity 1 to 4 and couplings between them along with the lower plane with de-tuned cavities. As shown in Figure 5-4(a), Cavities 5-8 are shorted using metallic rods inside the EM solver. Therefore, their resonant frequency is shifted to a much higher band. The group delay of S_{11} from Sub-circuit 1 is calculated using ANSYS HFSS. In this case, even though Cavities 5-8 are de-tuned, their physical influence is taken into account. In every step of calculating the EM response, the CM is optimized to

have the same response. In the CM, Resonators 5 to 8 are de-tuned by assigning their resonant frequencies to much higher values. The extracted couplings from the CM after optimization can be considered as equivalent couplings. Extracting coupling parameters from group delay response was first introduced in [15] for tuning filters after fabrication using provided tuning screws. We are using this method to tune the filter in the design process. One issue that wasn't addressed in [15] is the phase offset in the measured and simulated scattering parameters. It can be shown that phase offset of a bandpass filter is approximated by [26]:

(a)
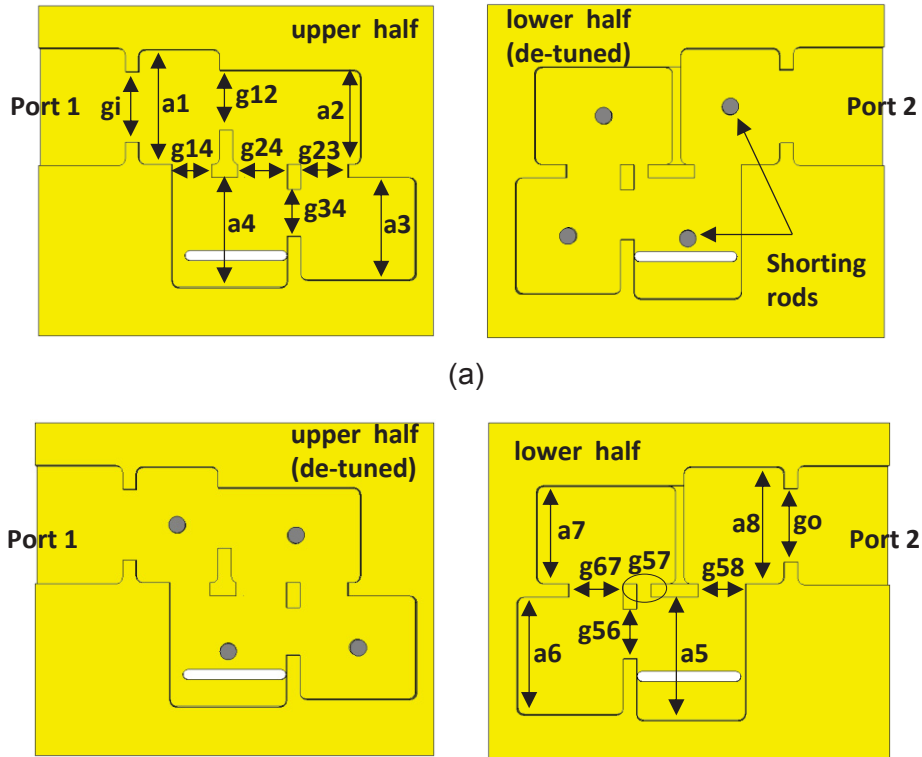
Figure 5-4. **(a) Sub-circuit 1 which consists of Cavities 1-4 with de-tuned Cavities 5-8. (b) Sub-circuit 2 which consists of de-tuned Cavities 1-4 along with Cavities 5-8.**

$$\varphi = \varphi_0 + \beta \Delta l. \qquad\qquad (\,5\text{-}2\,)$$

Where φ_0 is the constant phase loading created by evanescent modes, β is the propagation constant, and Δl is the equivalent length of the transmission lines that are feeding the filter and can be different from the physical length of input/output lines due to

the existence of the evanescent modes. In [26], a method is introduced to compensate both constant (φ_0) and varying (Δl) phase loadings in (5-2). Here, we are using group delay response, which is defined as:
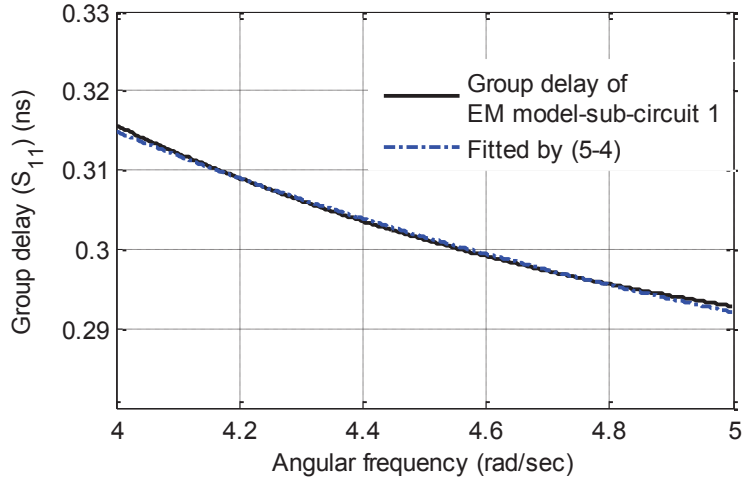
Figure 5-5.   Group delay of Sub-circuit 1 in lowpass frequency domain.
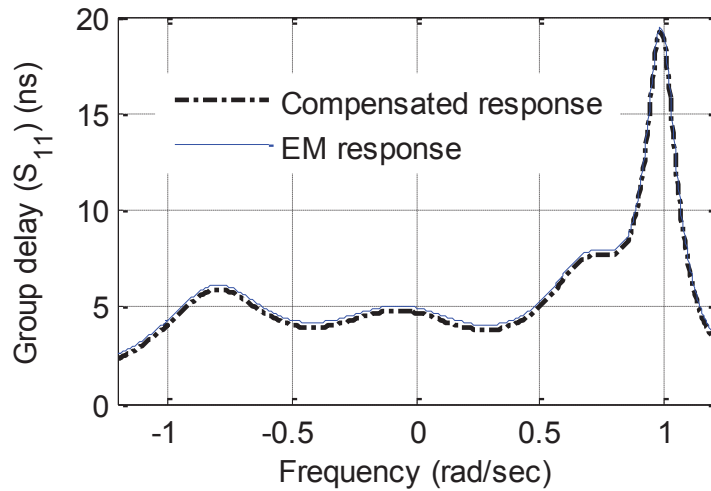
Figure 5-6.   EM and compensated group delay response of Sub-circuit 1.

$$\tau = -\frac{d\varphi}{d\omega}.$$ (5-3)

Therefore, it is not required to cancel the constant phase offset as it will be zero automatically from the differentiation. However, the second term in (5-2) is a frequency

dependent term that causes a shift in the simulated group delay response. To calculate this shift, the same method outlined in [26] is used for every sub-circuit instead of the complete filtering structure. The group delay response of S_{11} for Cavities 1 to 4 can be approximated in frequencies away from the passband by:
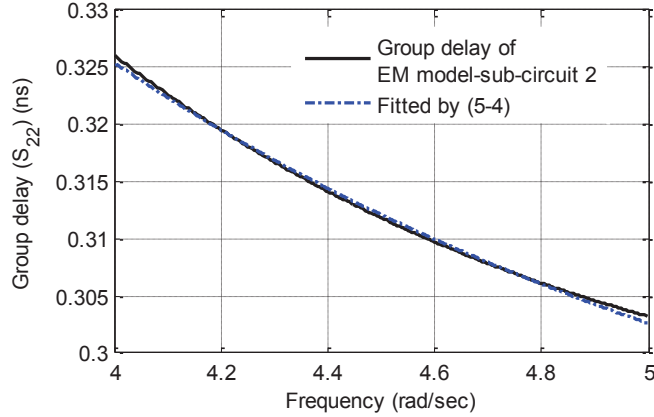
Figure 5-7.   Group delay of Sub-circuit 2 in lowpass frequency domain.
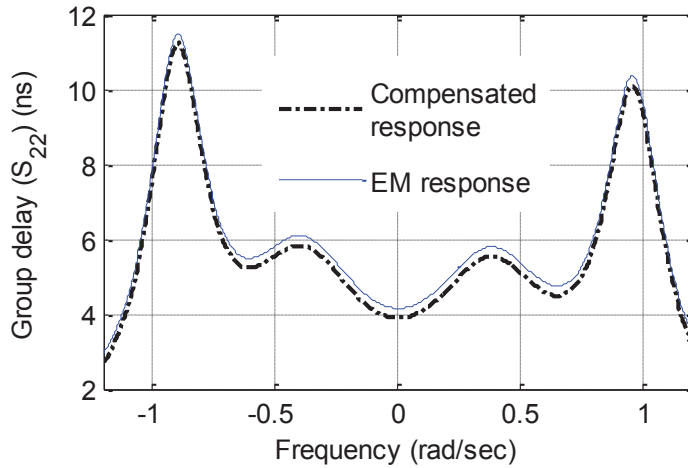
Figure 5-8.   EM and compensated group delay response of Sub-circuit 2.

$$\tau S_{11} = -\frac{a}{\Omega^2} - b \qquad (\text{5-4})$$

where a and b are constants, and Ω is the normalized frequency in lowpass domain. The constants in (5-4) can be found by least square fitting of the simulated results from ANSYS HFSS. Then, the compensated group delay of the sub-circuit is:

$$\tau S_{11}' = \tau S_{11} + b \qquad\qquad (\ 5\text{-}5\ )$$

where τS_{11} is the simulated group delay of the sub-circuit and b is the constant found from fitting in (5-4). Figure 5-5 shows the fitting process of the first sub-circuit, which consists of Cavities 1-4 along with de-tuned Cavities 5-8. After calculating b, compensated group delay response of S_{11} can be calculated using (5-5) as in Figure 5-6. Extracted value for b is -0.2515 ns for the associated length of 20.9 mm of the input waveguide. This value also can be calculated analytically by:
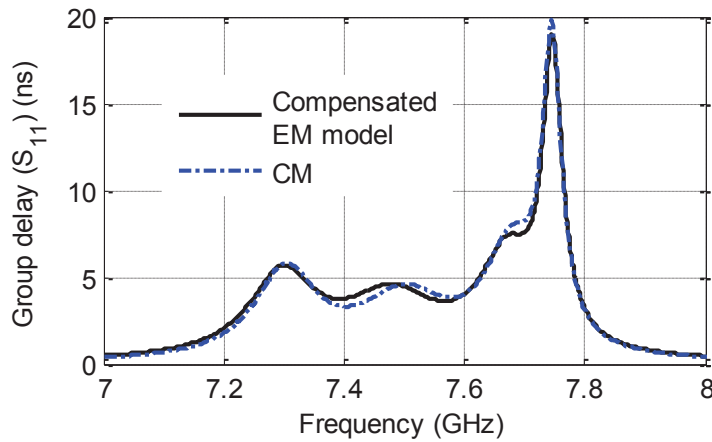
(a)
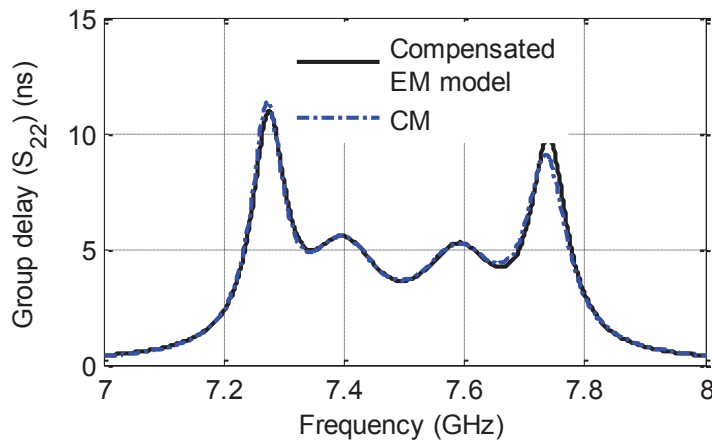
(b)

Figure 5-9. **Group delay of tuned sub-circuits. a) Sub-circuit 1. b) Sub-circuit 2.**

$$b = -2\Delta l \sqrt{\mu \varepsilon}$$ (5-6)

where Δl is the length of the input line. Using (5-6), b is calculated at -0.1393 ns, which is different from the extracted value because the effective length of the line is different from the physical length. Although the difference between the simulated and corrected delay response may look very small, this step is crucial in the optimization method that we are proposing in this chapter, and failing to do so will result in incorrectly extracted coupling parameters.

The corrected group delay response is used in the coarse model as the goal function to extract the equivalent couplings and cavities' resonant frequencies. We assumed a linear mapping existed between the parameters of the EM and CM model. The vector x_f contains the parameters of the fine model (Sub-circuit 1), and x_c is the vector that has the information of the coarse model. The vector x_c^* is an ideal coupling vector that has the information about the desired couplings between Cavities 1 to 4 and their resonant frequencies along with the input resistance (R_1). In the first step, the initial dimensions are preserved in ($x_f^{(n=1)}$). In the following step, the CM is optimized to have the same compensated group delay response of the EM model. The error function should have the form:

$$err = \sum_j \left(\tau S_{11}'(f_j) - \tau S_{11}^c(f_j) \right)^2$$ (5-7)

in which $\tau S_{11}'$ is the compensated delay response of EM model and τS_{11}^c is the delay response of the CM. Theoretically, the frequency span only needs to cover the passband of the filter but as in the first step the cavities are resonating at arbitrary frequencies, it is required to use a much wider frequency span. It is necessary to use a global optimization method such as Particle Swarm Optimization (PSO) [22] for the initial step. The achieved parameters are saved in $x_c^{(n=1)}$. Then:

$$f = x_c^* - x_c^{(n)}$$ (5-8)

$$\Delta d = f \cdot d \tag{5-9}$$

where d is the mapping vector and Δd is the dot product of f and d. The new dimensions are calculated by:

$$x_f^{(n+1)} = \Delta d + x_f^{(n)} \tag{5-10}$$
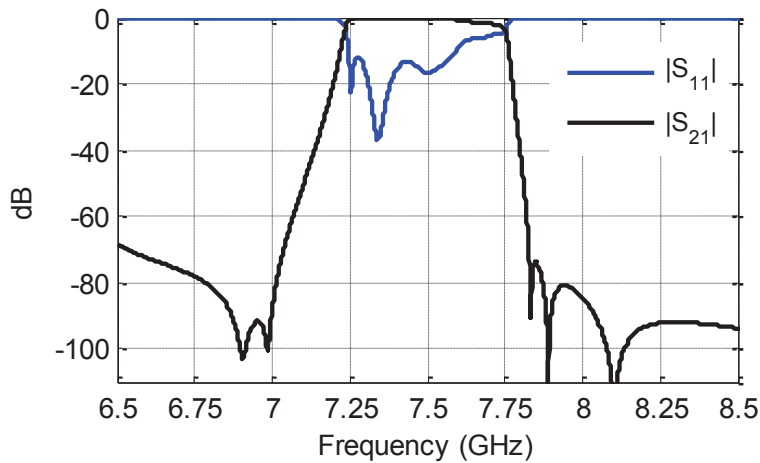
Figure 5-10. Simulated S_{11} and S_{21} of the structure after the first step of the optimization using group delay response and space mapping.

The process continues until reaching to a response close the EM model and tuned CM as in Figure 5-9(a). The same procedure is repeated for Sub-circuit 2 (Figure 5-4(b)) in which Cavities 1-4 are de-tuned and dimensions of Cavities 5-8 along with associated couplings and output resistance (R_2) will be optimized. In this case, the delay response of S_{22} is compensated first (Figure 5-7 and Figure 5-8) and then is used. The outcome of this process is shown in Figure 5-9(b). At this step, all the initial dimensions have been calculated. It should be mentioned that the parameter g_{45}, which is the slot's distance from the fourth cavity's wall, is calculated before this step using the curve in Figure 5-3. The final step of the design is done by fine-tuning the parameters using full-wave optimization. As the calculated dimensions are supposed to be very close to the desired values, this step should be fast, and the chance of being trapped in local minima is narrow. For optimization, the flowing error function can be used:
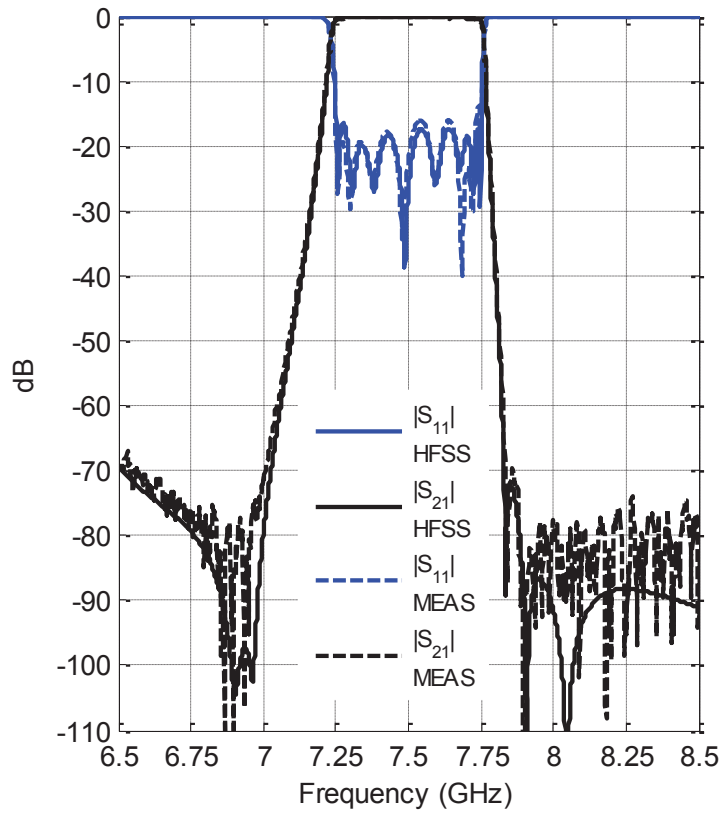
(a)
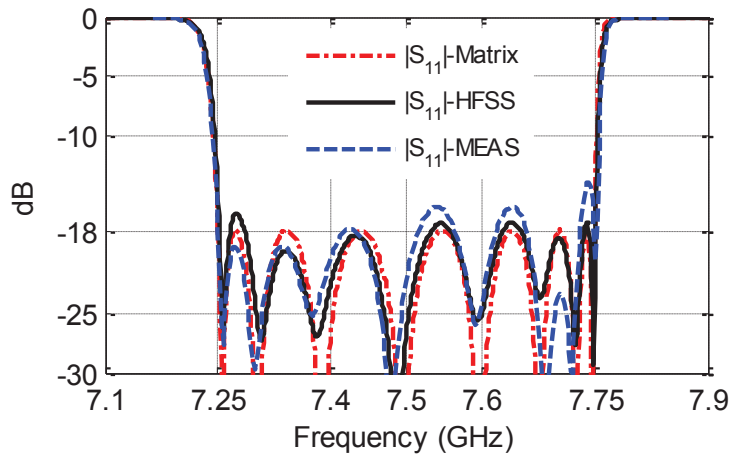
(b)

Figure 5-11. **Response of stacked quadruplet filter in simulation and measurement. (b) Simulated reflection response of the optimized design compared with the theory and measurement.**

$$errf = \sum_{1}^{n} |S_{11}(f_p^i)|^2 + w \sum_{1}^{m} |S_{21}(f_z^i)|^2 + \sum_{1}^{2} (|S_{11}(f_e^i)| - \varepsilon)^2. \qquad (5\text{-}11)$$

where f_p are the pole positions, f_z are the positions of the transmission zeros, f_e are the start and end frequencies of the passband, and ε is the ripple factor. As the rejection is considerably high in both upper and lower stopbands, it is necessary that the terms regarding S_{21} be weighted properly using w. Figure 5-10 shows the response of the filter after the first step of the optimization (space mapping). As it can be seen after the first step, the response is not far away from the desired filter function in Figure 5-2. However; the equi-ripple behavior is not achieved. This comes from the fact that parameter g_{45} is not tuned with the collaboration of other elements. Moreover, the loading effect is not present for Cavity 4 and 5 in Sub-circuit 1 and 2. After the second step of optimization (full-wave), the response is very close to the goal, which is shown in Figure 5-11. Table 5-2 lists the parameters in step 1 and 2. Few parameters remained unchanged during the full-wave optimization and changes in some of them are negligible. Parameters a_4 and a_5 have the biggest change in values, which is anticipated as in the first step they are tuned without the loading effect of the other one.
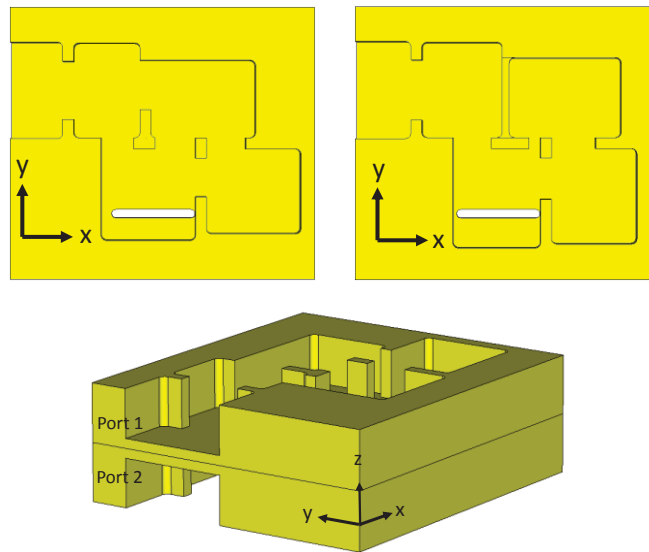
Figure 5-12.   Stacked CQ filter with input and output in the same direction.

The possibility of rotating the upper quadruplet and have both the input and output of the filter in the same direction is possible in this design, which adds to the flexibility of
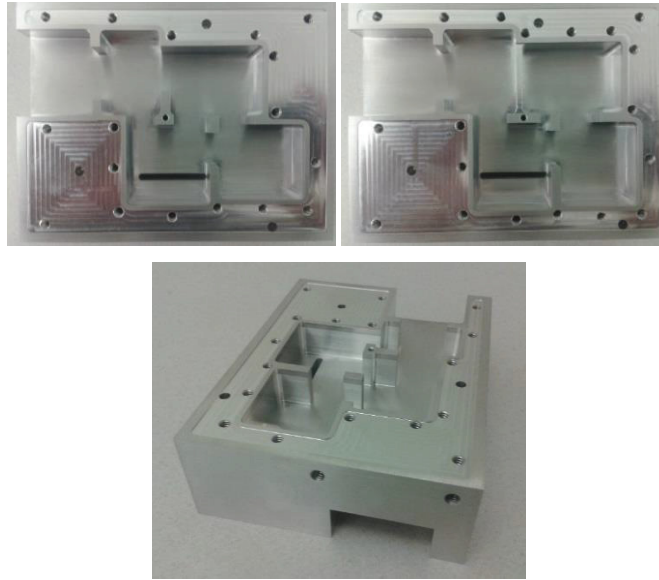
Figure 5-13. **Fabricated model (a) Upper quadruplet. b) Lower quadruplet. (c) Complete structure.**

Table 5-2. **Design parameters in both steps of the optimization.**

Parameter	Step1 (mm)	Step2 (mm)	Parameter	Step1 (mm)	Step2 (mm)
a1	27.89	28	g23	11.57	11.64
a2	22.85	22.89	g24	12.14	12.02
a3	24.98	25.03	g34	11.49	11.4
a4	26.8	27.02	g45	6.3	6.4
a5	29.58	29.2	g56	11.99	12.08
a6	28.17	28	g57	3.46	3.46
a7	23.41	23.5	g58	11.41	11.41
a8	28.02	28	g67	13.1	13.13
gi	17.13	17.09	g78	0.86	0.86
g12	14.55	14.55	go	17.61	17.67
g14	9.61	9.64			

the structure. With some careful investigation on the stacked configuration of Figure 5-1, it can be understood that in this case the results will be identical to the optimized response of the original design. The rotated structure is shown in Figure 5-12.

The fabricated prototype is shown in Figure 5-13. The design was fabricated using a CNC machine. The measured results are in excellent agreement with the simulation

(Figure 5-11). Also in Figure 5-11(b) the measured reflection coefficient is compared with simulation and CM indicating very good agreement. It's worth mentioning that no tuning screws are used for post-fabrication corrections.
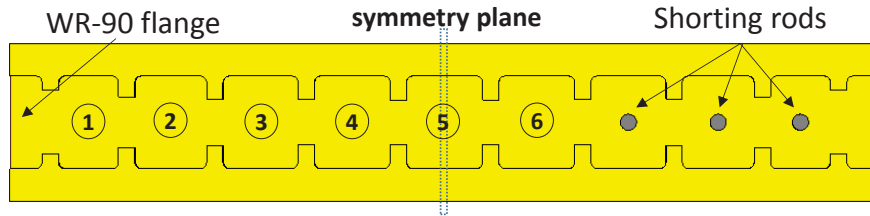
Figure 5-14.   All-pole ninth order bandpass filter sub-circuit in WR90 waveguide.
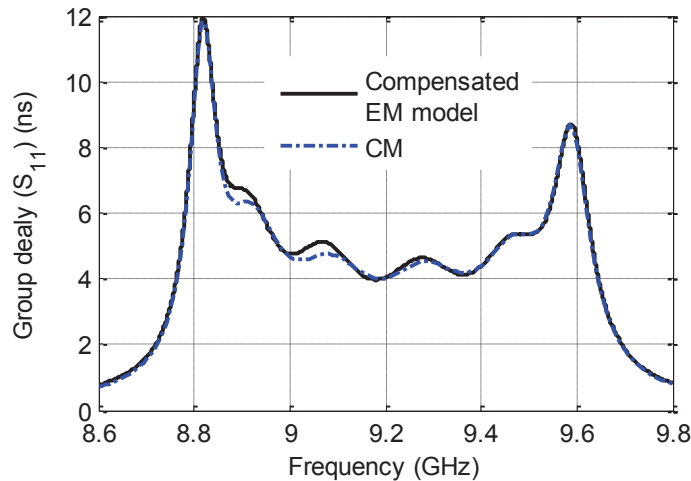
Figure 5-15.   Group delay response of tuned sub-circuits for ninth order all-pole filter.

5.3. Wideband All-Pole Filters

Several methods and closed form formulas can be found in the literature for the design of in-line all-pole filters on rectangular waveguide using irises [25]. The classic methods are based on modeling the coupling discontinuities by a lumped element network and compensate the size of the cavities by the calculated phase loading of every coupling window. Since all the calculations and modeling are being done in the center frequency of the filter, the calculated dimensions will yield accurate results only for narrow-band cases. Therefore, the design of wideband in-line filters mainly depends on full-wave optimization, which can be slow and tedious, especially for high order designs. There have been some

99

approaches in order to improve the calculated dimensions to have a better Chebyshev response as in [51], [52] which are based on using a more complicated model for the actual frequency dependence of the irises and using an iterative process to find the correct dimensions of the irises. One drawback of these methods is that they are unable to take into account the rounded corners of the cavities, which is the inevitable characteristic of CNC machined structures.

Using the proposed method in this chapter, wideband in-line filters can be designed efficiently and without the need for any full-wave optimization. The procedure is explained for both even and odd order filters through the design of a ninth order filter with the 24 dB return loss in 8.8-9.58 GHz, which is equal to approximately 8% fractional bandwidth, and an eighth order filter with a passband in 22.5-27.5 GHz (20% fractional bandwidth). Only one sub-circuit is enough to design any in-line configuration since the geometry is symmetric. Therefore, for the first design, the first five cavities need to be analyzed, and the rest should be de-tuned using shorting pins. However, to mimic the loading effect of Resonator 6 on Resonator 5, it is necessary to bring Cavity 6 in the sub-circuit and optimize its dimension during the process. In the end, the calculated dimension for Cavity 6 will be disregarded and replaced by the optimized length of Cavity 4, since the filter is symmetrical. By doing so, no post full-wave optimization is required after optimizing the dimensions by the group delay method. The geometry of the sub-circuit is shown in Figure 5-14. The thickness of irises is 4 mm. The same procedure is repeated as described in Section 5.2.2 by solving the EM sub-circuit, which contains Cavity 1 to 6 along with de-tuned Cavities 7 to 9 and performing parameter extraction procedure after correcting the phase loading effect. The group delay response of the optimized EM sub-circuit and CM are plotted in Figure 5-15. Later on, the shorting pins are removed, and the dimension of Cavity 6 is replaced by the length of Cavity 4. Then, EM response of the filter is calculated using ANSYS HFSS, which is shown in Figure 5-16. It can be concluded here that the proposed technique for mimicking the loading effect is effective. Therefore, by tuning one extra resonator in a sub-circuit, the full-wave optimization step can be avoided completely. Another conclusion is that the loading effect on a resonator is a function of the resonant frequency of the adjacent cavity rather than its physical dimensions. Therefore, in the sub-circuit of Figure 5-14, although the length of Resonator 4 is different from the real case since it is resonating at f_0, it is mimicking the correct loading.

100
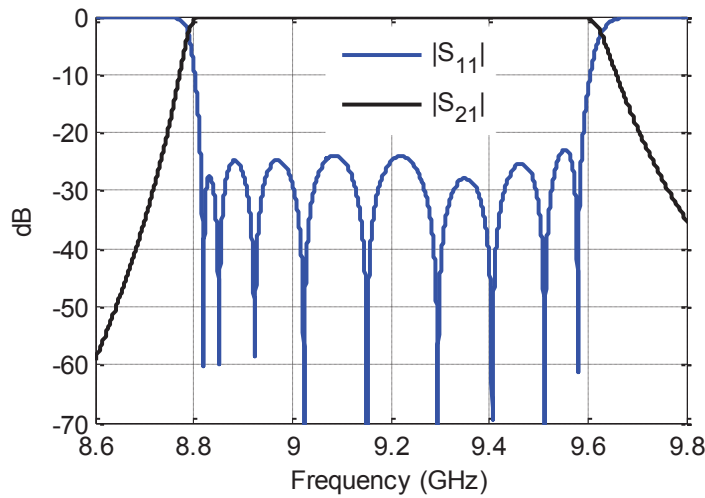
Figure 5-16.   Simulated response of ninth order all-pole filter.

We tested the method on an even order all-pole filter with extremely higher bandwidth. Figure 5-17 shows the sub-circuit of an eighth order filter with the 20 dB return loss in 22.5-27.5 GHz, which is equal to approximately 20% of fractional bandwidth. Similar to the previous example, one additional cavity is solved during the optimization. By having Cavity 5 in the circuit, the dimension of the iris in the middle responsible for coupling M_{45} will be optimized and also the loading effect on Cavity 4 is considered. Therefore, accurate dimensions can be calculated, and no further full-wave optimization is required. The delay response from the compensated EM model and CM are plotted in Figure 5-18. Similarly, at the end of the optimization process of the group delay, the length of Cavity 4 is used for Cavity 5, due to the symmetry of the structure. The simulated response of the complete structure is shown in Figure 5-19. Some discrepancy in the ripple is present as the bandwidth of the filter is considerably wide. To summarize the method, a flow chart is provided in Figure 5-20 that explains the procedures to design passband filters using group delay method. Note that in the chart, M^* is the goal CM of the sub-circuit and M is the extracted CM of the compensated EM model. Regarding the value of δ, the appropriate marginal error should be selected based on the order of the filter and the bandwidth. A graphical comparison between the calculated GD response of the EM model and that of the goal CM model can help to choose the correct δ.

101
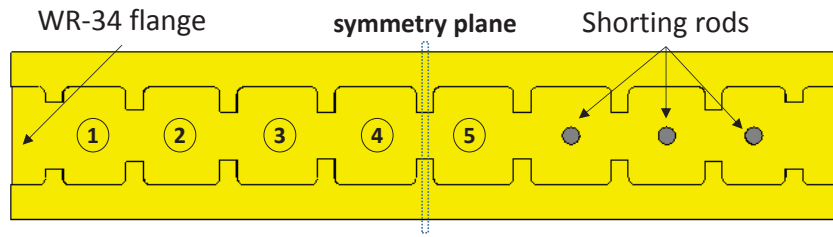
Figure 5-17.   All-pole eighth order bandpass filter sub-circuit.
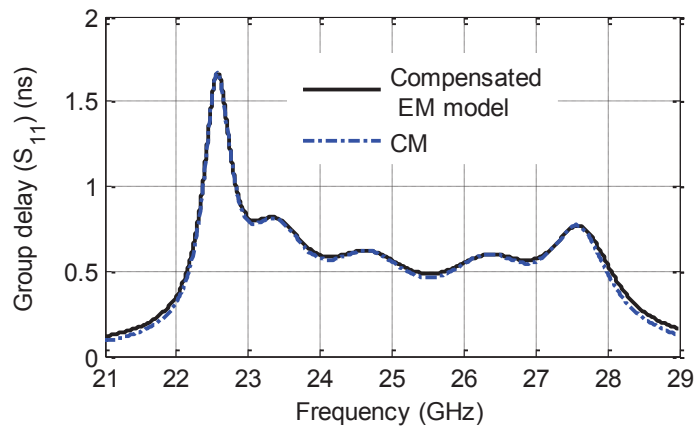
Figure 5-18.   Group delay response of tuned sub-circuits for eighth order all-pole filter.
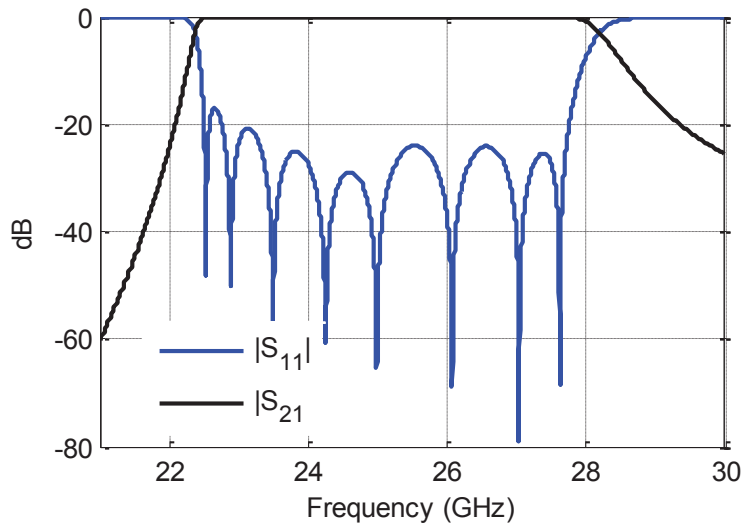
Figure 5-19.   Simulated response of eighth order all-pole filter.
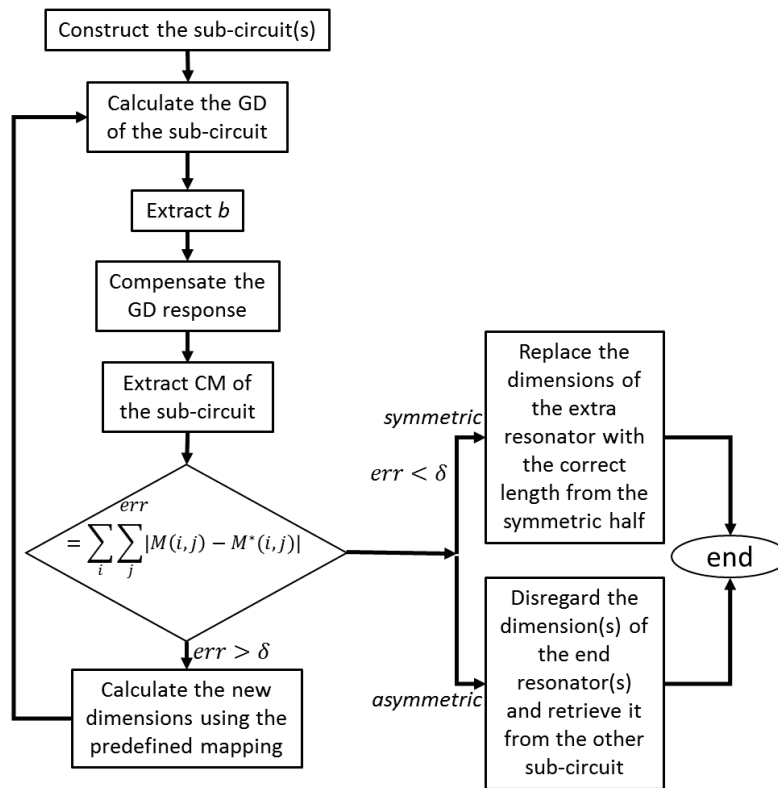
Figure 5-20. Flow chart for the design of in-line bandpass filters based on GD method.

5.4. Design of Wideband Diplexers

Converting the lumped element model of a diplexer to the physical dimensions is considered a challenging task since it is mainly based on full-wave optimization and post fabrication tuning. For narrow-band cases, there are analytical approaches to minimize the use of full-wave optimizations [53], [54]. In [55], a procedure was proposed to design the CM of the diplexers by modeling the junction of the two channel filters as a complex load. Then the designed CM was implemented for a diplexer with fifth order channels with 5% bandwidths using full-wave optimization. Another approach was used in [56] again to design the CM of diplexers. The proposed methodology was tested for a forth order rectangular waveguide diplexer with forth order channels with 1.3 % bandwidth by a full-wave optimization process which wasn't described in detail. One interesting approach to convert the CM of a diplexer to physical dimensions is by extracting the CM from the simulated or measured S-parameters as proposed in [57]. Such a procedure can be very

efficient for diplexers with narrow to moderate bandwidth channels if the rotation sequence for reducing the CM to the correct geometry is available. However, there is no standard procedure to calculate such a pivotal rotation sequence and angles for a general case, and it can be tough for complex topologies. The complexity of the task becomes more severe when dealing with the wideband case, high-order channels where the dispersive behavior of the irises should be taken into account. There have been methods to facilitate the full-wave optimization of wideband diplexers as in [51] where an approach is used to limit the number of the parameters during the full-wave optimization of wideband diplexers. Another method that was reported in [58] is proposed for designing multiplexers by using space mapping when the coarse model is CM representation of the channel filters. Such a procedure can be applied on a diplexer too. However, for wide-band, high order channel filters extracting the CM is troublesome due to existing of extra TZs that the CM does not predict.

As discussed above, the majority of the discussions in the literature on the design of the diplexers is focused on the calculation of the lumped or CM model of them while the physical dimensions are calculated by full-wave optimization or post fabrication tuning based on the calculated model. Even for narrowband cases, such an optimization routine can be expensive and tedious and mainly dependent on the initial points. As a matter of fact, the lumped model of diplexers can be calculated efficiently using optimization since the lumped model can be solved fast by using correct initial values.
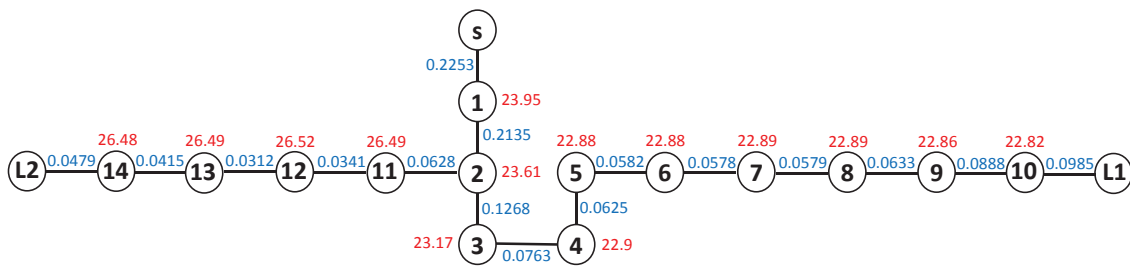
Figure 5-21.   Coupling diagram of the diplexer. Resonant frequencies are in GHz. The true un-normalized couplings (k) are provided.

The group delay method can be used to design wideband, high-order diplexers by dividing the structures to three sub-circuits and using space mapping. Here, a diplexer with wideband channels is designed. The first channel covers 21.8-24.2 GHz, and

Channel 2 covers 25.9-27.1 GHz with 20 dB return loss. The coupling diagram of the diplexer is shown in Figure 5-21 along with the couplings and the resonant frequency of the nodes. In order to avoid any ambiguity regarding the fractional bandwidth of the CM, the un-normalized couplings (k) and actual resonant frequencies (in GHz) are provided in the graph. The coupling diagram is designed by an optimization procedure outlined in [42]. Although the CM model is solved very fast, with the enormous number of the unknowns, it is important to start the optimization with the correct initial values. The coupling matrix of Chebyshev filter for each channel is used as the initial point to facilitate the speed. For the input coupling of the diplexer (source to Resonator 1), the normalized coupling of M=1 is used as the initial value. Also, Resonator 1 and Resonator 2 are set to the center frequency of the diplexer, calculated by:

$$f_0 = \sqrt{f_{l1}f_{u2}} \qquad\qquad (\text{5-12})$$

where f_{l1} is the lower frequency of Channel 1 (21.8 GHz) and f_{u2} is the upper frequency of Channel 2 (27.1 GHz). By considering the outlined guidelines, the CM of the diplexer is calculated efficiently. Our goal is to convert the network elements in Figure 5-21 to physical dimensions using the group delay method. To do so, the structure is divided into three sub-circuits. In Sub-circuit 1, the common input port is excited, and all the resonators except the last one in every channel are in the circuit. The last cavities of both channels are de-tuned using shorting pins in the middle. This is shown in Figure 5-22(a). Even though Resonator 9 and Resonator 13 are being optimized during the process, their optimized dimensions will be disregarded as they only exist in Sub-circuit 1 to mimic the loading effect on Resonator 8 and 12. The group delay of S_{11} is calculated using ANSYS HFSS and after performing a phase removal process, the associated resonant frequencies and coupling parameters of Sub-circuit 1 are extracted from it using the CM model. Space mapping is applied to find the updated values for each dimension by comparing them to the goal coupling parameters using (5-8) to (5-10). The process continues until reaching a response close to the EM and optimized CM. This is shown in Figure 5-23(a). At this step, the dimensions of Resonators 1 to 8 and 11 to 12 along with iris dimensions associated with them and the input iris size are calculated.

105
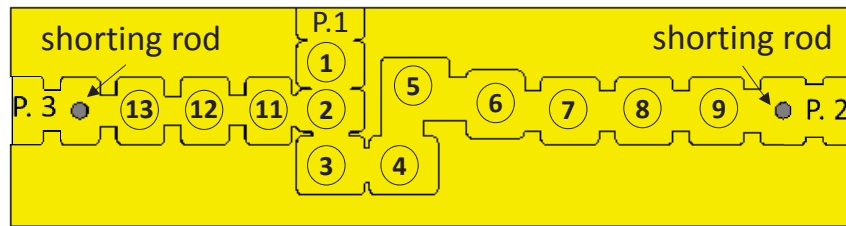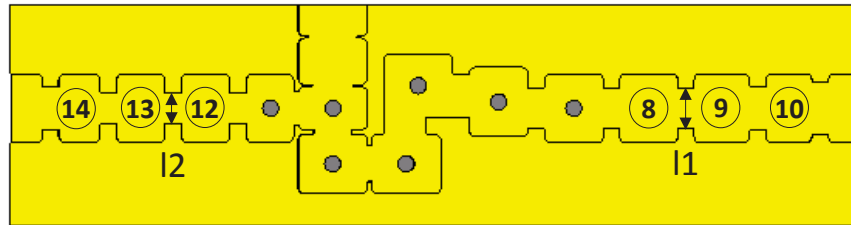
Figure 5-22. Wideband diplexer on WR34. a) Sub-circuit 1, b) Sub-circuit 2 and 3.

In Sub-circuit 2 (Figure 5-22(b)) output of Channel 1 is excited, and only the last three resonators of channel 1 are in the circuit. The rest of resonators are detuned, and the ones that are far away can be removed from the model to increase the speed. Continuing the same procedure outlined for Sub-circuit 1, it is important to mention that Resonator 8 only exists in the Sub-circuit 2 to create the loading effect on Resonator 9 and its dimension will be disregarded because it has already been calculated using Sub-circuit 1. The delay response of the optimized Sub-circuit 2 (S_{22}) compared with the response from the goal CM model is plotted in Figure 5-23(b). The same procedure is used on Sub-circuit 3 and outcome of it is plotted in Figure 5-23(c). As shown in Figure 5-22(b), Sub-circuits 2 and 3 can be combined and solved at the same time because the de-tuned cavities in the middle remove any coupling between them. Therefore, the delay response of S_{22} and S_{33} can be considered independent of each other.

At this step, all of the dimensions are calculated. It is important to notice that parameters *l1* and *l2,* as defined in Figure 5-22(b), are calculated through Sub-circuit 1 and also by Sub-circuit 2 and 3. The parameter *l1* is responsible for the coupling between Resonators 8 and 9, and *l2* controls the coupling of Resonators 12 and 13. If the procedure explained above is done correctly, the optimized values for *l1* and *l3*, which are obtained using Sub-circuit 1, should be equal or very close to the calculated values from Sub-circuit
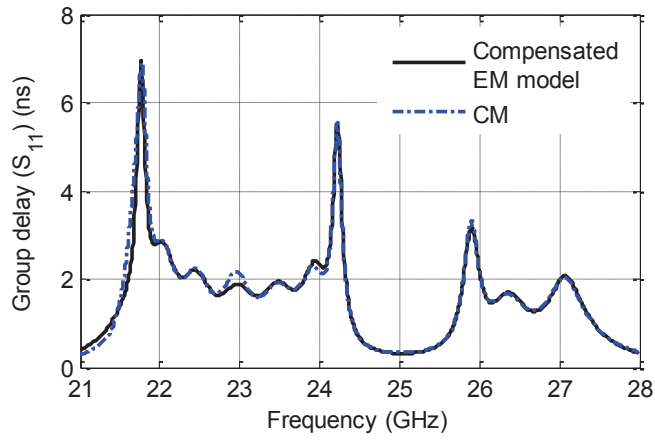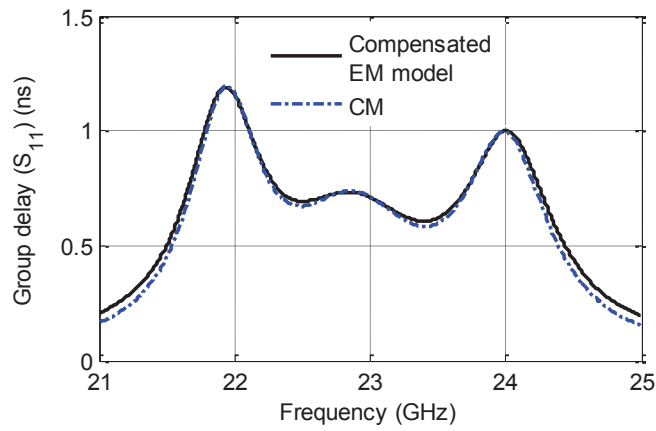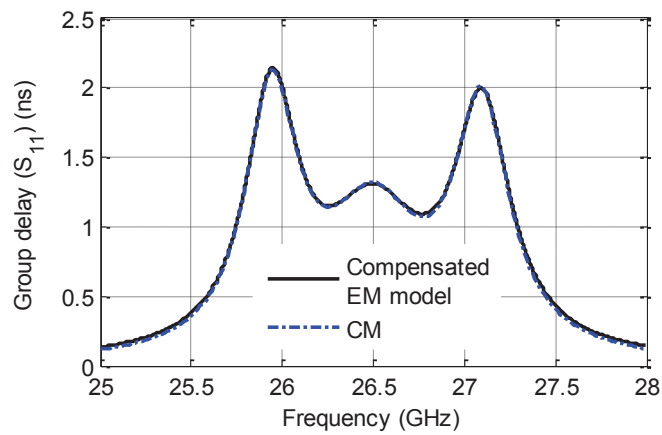
Figure 5-23. Optimized group delay responses of the diplexer. a) Sub-circuit 1, b) Sub-circuit 2, c) Sub-circuit 3.
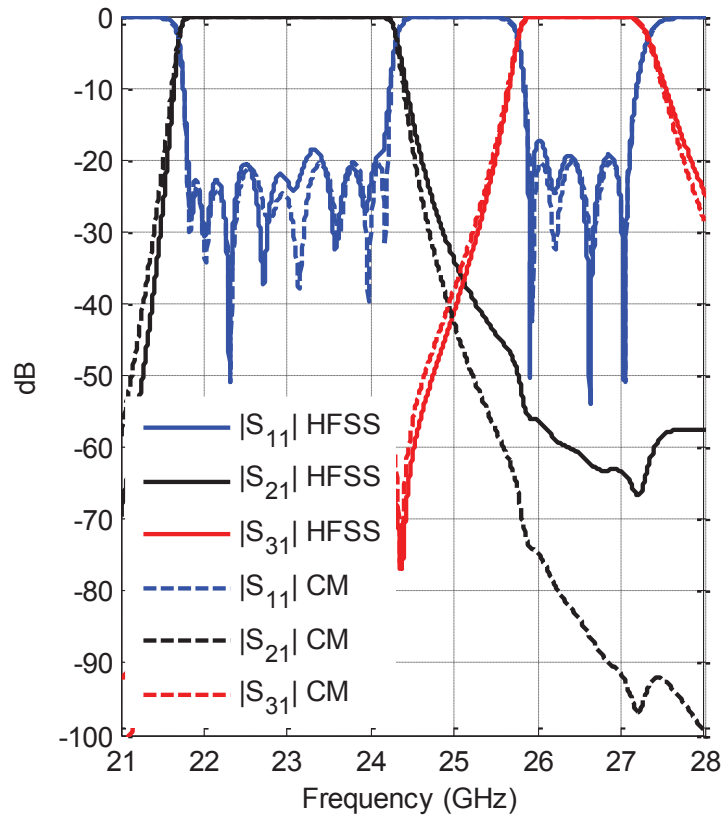
Figure 5-24.   Simulated response of the diplexer compared to coupling matrix.

2 (for *I1*) and Sub-circuit 3 (for *I3*). The simulated EM response of the model compared with lumped element model is plotted in Figure 5-24, which shows an excellent agreement considering no full-wave optimization has been performed. The total bandwidth of the diplexer is approximately 21.8% which can encompass the majority of applications. The flow chart in Figure 5-20 can be used to design the diplexer. However, it should be repeated for all three sub-circuits because there is no symmetry in the structure anymore. Consequently, the GD response of each sub-circuit should be corrected independently using the procedure outlined in Section 5.2.2.

5.5. Conclusion

A novel methodology has been proposed for deriving the physical dimensions of bandpass filters and diplexers from the pre-designed coupling matrix for wideband, large-

scale designs. The method has been based on dividing the structure into many sub-circuits and calculating the delay response of each sub-circuit using a full-wave EM software. The coupling parameters of each sub-circuit have been extracted from the delay response. Using a simple linear mapping, the physical dimensions have been calculated gradually using an iterative process.

Normally, for wideband filters, the design has been based on full-wave optimization, which is a tedious and slow process, especially for high-order and large-scale structures. Many structures can be designed without any use of full-wave optimization in EM level using the proposed method. For some cases, the fine-tuning of the design has been done using a local gradient optimizer, which converges very fast. Therefore, we have eliminated the use of global optimization.

The proposed method is applicable to a variety of designs providing that the coupling matrix of the filter be available. Also, the physical model details such as rounded corners are taken into account during the optimization. We tested the method on a novel geometry of a cascaded quadruplet filter with many cross-couplings and high complexity with 6.7% fractional bandwidth. A ninth order all-pole filter with 8% bandwidth and an extremely wideband eighth order filter have been designed without using any full-wave optimization. To show the capacity of the method, it has been used to design a wideband, high order k-band diplexer. The conversion of the coupling matrix of the diplexer to the physical dimensions has been carried out efficiently without using any full-wave optimization. The total fractional bandwidth of the diplexer is around 22%. It should be mentioned that here, we used the simplest form of mapping and still the responses are converged fast and efficiently. By using aggressive space mapping [59] which benefits from a non-linear and more complex form of mapping, the convergence of the responses can be improved even further.

Chapter 6.

Design of Integrated Diplexer-Power Divider Using Gap Waveguide Technology

6.1. Introduction

Diplexers and power dividers are two important and integral part of many communication systems. Several geometries and design procedures are introduced to improve their functionality in terms of size reduction, insertion loss, and rejection. As the design and implementation of the diplexers are more involved, considerable resources can be found in the literature [51], [53], [54], [56], [60], [61]. One novel geometry that contributes to the performance and size reduction of the system is integrating the power divider inside the diplexer to be common with the antenna array's corporate feed. In this chapter, we propose all-pole coupled-resonator diplexer-power divider. We introduce a systematic design procedure. In order to achieve this, a novel optimization technique is used. The optimized lumped element network is implemented on ridge gap waveguide technology in order to benefit from the contactless fabrication features. Finally, the integrated diplexer-power divider is used in a large-scale 16×16 antenna array which is designed in the same RGW technology.

In Section 6.2, a new error function is introduced to design the coupling matrix of the diplexer-power divider network. Also, a general recipe is explained to ensure the convergence of the optimization procedure. The proposed error function removes the coupling between the two power divider output ports and simultaneously design the channel filters correctly based on an equi-ripple performance. The method is tested on a seventh order channel diplexer successfully. In the final section of this chapter, the optimized CM of the seventh order channel diplexer-power divider is implemented on a guiding structure. Converting the lumped element model of a diplexer to the physical dimensions is generally considered a difficult task since it is mainly based on optimization procedures. In Chapter 5 a method was introduced to design bandpass filters and diplexers using the corrected delay response of the sub-circuits. We used this method with

some modifications in order to convert the CM model of diplexer-power divider to the physical dimensions of the structure without using any full-wave optimization. This was done successfully using ridge gap and groove gap waveguide technology. The simulated response of the diplexer-power divider agrees very well with CM model. The proposed device is integrated easily with the corporate feed of the antenna array. The proposed technique allows for the design of a high-performance module that incorporate the diplexer with the radiating elements efficiently with almost similar size to the antenna. The proposed diplexer-power divider is integrated with the previously designed 16×16 antenna array in order to realize a compact novel diplexer-antenna array based on RGW technology. The antenna array and feeding network have been developed at Chalmers University of Technology, Sweden, by the Division of Antenna Systems, Department of Signal and Systems as a collaborative project. This is investigated in Section 6.4.

6.2. Geometry and Design of Diplexer-Power Divider

The coupling diagram of an integrated seventh order channel diplexer-power divider is shown in Figure 6-1. Every channel filter is composed of seven resonators intercoupled to each other. Two channels are combined using a distributing node (Resonator 0). The distributing node is coupled to two outputs which represent the power divider. It is required for the power to be divided equally in the outputs of the circuit. Thus, output couplings are equal in port 3 and 4 that is shown with R_o. In order to calculate the coupling values and the resonant frequency of the nodes, one can use the optimization routine outlined in [42]. In that case, an error function should be constructed to enforce the position of poles and zeros of the system along with the passband edges and the ripple of Chebyshev function. This procedure yields correct CM in case of traditional diplexers as shown in [62]. Here, the integration of the diplexer with the power divider creates a spurious coupling between Port 3 and Port 4 through Resonator 0. This unwanted resonance has a severe adverse effect on the isolation of channels and has to be removed from the response of the system. Therefore, the pole in S_{33} should be eliminated. This can be done by enforcing a transmission zero in S_{43} at the center frequency of the diplexer which can be achieved by adding an extra term to the conventional error function as follows:

$$errf = \sum_{1}^{n1} |S_{11}(f_p^i)|^2 + \sum_{1}^{2} (|S_{11}(f_e^i)| - \varepsilon)^2$$

$$+ \sum_{n1+1}^{n2} |S_{22}(f_p^i)|^2 + \sum_{3}^{4} (|S_{22}(f_e^i)| - \varepsilon)^2 + |S_{43}(f_c)|^2$$

(6-1)

where f_p are the poles positions, f_e are the start and end frequencies of the passbands, and ε is the ripple factor. The center frequency of the diplexer (f_c) is defined by:

$$f_c = \sqrt{f_e^1 f_e^4}$$

(6-2)

The configuration in Figure 6-1 normally is unable to create any transmission zero at finite frequencies. Therefore, the term regarding them is absent in the error function. The poles f_p^1 to f_p^{n1} represent the poles of the filter in Channel 1 and the f_p^{n1+1} to f_p^{n2} are the poles of Channel 2 filter. Also, f_e^1 and f_e^2 are the passband edge frequencies of Channel 1. In the same way, f_e^3 and f_e^4 represent the passband of Channel 2. It's important to note that even though the CM model is solved very fast since the number of the unknowns is huge, it is important to start the optimization with the correct initial values. Thus, the coupling matrix of Chebyshev filter for each channel is used as the starting point. For the output coupling of the diplexer (Port 3 and 4 to Resonator 0), the normalized coupling of M=1 is used as the initial value. Also, Resonator 0 is set to the center frequency of the diplexer (f_c).
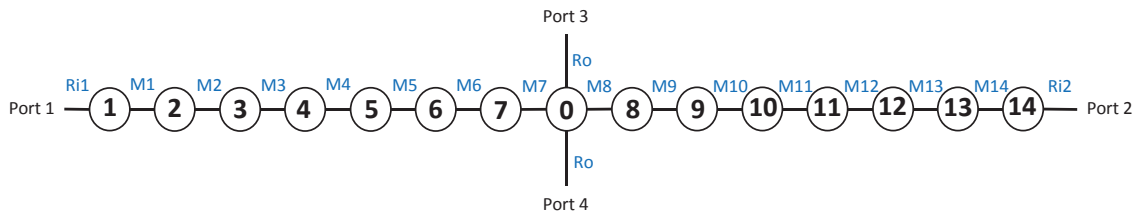
Figure 6-1.   Coupling diagram of a seventh order channel integrated diplexer-power divider.

Here, it is intended to have channels with center frequencies at 28.2068 GHz and 29.2148 GHz with 650 MHz bandwidths with 20 dB return loss. Using the error function in
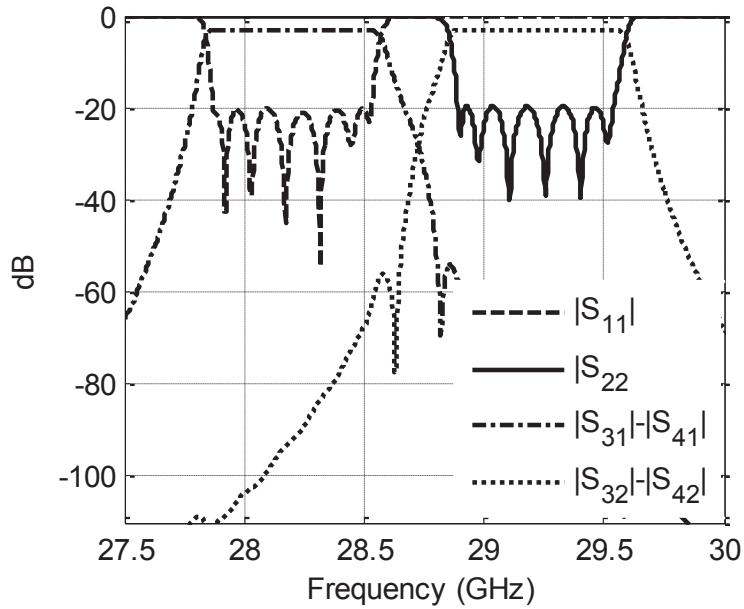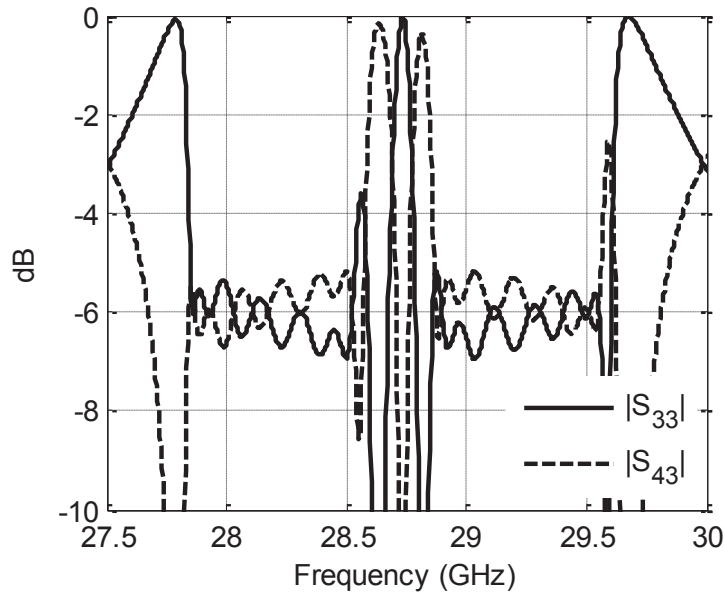
Figure 6-2. Response of the optimized CM of the integrated diplexer-power divider.

(6-1) and considering the aforementioned guidelines, the coupling values and resonant frequencies of the diagram of Figure 6-1 are calculated. The response of the CM is plotted in (a). Using the improved error function in (6-1), no spurious pole is present in the middle of the band. The plotted magnitude of S_{33} and S_{43} also confirm this fact by showing a zero

at the exact same frequency (b). If the optimization of the CM were done using conventional methods, a strong resonance would appear at f_c that has an adverse effect on the isolation between the channels.

6.3. Realization of the Integrated Diplexer-Power Divider in Ridge Gap Waveguide

The optimized CM of the diagram in Figure 6-1 is to be realized using gap waveguide technology. The geometry is shown in Figure 6-3.
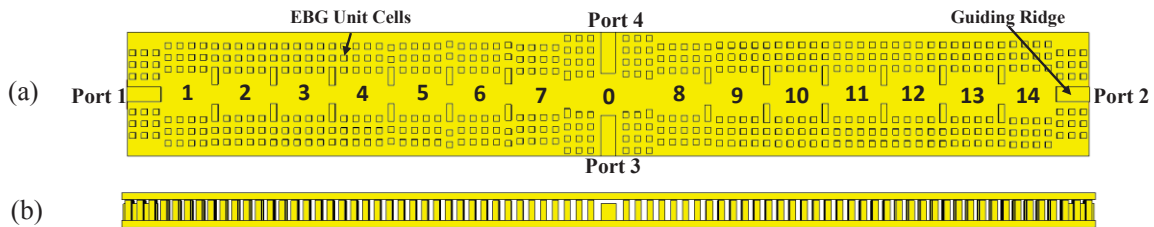
Figure 6-3. Integrated diplexer-power divider using gap waveguide technology. a) top view without the upper lid, b) side view.

The gap waveguide generally is known as a computationally expensive structure. Therefore, the realization of the CM on the structure in Figure 6-3 should be done by an efficient and fast procedure without using any full-wave optimization. Here, we used the delay response of the sub-circuits and space mapping to convert the diagram of Figure 6-1 into cavity and iris dimensions of Figure 6-3. This method was introduced in Chapter 5 for bandpass filters and diplexers, but with some modification, it is adaptable for the proposed diplexers-power divider as well. The structure is divided into three sub-circuits, which are excited at Port 1, 2 and 3 separately. The group delay response of S_{11}, S_{22} and S_{43} is used to extract the CM parameters of each sub-circuit individually. Later, using a linear mapping, the correct dimensions are calculated in an iterative procedure. CST Microwave Studio is used for all EM simulations.

Figure 6-4 shows Sub-circuit 1 in which the structure is excited at Port 3 and Resonators 0, 5-7 and 8-10 are in the circuits while the rest of them are detuned using shorting pins. In order to calculate accurate phase Information, a transition from ridge

114

waveguide to ridge gap waveguide is used in the sub-circuit. This comes from the issues regarding defining a simulation port in CST for ridge gap waveguide. The effect of the transition will be removed by the procedure outlined in Section 5.2.2 using (5-2) to (5-5). All the information about the resonant frequencies and couplings of the elements in Sub-circuit 1 can be extracted from group delay of S_{34}. Figure 6-5 shows the delay response of S_{34} of Sub-circuit 1 after and before phase removal procedure. As can be seen, this step is crucial in order to extract the correct couplings of the sub-circuit.
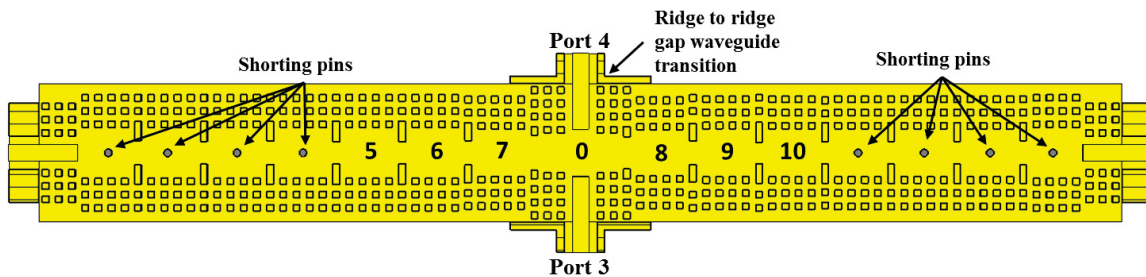
Figure 6-4.   Sub-circuit 1 of the integrated diplexer-power divider.
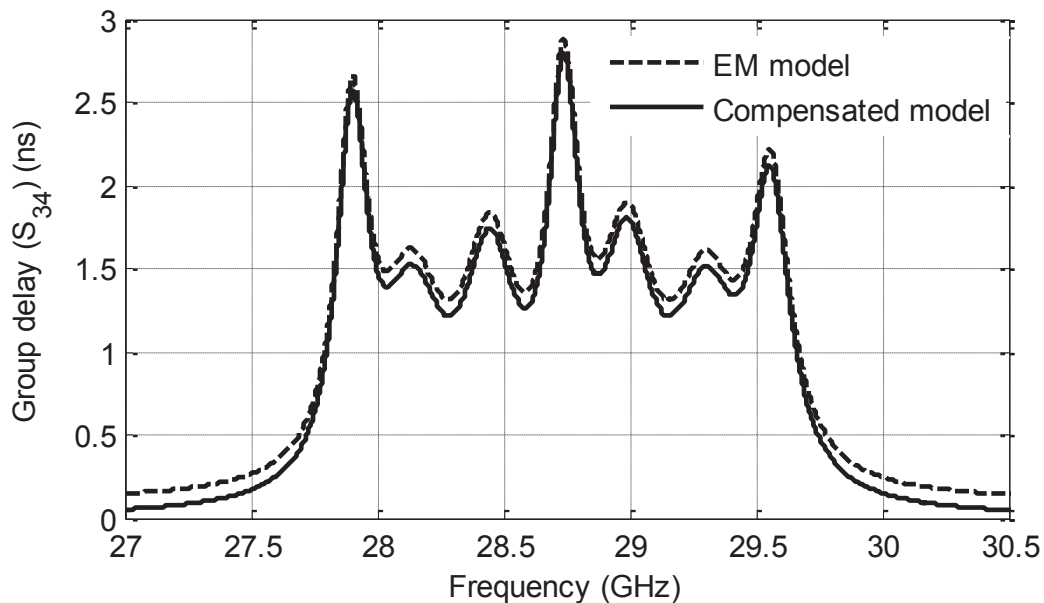
Figure 6-5.   Simulated delay response of Sub-circuit 1 after and before phase removal procedure.

By performing an iterative space mapping procedure using (5-7) to (5-10), all the cavity sizes and the iris dimensions are extracted. Also, the length of input ridges from Port 3 and Port 4 that extrudes to Cavity 0 is calculated. This length reflects the value of

115

output coupling (R_o). The outcome of the optimization procedure is shown in Figure 6-6 by presenting the compensated delay response of EM model and the response from the coupling matrix.
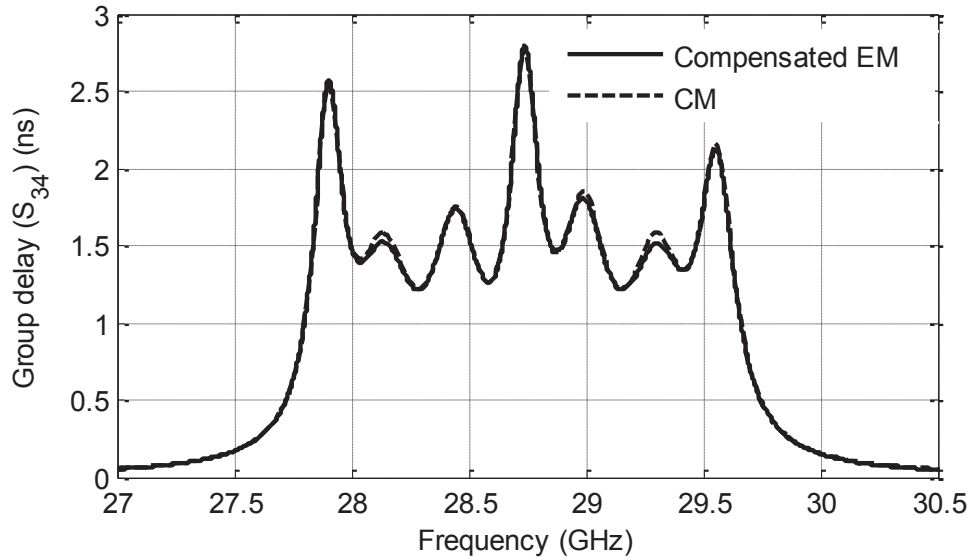
Figure 6-6.   Delay response of the optimized Sub-circuit 1 and the coupling matrix.

Similar to sub-circuits developed in Chapter 5, the resonators at the end of channels (Resonator 5 and Resonator 10) are considered in the circuit in order to mimic the loading effect on their adjacent resonators and their calculated dimensions will be disregarded later.
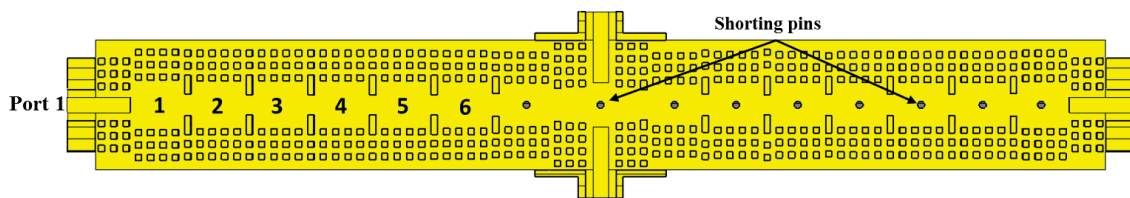
Figure 6-7.   Sub-circuit 2 of the integrated diplexer-power divider.

Sub-circuit 2 is shown in Figure 6-7 which includes Resonators 1 to 6 while the rest of them are detuned. Group delay of reflection from Port 1 is used to optimize the Sub-circuit. By optimizing Sub-circuit 2, dimensions of Resonators 1 to 5 and the iris dimensions incorporated with them will be calculated. It's important to note that Resonator 6 only exists in the circuit to mimic the loading effect on Resonator 5. The dimension for

116

Resonator 5 calculated from Sub-circuit 2 should be replaced by the value from Sub-circuit 1. The outcome of optimization of Sub-circuit 2 is shown in Figure 6-8.
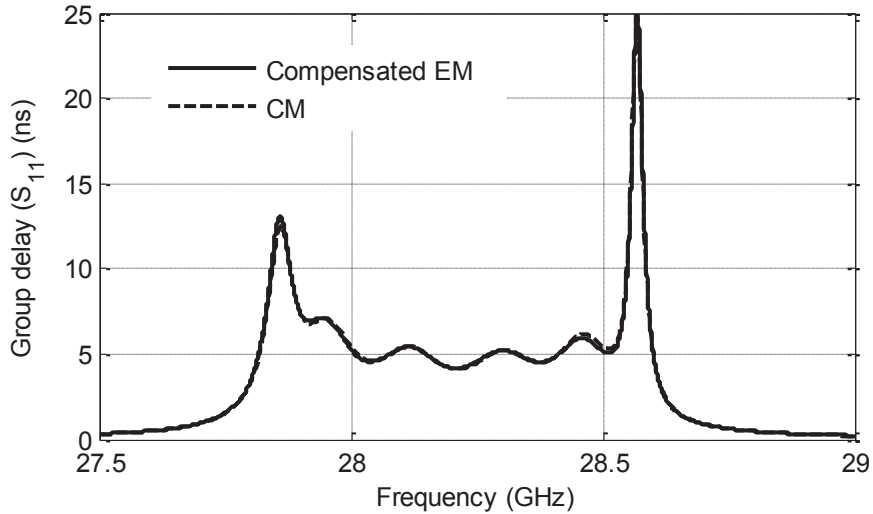
Figure 6-8. **Delay response of the optimized Sub-circuit 2 and the coupling matrix.**

In a similar way, Sub-circuit 3 is generated that is shown in Figure 6-9. Resonators 9 to 14 are included in Sub-circuit 3. After performing the phase removal procedure and an iterative space mapping process, all the dimensions of the Sub-circuit 3 are calculated. The delay response of reflection from Port 2 for the optimized sub-circuits along with the expected response from the coupling matrix is plotted in Figure 6-10 which shows very close behavior. The dimension calculated for resonator 10 is the correct value and should replace the value calculated from Sub-circuit 1. If the outlined procedure is performed correctly, the iris dimension between Resonator 9 and 10 (responsible for coupling M_{10}) that is calculated from Sub-circuit 1 and also from Sub-circuit 3 should be equal or very close. This also applies to the iris between Resonator 5 and 6 (M_5) that is calculated from Sub-circuit 1 and 2.
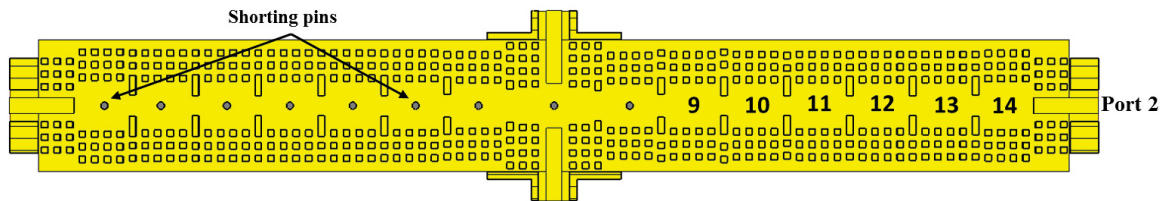
Figure 6-9. **Sub-circuit 3 of the integrated diplexer-power divider.**
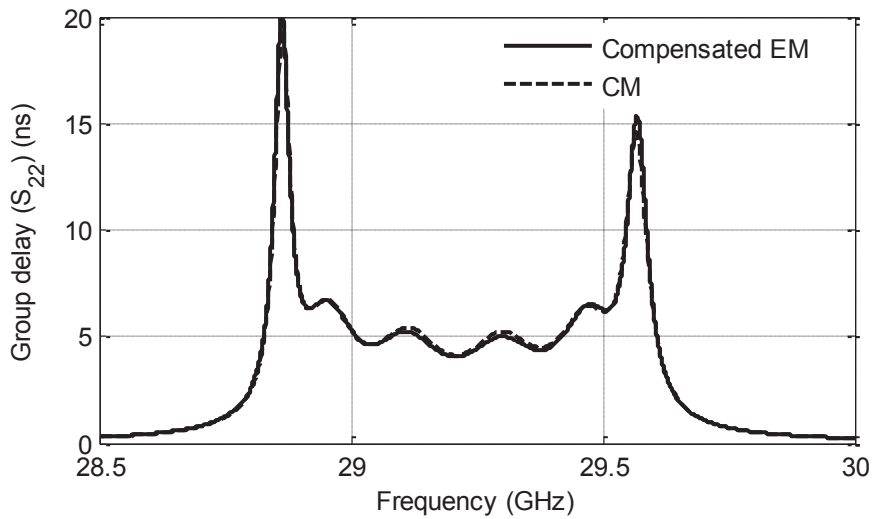
Figure 6-10.   Delay response of the optimized Sub-circuit 3 and the coupling matrix.
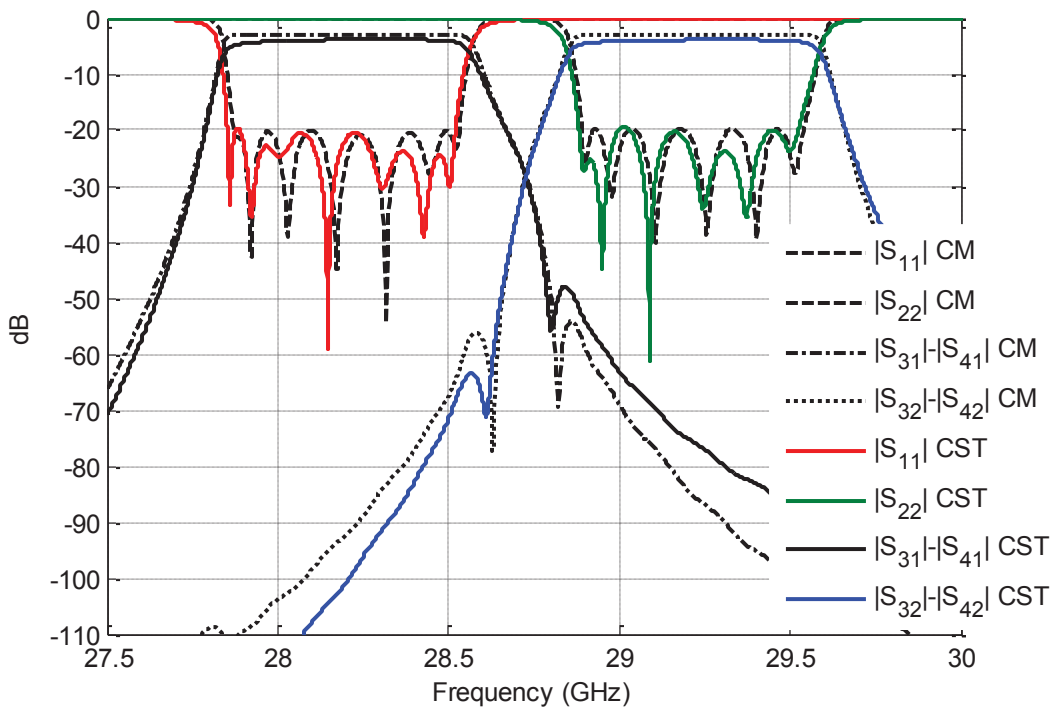
Figure 6-11.   Simulated EM response of the integrated diplexer-power divider.

At this step, all the resonator widths, iris dimensions, and input/output lines are calculated based on the coupling diagram in Figure 6-1. After removing all the shorting rods, the response of the complete diplexer-power divider can be calculated. The

optimized response of the design is shown in Figure 6-11, which shows an excellent agreement with the designed CM model. The focused transmission is provided in Figure 6-12. Ideally, at each output of the power divider, magnitude of $|S_{31}|$, $|S_{41}|$, $|S_{32}|$, and $|S_{42}|$ should be -3 dB since the power is divided equally. However, due to the finite conductivity of the materials, a certain amount of loss is observed. Using Aluminum as the constructing material, a minimum of 0.9 dB insertion loss was noted at the outputs of both channels.
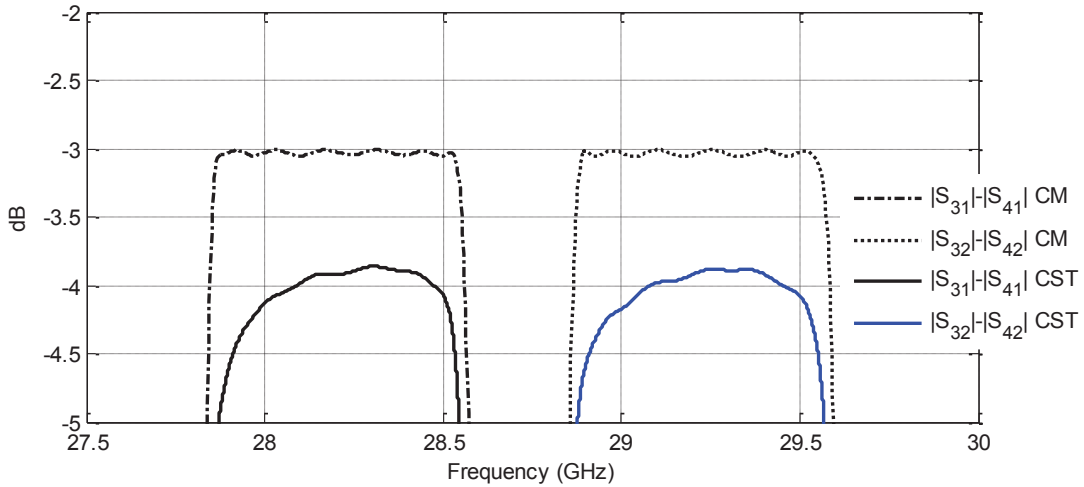
Figure 6-12.   Simulated transmission of the diplexer-power divider compared to CM.

6.4.   Design of Integrated Diplexer-Antenna Array

The designed diplexer-power divider is now incorporated with the corporate-feed of a 16×16 antenna array that is constructed in the same technology. The circuit is placed in the middle of the array and feeds each half of the array equally using the output of the divider. Therefore, a very compact module is achieved that serves as a diplexer and an antenna array at the same time in order to isolate the send and receive signals in a full-duplex communication system. Such a geometry can find application in systems with size restrictions.

The geometry of the corporate feed of the antenna integrated with the diplexer is shown in Figure 6-13. Transition from the WR-28 rectangular waveguide to RGW is used

at Port 1 and 2 of the diplexer. Each output of the diplexer-power divider is connected to one-half of the feeding network. Some of the EBG cells had to be replaced by single big pins since there is not enough space to fit the complete diplexer in the middle of the feed network. The feeding network consists of several bends and quarter wavelength transformers as shown. The design of antenna array and feed network have been done at Chalmers University of Technology, Sweden, by the Division of Antenna Systems, Department of Signal and Systems as a collaborative project. Since the concentration of this thesis is on filter devices, the details of the antenna array won't be discussed here, and instead, it will be briefly reviewed, and some final results will be presented to achieve a better grasp of the principal of the designed diplexer-power divider and its application in the realization of compact integrated diplexer-antenna array modules. More detail regarding the design of antenna arrays using RGW technology can be found in [63], [64].
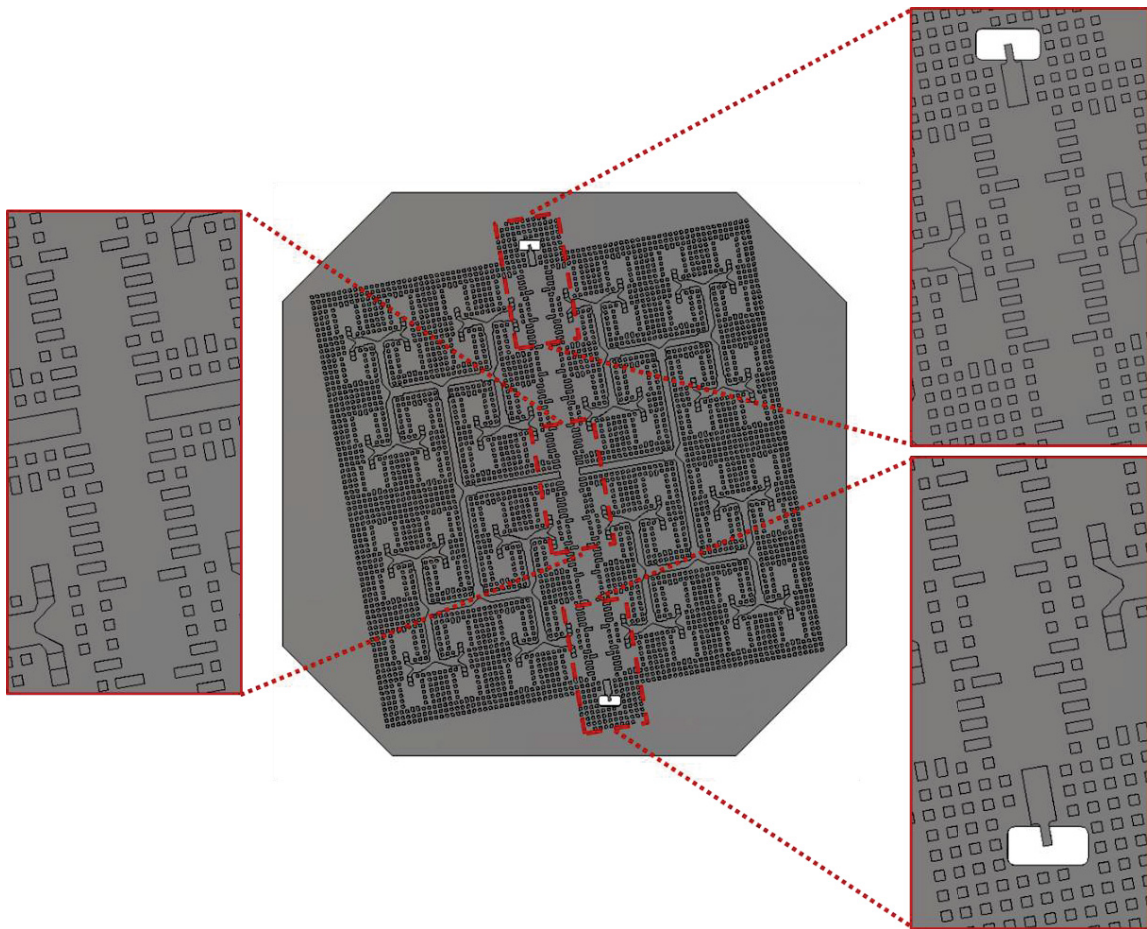
Figure 6-13.   Corporate-feed of a 16×16 antenna array integrated with the diplexer.
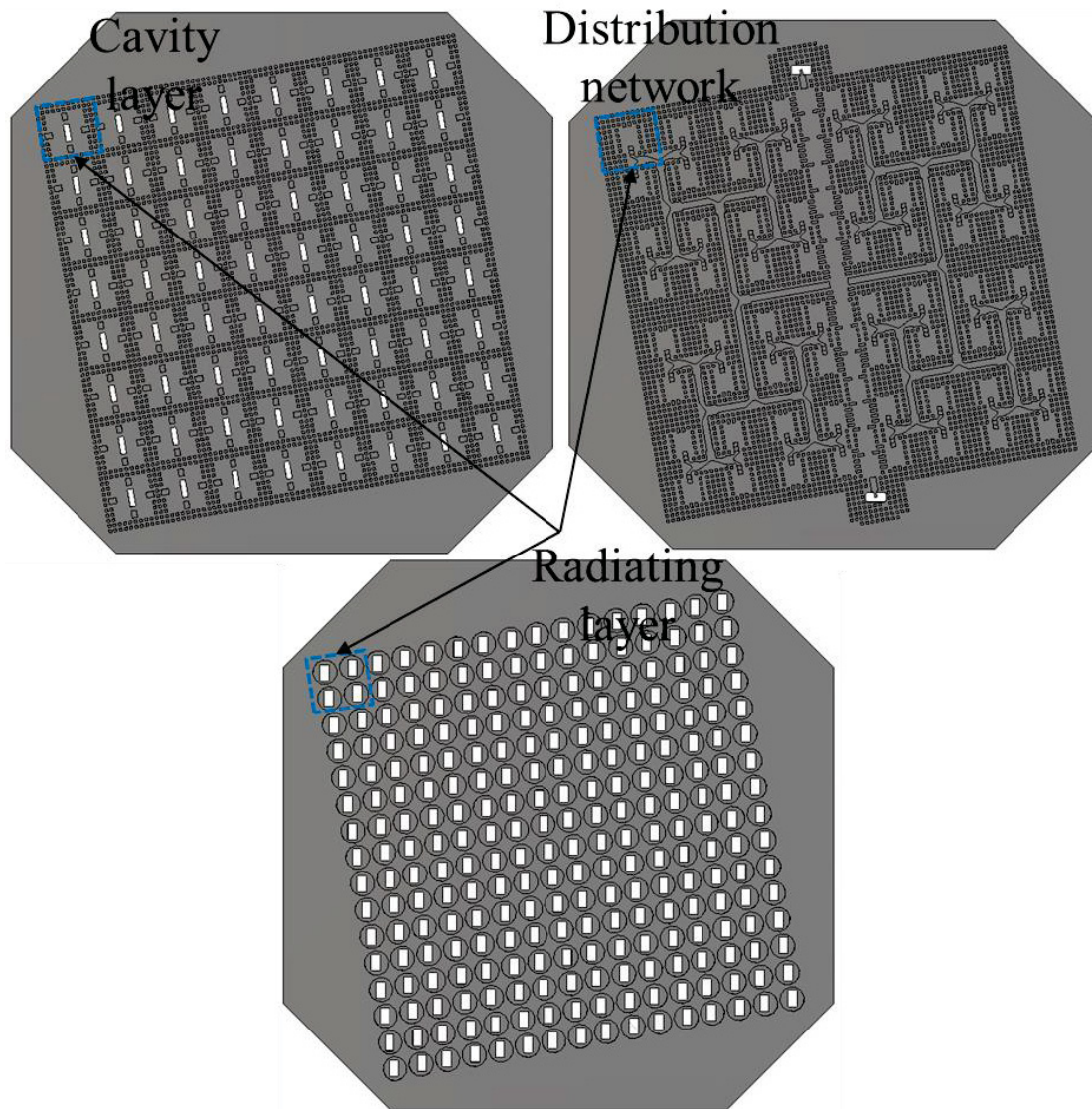
Figure 6-14. **Different layers of the integrated Antenna array-Diplexer.**

The geometry of the module is shown in Figure 6-14. The structure consists of three unconnected layers. Therefore, the structure has a simple mechanical assembly without the requirement for electrical contact. The lower layer is the aforementioned feeding network. The second layer consists of a subarray of air-filled groove gap waveguide cavity. These cavities are coupled to the feed network using slots. On the third layer, radiating elements are formed which are excited by the cavities in the second layer. These slots are spaced at a distance smaller than, but close to one wavelength. The pin surface combined with the small air gaps between the layers, create the forbidden

electromagnetic bandgap and suppress any leakage between them without the need for contact between the layers. The assembled structure with all three layers is shown in Figure 6-15 that shows a compact module that combines the diplexer with the antenna array.
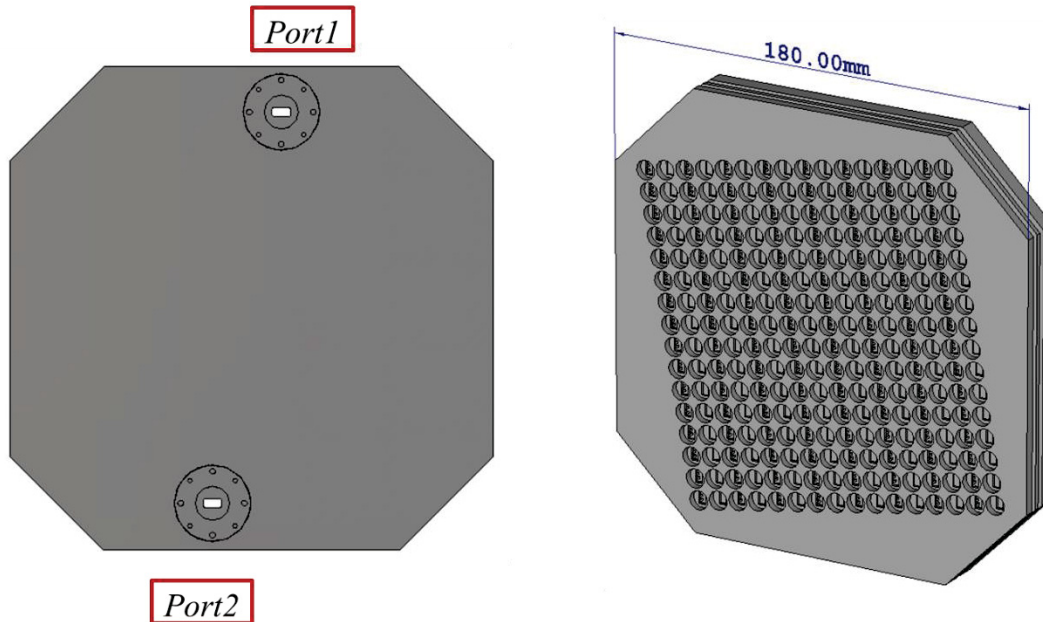
Figure 6-15.   Integrated diplexer-antenna array.

The reflection coefficient of the structure from each port is simulated and plotted in Figure 6-16 along with the reflection for the antenna array without the diplexer. The simulated response is very close to that of Figure 6-11 for the diplexer alone with some negligible degradation in the matching level. This comes from the interference caused by changes made to diplexer when inserted in the middle of the feed network.

The simulated realized gain of the antenna array and the integrated diplexer-antenna array is plotted in Figure 6-17. As it can be seen, after adding the diplexer, the gain of channels are isolated from each other at about 50 dB. Also, the effect of the loss of the diplexer is evident from the decrease in the gain value when compared to the antenna array without the diplexer. The diplexer decreases the realized gain at each channel around 0.7 dB.
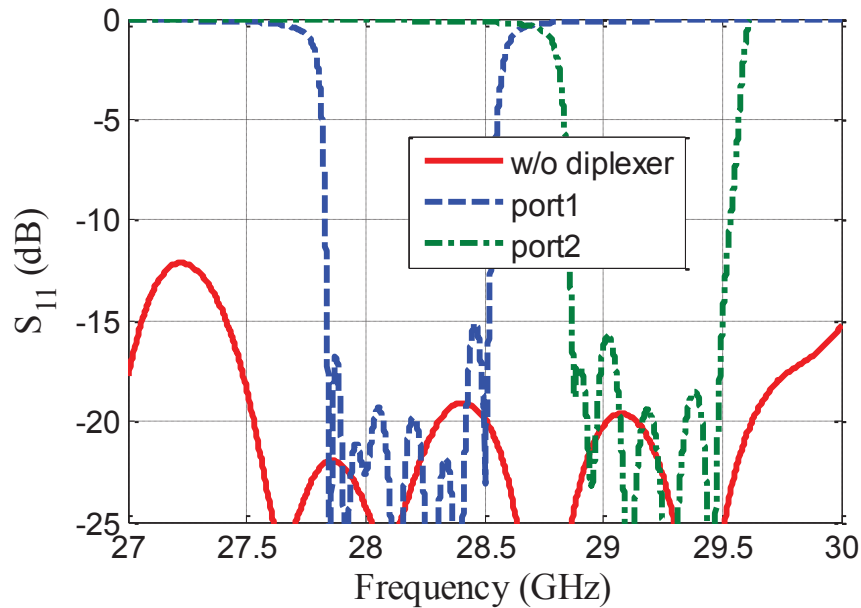
Figure 6-16. **Input reflection coefficient of the antenna without the diplexer and integrated antenna-diplexer from each port.**

6.5. Conclusion

A design procedure for a novel geometry has been presented to realize an integrated diplexer-power divider. The lumped model of the design is based on coupling matrix and is achieved using a new error function which is capable of removing the coupling between the two outputs of the circuit. A guideline has been proposed to design the CM efficiently. Realization of the CM on an EBG based guiding medium has been carried out using a novel method, based on dividing the structure into many sub-circuits and using the delay responses of them in combination with space mapping. The final optimized EM response has been computed, which has shown excellent agreement with the CM response.

The presented geometry has a specific application in array antenna modules. By integrating the power divider into a diplexer, the diplexer can be integrated efficiently with the corporate feed network of the antenna array. As an example, a diplexer with seventh order channel filters was incorporated in the feeding network of a 16×16 antenna array.

As a result, a compact module was achieved that efficiently can realize an antenna array-diplexer. Such a device is very attractive for the applications that involve space limitations.
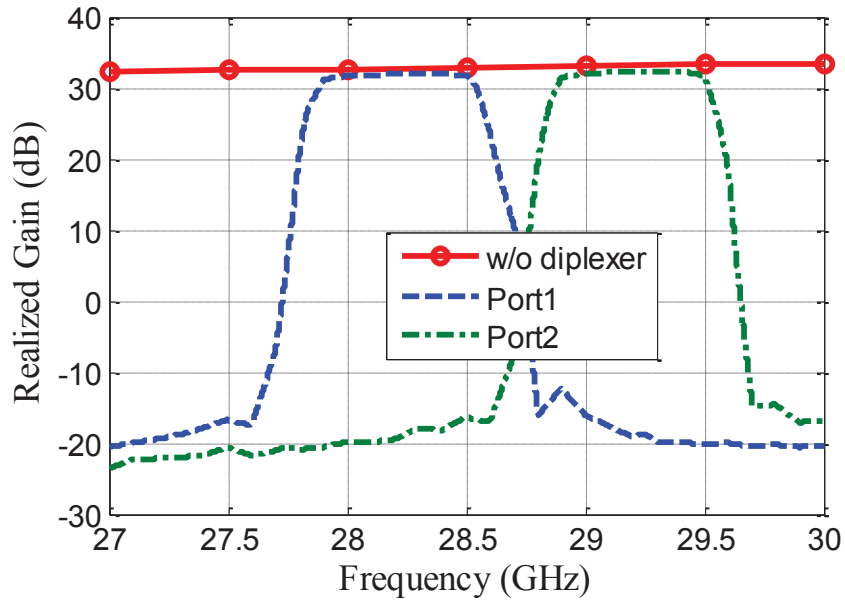
(a)
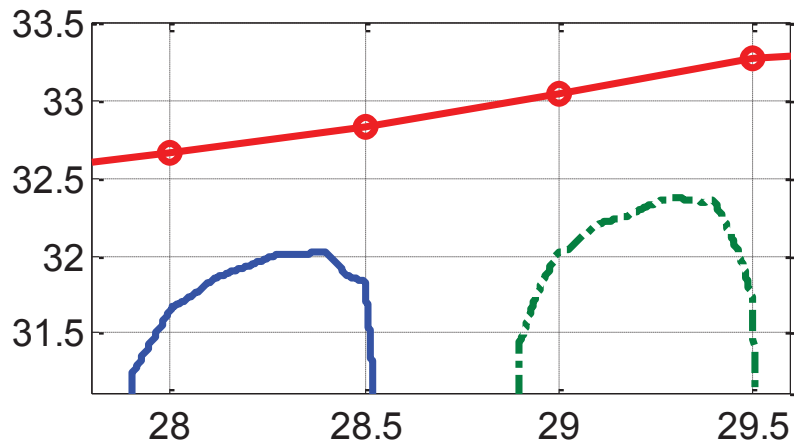
(b)

Figure 6-17. Simulated realized gain of the antenna array and integrated diplexer-antenna array from each port.

Chapter 7.   Conclusion and Future Works

The thesis presented many innovative approaches to realizing low-loss microwave circuits using the new technologies. Many geometries such as bandpass filters, diplexers, bandstop filters and antenna arrays have been developed in the thesis using the metamaterial-based gap waveguide technology. Gap waveguide as an air-filled guiding medium that doesn't need any electrical contact between different layers and parts is a step forward in the microwave industry. However, this technology comes with its own drawbacks. As the result of using a periodic structure in order to suppress the energy in the undesired directions, the structure becomes complex and computationally expensive. A filter as a component that generally needs extensive optimization procedure is mainly affected by this complexity. In order to resolve this issue, many optimization techniques have been used and in many cases developed to be able to optimize the circuits efficiently. As the result, the newly developed techniques of filter design and optimization became an important part of this thesis.

In Chapter 2, completely tuned bandpass filters using gap waveguide technology are presented for the first time. Moreover, filters with transmission zeros at finite frequencies are developed. It is observed that the performance of these filters is comparable with filters in waveguide technology. Using the gap waveguide, these filters are not dependent on the electrical contact. Therefore, their assembly is easier than waveguide components. Electrical contact may not be a critical issue for low-frequency applications as always the distance between the screws is small enough to prevent serious leakage for simple devices. However, in complete systems with many devices that should be integrated together in a small space, electrical contact is a critical issue that might cause interference between different devices in the system and additional loss. Identifying these problems is difficult. Therefore, to assure the electrical contact, an expensive and time-consuming procedure will be needed to resolve these problems. Moreover, at higher frequencies, due to the small size of the components, this becomes more crucial. For such cases, diffusion bonding is one possible solution. However, it's an expensive process. Ridge gap waveguide can be another solution with almost the same fabrication cost as other hollow waveguides. In return, due to the complexity of the

structure, it is computationally expensive. The first chapter resolves this issue by adopting the classical filter design and optimization techniques to be used in this technology.

PCB techniques as a low-cost fabrication method is an attractive solution for many systems. However, it comes with certain limitations in the performance. The main drawback of PCB circuits is their poor performance regarding the insertion loss. Therefore, most of the microstrip circuits at high-frequency bands are accompanied by a bulky and rather expensive packaging box. In Chapter 3 this problem was addressed by using the printed gap waveguide to realize self-packaged, low-loss bandpass filters that can outperform the conventional microstrip circuits and still benefit from the low-cost manufacturing properties of PCB. Many classic and practical bandpass filters have been developed at millimetre-wave band using the gap waveguide technology that is presented along with the measured responses. These circuits as the first prototype, are showing promising results.

The main drawback of the current configuration of gap waveguide is its complexity regarding the placement of the EBG cells within the circuit in order to provide adequate isolation between different parts of the structure. In many cases, the distance among the various branches of the circuit is not enough to place as many cells that are necessary. Moreover, it adds to the complexity of the design process, since during the optimization of the circuits maintaining the correct geometry of the cells becomes a challenging and tedious act. In Chapter 4 by introducing a modification in the arrangement of EBG cells and the guiding ridge, this problem was addressed. Using the proposed geometry, several prototypes have been developed for different applications, such as bandpass and bandstop filters and antenna arrays. Although the proposed geometry requires one additional substrate compared to the normal gap waveguide configuration, it doesn't add much to the cost of circuits but comes with major benefits. Moreover, the low-loss performance of gap waveguide technology still is in practice. Comparison to the leading designs in SIW technology from the literature proves this point that the PRGW can outperform them in many aspects.

A major part of the thesis is devoted to general filter design and optimization theories and techniques. In some cases, the methods were validated using the

conventional technologies, then applied in gap waveguide. In Chapter 5 a generalized methodology was presented to design bandpass filters and diplexers in an efficient iterative process, without the need for any full-wave optimization. Using the proposed method, many states of the art designs were developed and validated by measurement and full-wave simulation. It is observed that the proposed group delay method is capable of optimizing large-scale and complicated circuits that are usually optimized using full-wave optimization or post-fabrication tuning using tuning screws.

The direct application of the group delay method in gap waveguide technology was seen in Chapter 6 where an innovative structure that combines a high-order diplexer into the feeding network of a large-scale antenna array is proposed. In order to realize such a device, we formulated a cost function to design the lumped element network of an integrated diplexer-power divider. To convert this lumped model to physical dimensions, the group delay method was used. Based on our knowledge, no other technique is capable of optimizing such a complicated and computationally expensive structure as efficient. The outcome of Chapter 6 is a unique and compact device that serves both as a diplexer and antenna array at Ka-band. Many applications such as 5G base station networks can benefit from the proposed device to improve the efficiency and realize a more compact sub-system.

7.1. Future Works

Several other filters can be developed in the PRGW technology in order to benefit from its attractive low-cost fabrication and high performance properties. Using the proposed optimization techniques in the thesis, more advanced higher order filters with multiple transmission zeros should be developed to satisfy the strict limitations of the spectrum. With the rising demand to use the 60 GHz band for high transfer rate communication, the PRGW can be a desirable candidate to realize the required filters at this band or moreover, to be used as the standard guiding medium to integrate the complete systems.

The proposed integrated antenna-diplexer in Chapter 6 that was realized in RGW technology shows a promising performance in terms of system Integrability and size.

However, machining cost can be a limiting factor in the proposed device in many systems. A similar product can be designed with PRGW technology to benefit from the low-cost manufacturing of the PCB technology.

The proposed method in Chapter 5 to design large-scale and wideband filters and diplexers, shows promising performance in terms of efficiency and feasibility for different geometries and technologies. The method can be used in the design of the filters and diplexers in other technologies such as combline and coaxial. Our primary investigations show that using the group delay method; complicated filters can be optimized accurately in combline configuration. More analyses and trials are required to assess the performance of the method completely.

References

[1] T. Yoneyama and S. Nishida, "Nonradiative Dielectric Waveguide for Millimeter-Wave Integrated Circuits," *IEEE Trans. Microw. Theory Tech.*, vol. 29, no. 11, pp. 1188–1192, Nov. 1981.

[2] Y. Miura, J. Hirokawa, M. Ando, Y. Shibuya, and G. Yoshida, "Double-Layer Full-Corporate-Feed Hollow-Waveguide Slot Array Antenna in the 60-GHz Band," *IEEE Trans. Antennas Propag.*, vol. 59, no. 8, pp. 2844–2851, Aug. 2011.

[3] P.-S. Kildal, E. Alfonso, A. Valero-Nogueira, and E. Rajo-Iglesias, "Local Metamaterial-Based Waveguides in Gaps Between Parallel Metal Plates," *IEEE Antennas Wirel. Propag. Lett.*, vol. 8, pp. 84–87, 2009.

[4] P.-S. Kildal, A. Zaman, E. Rajo-Iglesias, E. Alfonso, and A. Valero-Nogueira, "Design and experimental verification of ridge gap waveguide in bed of nails for parallel-plate mode suppression," *IET Microw. Antennas Propag.*, vol. 5, no. 3, pp. 262–270, Feb. 2011.

[5] E. Rajo-Iglesias and P.-S. Kildal, "Numerical studies of bandwidth of parallel-plate cut-off realised by a bed of nails, corrugations and mushroom-type electromagnetic bandgap for use in gap waveguides," *IET Microw. Antennas Propag.*, vol. 5, no. 3, pp. 282–289, Feb. 2011.

[6] "https://www.cst.com/Products/CSTmws/eigenmodesolver." .

[7] A. Polemi and S. Maci, "Closed form expressions for the modal dispersion equations and for the characteristic impedance of a metamaterial-based gap waveguide," *IET Microw. Antennas Propag.*, vol. 4, no. 8, pp. 1073–1080, Aug. 2010.

[8] S. A. Razavi, P.-S. Kildal, L. Xiang, E. Alfonso Alos, and H. Chen, "2×2-Slot Element for 60-GHz Planar Array Antenna Realized on Two Doubled-Sided PCBs Using SIW Cavity and EBG-Type Soft Surface fed by Microstrip-Ridge Gap Waveguide," *IEEE Trans. Antennas Propag.*, vol. 62, no. 9, pp. 4564–4573, Sep. 2014.

[9] A. Atia and A. Williams, "Narrow-Bandpass Waveguide Filters," *IEEE Trans. Microw. Theory Tech.*, vol. 20, no. 4, pp. 258–265, Apr. 1972.

[10] A. Atia, A. Williams, and R. W. Newcomb, "Narrow-band multiple-coupled cavity synthesis," *IEEE Trans. Circuits Syst.*, vol. 21, no. 5, pp. 649–655, Sep. 1974.

[11] M. S. Sorkherizi, A. Khaleghi, and P.-S. Kildal, "Direct-Coupled Cavity Filter in Ridge Gap Waveguide," *IEEE Trans. Compon. Packag. Manuf. Technol.*, vol. 4, no. 3, pp. 490–495, Mar. 2014.

[12] A. Zaman, P.-S. Kildal, and A. Kishk, "Narrow-Band Microwave Filter Using High-Q Groove Gap Waveguide Resonators With Manufacturing Flexibility and No Sidewalls," *IEEE Trans. Compon. Packag. Manuf. Technol.*, vol. 2, no. 11, pp. 1882–1889, Nov. 2012.

[13] E. A. Alos, A. U. Zaman, and P. Kildal, "Ka-Band Gap Waveguide Coupled-Resonator Filter for Radio Link Diplexer Application," *IEEE Trans. Compon. Packag. Manuf. Technol.*, vol. 3, no. 5, pp. 870–879, May 2013.

[14] J. W. Bandler, R. Biernacki, S. H. Chen, P. . Grobelny, and R. H. Hemmers, "Space mapping technique for electromagnetic optimization," *IEEE Trans. Microw. Theory Tech.*, vol. 42, no. 12, pp. 2536–2544, Dec. 1994.

[15] J. B. Ness, "A unified approach to the design, measurement, and tuning of coupled-resonator filters," *IEEE Trans. Microw. Theory Tech.*, vol. 46, no. 4, pp. 343–351, Apr. 1998.

[16] E. Pucci, A. U. Zaman, E. Rajo-Iglesias, P.-S. Kildal, and A. Kishk, "Study of Q-factors of ridge and groove gap waveguide resonators," *IET Microw. Antennas Propag.*, vol. 7, no. 11, pp. 900–908, Aug. 2013.

[17] M. Rezaee, A. U. Zaman, and P.-S. Kildal, "A groove gap waveguide iris filter for V-band application," in *2015 23rd Iranian Conference on Electrical Engineering (ICEE)*, 2015, pp. 462–465.

[18] M. Rezaee, A. U. Zaman, and P.-S. Kildal, "V-band groove gap waveguide diplexer," in *2015 9th European Conference on Antennas and Propagation (EuCAP)*, 2015, pp. 1–4.

[19] M. S. Sorkherizi, A. A. Kishk, and A. Khaleghi, "Single and dual mode cavities based on defected bed of nails structure for ridge gap waveguide," in *2014 8th European Conference on Antennas and Propagation (EuCAP)*, 2014, pp. 2669–2673.

[20] R. J. Cameron, C. M. Kudsia, and R. Mansour, *Microwave Filters for Communication Systems: Fundamentals, Design and Applications*, 1 edition. Hoboken, N.J: Wiley-Interscience, 2007.

[21] "http://www.ansys.com/Products/Electronics/ANSYS+HFSS." .

[22] Y. Rahmat-Samii, "Genetic algorithm (GA) and particle swarm optimization (PSO) in engineering electromagnetics," in *17th International Conference on Applied Electromagnetics and Communications, 2003. ICECom 2003*, 2003, pp. 1–5.

[23] H. Raza, J. Yang, P.-S. Kildal, and E. Alfonso Alos, "Microstrip-Ridge Gap Waveguide; Study of Losses, Bends, and Transition to WR-15," *IEEE Trans. Microw. Theory Tech.*, vol. 62, no. 9, pp. 1943–1952, Sep. 2014.

[24] J.-S. Hong, *Microstrip Filters for RF/Microwave Applications*, 2 edition. Hoboken, N.J: Wiley, 2011.

[25] G. Matthaei, E. M. T. Jones, and L. Young, *Microwave Filters, Impedance-Matching Networks, and Coupling Structures*. Norwood, Mass: Artech House, 1980.

[26] M. Meng and K.-L. Wu, "An Analytical Approach to Computer-Aided Diagnosis and Tuning of Lossy Microwave Coupled Resonator Filters," *IEEE Trans. Microw. Theory Tech.*, vol. 57, no. 12, pp. 3188–3195, Dec. 2009.

[27] A. A. Brazalez, A. U. Zaman, and P.-S. Kildal, "Improved Microstrip Filters Using PMC Packaging by Lid of Nails," *IEEE Trans. Compon. Packag. Manuf. Technol.*, vol. 2, no. 7, pp. 1075–1084, Jul. 2012.

[28] E. Pucci, E. Rajo-Iglesias, and P.-S. Kildal, "New Microstrip Gap Waveguide on Mushroom-Type EBG for Packaging of Microwave Components," *IEEE Microw. Wirel. Compon. Lett.*, vol. 22, no. 3, pp. 129–131, Mar. 2012.

[29] M. Li and K. M. Luk, "Low-Cost Wideband Microstrip Antenna Array for 60-GHz Applications," *IEEE Trans. Antennas Propag.*, vol. 62, no. 6, pp. 3012–3018, Jun. 2014.

[30] L. Lu, K. Ma, F. Meng, and K. S. Yeo, "Design of a 60-GHz Quasi-Yagi Antenna With Novel Ladder-Like Directors for Gain and Bandwidth Enhancements," *IEEE Antennas Wirel. Propag. Lett.*, vol. 15, pp. 682–685, 2016.

[31] J. Xu, Z. N. Chen, and X. Qing, "270-GHz LTCC-Integrated High Gain Cavity-Backed Fresnel Zone Plate Lens Antenna," *IEEE Trans. Antennas Propag.*, vol. 61, no. 4, pp. 1679–1687, Apr. 2013.

[32] J. Xu, Z. N. Chen, X. Qing, and W. Hong, "Bandwidth Enhancement for a 60 GHz Substrate Integrated Waveguide Fed Cavity Array Antenna on LTCC," *IEEE Trans. Antennas Propag.*, vol. 59, no. 3, pp. 826–832, Mar. 2011.

[33] W. Liu, Z. N. Chen, and X. Qing, "60-GHz Thin Broadband High-Gain LTCC Metamaterial-Mushroom Antenna Array," *IEEE Trans. Antennas Propag.*, vol. 62, no. 9, pp. 4592–4601, Sep. 2014.

[34] S. B. Yeap, Z. N. Chen, and X. Qing, "Gain-Enhanced 60-GHz LTCC Antenna Array With Open Air Cavities," *IEEE Trans. Antennas Propag.*, vol. 59, no. 9, pp. 3470–3473, Sep. 2011.

[35] W. C. Yang, H. Wang, W. Q. Che, Y. Huang, and J. Wang, "High-Gain and Low-Loss Millimeter-Wave LTCC Antenna Array Using Artificial Magnetic Conductor Structure," *IEEE Trans. Antennas Propag.*, vol. 63, no. 1, pp. 390–395, Jan. 2015.

[36] W. Han, F. Yang, J. Ouyang, and P. Yang, "Low-Cost Wideband and High-Gain Slotted Cavity Antenna Using High-Order Modes for Millimeter-Wave Application," *IEEE Trans. Antennas Propag.*, vol. 63, no. 11, pp. 4624–4631, Nov. 2015.

[37] Y. Li and K. M. Luk, "60-GHz Substrate Integrated Waveguide Fed Cavity-Backed Aperture-Coupled Microstrip Patch Antenna Arrays," *IEEE Trans. Antennas Propag.*, vol. 63, no. 3, pp. 1075–1085, Mar. 2015.

[38] A. U. Zaman and P. S. Kildal, "Wide-Band Slot Antenna Arrays With Single-Layer Corporate-Feed Network in Ridge Gap Waveguide Technology," *IEEE Trans. Antennas Propag.*, vol. 62, no. 6, pp. 2992–3001, Jun. 2014.

[39] H. Attia, M. S. Sorkherizi, and A. A. Kishk, "60 GHz slot antenna array based on ridge gap waveguide technology enhanced with dielectric superstrate," in *2015 9th European Conference on Antennas and Propagation (EuCAP)*, 2015, pp. 1–4.

[40] Y. Li and K. M. Luk, "60-GHz Dual-Polarized Two-Dimensional Switch-Beam Wideband Antenna Array of Aperture-Coupled Magneto-Electric Dipoles," *IEEE Trans. Antennas Propag.*, vol. 64, no. 2, pp. 554–563, Feb. 2016.

[41] P. N. Choubey, W. Hong, Z. C. Hao, P. Chen, T. V. Duong, and J. Mei, "A Wideband Dual-Mode SIW Cavity-Backed Triangular-Complimentary-Split-Ring-Slot (TCSRS) Antenna," *IEEE Trans. Antennas Propag.*, vol. 64, no. 6, pp. 2541–2545, Jun. 2016.

[42] S. Amari, "Synthesis of cross-coupled resonator filters using an analytical gradient-based optimization technique," *IEEE Trans. Microw. Theory Tech.*, vol. 48, no. 9, pp. 1559–1564, Sep. 2000.

[43] R. J. Cameron, A. R. Harish, and C. J. Radcliffe, "Synthesis of advanced microwave filters without diagonal cross-couplings," *IEEE Trans. Microw. Theory Tech.*, vol. 50, no. 12, pp. 2862–2872, Dec. 2002.

[44] R. J. Cameron and F. Seyfert, "Coupling matrix synthesis for a new class of microwave filter configuration," in *Microwave Symposium Digest, 2005 IEEE MTT-S International*, 2005, p. 4 pp.–.

[45] W. Feng, W. Che, and Q. Xue, "Transversal Signal Interaction: Overview of High-Performance Wideband Bandpass Filters," *IEEE Microw. Mag.*, vol. 15, no. 2, pp. 84–96, Mar. 2014.

[46] S. Amari, F. Seyfert, and M. Bekheit, "Theory of Coupled Resonator Microwave Bandpass Filters of Arbitrary Bandwidth," *IEEE Trans. Microw. Theory Tech.*, vol. 58, no. 8, pp. 2188–2203, Aug. 2010.

[47] R. J. Cameron, "General coupling matrix synthesis methods for Chebyshev filtering functions," *IEEE Trans. Microw. Theory Tech.*, vol. 47, no. 4, pp. 433–442, Apr. 1999.

[48] M. Kahrizi, S. Safavi-Naeini, S. K. Chaudhuri, and R. Sabry, "Computer diagnosis and tuning of RF and microwave filters using model-based parameter estimation," *IEEE Trans. Circuits Syst. Fundam. Theory Appl.*, vol. 49, no. 9, pp. 1263–1270, Sep. 2002.

[49] J. Marquardt and G. Muller, "Computer-Aided Tuning of Microwave Circuits," in *Microwave Symposium Digest, 1977 IEEE MTT-S International*, 1977, pp. 147–150.

[50] R. J. Cameron and J. D. Rhodes, "Asymmetric Realizations for Dual-Mode Bandpass Filters," *IEEE Trans. Microw. Theory Tech.*, vol. 29, no. 1, pp. 51–58, Jan. 1981.

[51] F. M. Vanin, D. Schmitt, and R. Levy, "Dimensional synthesis for wide-band waveguide filters and diplexers," *IEEE Trans. Microw. Theory Tech.*, vol. 52, no. 11, pp. 2488–2495, Nov. 2004.

[52] H. Y. Hwang and S. Yun, "The design of bandpass filters considering frequency dependence of inverters," *Microw. J*, vol. 45, pp. 154–163, Sep. 2002.

[53] A. Morini, T. Rozzi, and M. Morelli, "New formulae for the initial design in the optimization of T-junction manifold multiplexers," in *Microwave Symposium Digest, 1997., IEEE MTT-S International*, 1997, vol. 2, pp. 1025–1028 vol.2.

[54] J. Rhodes and R. Levy, "A Generalized Multiplexer Theory," *IEEE Trans. Microw. Theory Tech.*, vol. 27, no. 2, pp. 99–111, Feb. 1979.

[55] K. L. Wu and W. Meng, "A Direct Synthesis Approach for Microwave Filters With a Complex Load and Its Application to Direct Diplexer Design," *IEEE Trans. Microw. Theory Tech.*, vol. 55, no. 5, pp. 1010–1017, May 2007.

[56] H. Meng and K. L. Wu, "Direct Optimal Synthesis of a Microwave Bandpass Filter with General Loading Effect," *IEEE Trans. Microw. Theory Tech.*, vol. 61, no. 7, pp. 2566–2573, Jul. 2013.

[57] P. Zhao and K. L. Wu, "Circuit model extraction for computer-aided tuning of a coupled-resonator diplexer," in *2015 IEEE MTT-S International Microwave Symposium*, 2015, pp. 1–3.

[58] M. A. Ismail, D. Smith, A. Panariello, Y. Wang, and M. Yu, "EM-based design of large-scale dielectric-resonator filters and multiplexers by space mapping," *IEEE Trans. Microw. Theory Tech.*, vol. 52, no. 1, pp. 386–392, Jan. 2004.

[59] M. H. Bakr, J. W. Bandler, N. Georgieva, and K. Madsen, "A hybrid aggressive space-mapping algorithm for EM optimization," *IEEE Trans. Microw. Theory Tech.*, vol. 47, no. 12, pp. 2440–2449, Dec. 1999.

[60] P. Zhao and K. L. Wu, "An Iterative and Analytical Approach to Optimal Synthesis of a Multiplexer With a Star-Junction," *IEEE Trans. Microw. Theory Tech.*, vol. 62, no. 12, pp. 3362–3369, Dec. 2014.

[61] K. L. Wu and H. Wang, "A rigorous modal analysis of H-plane waveguide T-junction loaded with a partial-height post for wide-band applications," *IEEE Trans. Microw. Theory Tech.*, vol. 49, no. 5, pp. 893–901, May 2001.

[62] X. Shang, Y. Wang, W. Xia, and M. J. Lancaster, "Novel Multiplexer Topologies Based on All-Resonator Structures," *IEEE Trans. Microw. Theory Tech.*, vol. 61, no. 11, pp. 3838–3845, Nov. 2013.

[63] A. Vosoogh and P. S. Kildal, "Corporate-Fed Planar 60 GHz Slot Array Made of Three Unconnected Metal Layers Using AMC pin surface for the Gap Waveguide," *IEEE Antennas Wirel. Propag. Lett.*, vol. PP, no. 99, pp. 1–1, 2015.

[64] A. Vosoogh, P. S. Kildal, and V. Vassilev, "A multi-layer gap waveguide array antenna suitable for manufactured by die-sink EDM," in *2016 10th European Conference on Antennas and Propagation (EuCAP)*, 2016, pp. 1–4.